Western Graduate&PostdoctoralStudies

Western University
Scholarship@Western

Electronic Thesis and Dissertation Repository

8-22-2011 12:00 AM

Validation and Application of Wind Profiler Measurements of Atmospheric Turbulence

Armin Dehghan, *The University of Western Ontario*

Supervisor: Prof. Wayne K. Hocking, *The University of Western Ontario*

A thesis submitted in partial fulfillment of the requirements for the Doctor of Philosophy degree in Physics

© Armin Dehghan 2011

Follow this and additional works at: https://ir.lib.uwo.ca/etd

 Part of the Physics Commons

Recommended Citation

Dehghan, Armin, "Validation and Application of Wind Profiler Measurements of Atmospheric Turbulence" (2011). *Electronic Thesis and Dissertation Repository*. 251.
https://ir.lib.uwo.ca/etd/251

This Dissertation/Thesis is brought to you for free and open access by Scholarship@Western. It has been accepted for inclusion in Electronic Thesis and Dissertation Repository by an authorized administrator of Scholarship@Western. For more information, please contact wlswadmin@uwo.ca.

Validation and Application of Wind Profiler Measurements of Atmospheric Turbulence

(Spine Title: Validation and Application of Profiler Measurements of Turbulence)

(Thesis Format: Monograph)

by

Armin Dehghan

Faculty of Science
Department of Physics and Astronomy

Submitted in partial fulfillment
of the requirements for the degree of
Doctor of Philosophy

School of Graduate and Postdoctoral Studies
The University of Western Ontario
London, Ontario, Canada
August, 2011

© Armin Dehghan 2011

Certificate of Examination

The University of Western Ontario

School of Graduate and Postdoctoral Studies

Supervisor	Examiners
Dr. Wayne K. Hocking	Dr. Tamie Poepping
Supervisory Committee	Dr. Martin Houde
Dr. Paul Wiegert	Dr. Gregory Kopp
Dr. Peter Brown	Dr. Gary Klaassen

The thesis by

Armin Dehghan

entitled:

Validation and Application of Wind Profiler Measurements of Atmospheric Turbulence

is accepted in partial fulfillment of the
requirements for the degree of

Doctor of Philosophy

Date	Chair of the Thesis Examination Board

Abstract

This thesis focuses on the investigation of the reliability of turbulence measurements by radars when the spectral-width method is used. This method employs the spectral widths observed by radar (experimental spectral width) to determine turbulence. However, the experimental width can be affected by non-turbulent effects, including radar geometry. Therefore, the spectral width due to non-turbulent effects (theoretical spectral width) must be removed from the experimental width. This can occasionally lead to negative values of turbulence.

It is our aim (1) to study the effects of both experimental and theoretical spectral widths on the accuracy of turbulence measurements, (2) to study the validity of "negative" values of turbulence, and (3) to compare radar-estimated values of turbulence with in-situ measurements.

This is performed by studying the factors that can contribute to errors in estimation of spectral widths, including mean wind speed, wind shear, anisotropy and length of data. In addition to that, radar-estimated turbulence is compared to turbulence measured by high-resolution research and commercial aircraft.

Significant findings include:

1. The statistical fluctuations of mean wind speed and its impact on estimation of the theoretical spectral width is the most important factor in producing errors in turbulence measurements.

2. The choice of spectrum fitting algorithm and length of data is very important in producing experimental spectral widths.

3. In order to estimate theoretical widths more accurately, a formula is developed by comparing models that calculate the theoretical spectral width.

4. It is found that both negative and positive values of turbulence need to be included in turbulence analysis. However, if the percentage of negatives exceeds 35%, the measurements are not reliable.

5. Turbulence data measured by radar agrees well with high-resolution aircraft data for weak turbulence. However, in-situ aircraft measurements show a higher probability of strong turbulence than hourly radar data.

6. The theoretical spectral width is small compared to the experimental one for strong turbulence. By discarding the theoretical spectral widths in turbulence

calculations, we can measure near-instantaneous values of turbulence rather than hourly averages. Therefore, we can improve the agreement between the aircraft-estimated and radar-estimated turbulence for strong values of turbulence.

Key words: Turbulence, Radar, Spectral-width method, Reliability

Acknowledgements

I would like to thank all people who helped or inspired me during my doctoral study.

I especially want to thank my supervisor, Prof. Wayne K. Hocking, for his guidance and encouragement. This work would have not been possible without his invaluable support.

I am also thankful to Dr. Peter Brown and Dr. Paul Wiegert for serving on my advisory committee.

I would like to express my gratitude to Dr. Steve Argall, Dr. Nimalan Swarnalingam and Mohammed Osman for their support during this work.

It is my pleasure to thank Dr. Katherine Hayden from Environment Canada, Ramesh Srinivasan and Matthew Bastian from the National Research Council of Canada, Dr. Robert Sharman and Dr. Rod Frehlich from the National Center for Atmospheric Research and Dr. Donald Wroblewski from Boston University for providing me with aircraft data and giving me valuable comments and suggestions.

I would like to express my heart-felt gratitude to my family for their love, encouragement and support over the years.

And finally thanks to all my friends for making my life a lot more fun.

Contents

List of Tables

List of Figures

Chapter 1

Background, Theory and Instrumentation

Turbulence is one of the characteristic properties of atmospheric flow. The importance of turbulence has been recognized by scientists since near the end of 19th century. In 1883, Reynolds identified two different types of fluid flow, namely laminar (non turbulent) and turbulent by experimenting on flow in long straight pipes. He also concluded that transition from laminar to turbulent flow depends on the average velocity of the fluid, radius of the pipe and the viscosity of the fluid (Sutton, 1960).

The mixing and diffusion characteristics of turbulence in the atmosphere motivated many meteorologists. Taylor (1922) developed a diffusion theory which was the foundation of many studies on atmospheric dispersion. In fact, it is now understood that turbulence plays an important role in a large number of processes in the atmosphere, including (among others) transport of pollutants and dissipation of fog.

Most early studies of atmospheric turbulence and diffusion took place in the atmospheric boundary layer. Studies of the upper levels were really only developed during world-war II, when interest developed in relation to aircraft safety. Turbulence in the upper levels was found to be patchy, with frequent regions of non-turbulent flow interspersed with occasionally intense bursts. Such intense localized regions of turbulence were termed "Clear Air Turbulence", or CAT.

In 1941, Kolmogorov studied the statistical characteristics of turbulence and introduced one of the most advanced theories in turbulence. His studies showed that in 3-D turbulence, energy continuously passes from the large to smaller scale motions. Hence it can be concluded that turbulence may be driven by larger-scale motions.

Therefore, it is important to take turbulence into account when designing aircraft and forecasting weather. Turbulence is also a key parameter in air pollution dispersion

models. These models help to estimate or predict the concentration of air pollutants or toxins emitted from various sources.

1.1 Definition and Properties of Turbulence

Turbulence is defined as a three dimensional, rotational, dissipative, intermittent, non linear and diffusive motion (Vinnichenko et al., 1973). A turbulent flow is a result of the growth of small disturbances which are no longer damped by the flow. These disturbances grow by extracting energy from the primary flow.

In the atmosphere, large scale motions can be examined through the Navier-Stokes equation (Holton, 1992) :

$$\frac{D\mathbf{U}}{Dt} = -2\mathbf{\Omega} \times \mathbf{U} - \frac{1}{\rho}\boldsymbol{\nabla} p + \mathbf{g} + \mathbf{F}_r, \tag{1.1}$$

where $\mathbf{U}$ is the velocity vector, $\mathbf{\Omega}$ the angular velocity of earth's rotation , ρ the density, p the pressure, $\boldsymbol{g}$ the gravitational acceleration, and F_r the viscous force. The velocity vector $\mathbf{U}$**,** and the operator $\boldsymbol{\nabla}$, may be written as:

$$\mathbf{U} = \mathbf{i}\mathrm{u} + \mathbf{j}\mathrm{v} + \mathbf{k}\mathrm{w}, \tag{1.2}$$

$$\boldsymbol{\nabla} = \mathbf{i}\frac{\partial}{\partial x} + \mathbf{j}\frac{\partial}{\partial y} + \mathbf{k}\frac{\partial}{\partial z}, \tag{1.3}$$

In which u, v and w are the wind velocity components and $\mathbf{i}$, $\mathbf{j}$ and $\mathbf{k}$ are unit vectors and can be taken to be directed eastward, northward and upward respectively. Furthermore, the term in the left side of the Equation (1.1) can be written as:

$$\frac{D\mathrm{U}}{Dt} = \frac{\partial \mathrm{U}}{\partial t} + \boldsymbol{U}.\boldsymbol{\nabla}\boldsymbol{U}, \tag{1.4}$$

where $\frac{\partial \mathrm{U}}{\partial t}$ is the local rate of change of wind velocity and $\mathrm{U}.\boldsymbol{\nabla}\mathrm{U}$ is the advective term and is due to local change of velocity due to air motion.

In turbulent flow, the measured parameter fluctuates in time. In order that the velocity measurements be representative of turbulent flow, we define the instantaneous velocity as:

$$\mathbf{U} = \overline{\mathbf{U}} + \mathbf{U}', \tag{1.5}$$

where $\overline{\mathbf{U}}$ and $\mathbf{U}'$ are the time-averaged value and fluctuating part of the velocity

respectively.

Now we substitute Equation (1.5) into Equation (1.1). It should be noted that small fluctuations in density associated with turbulence have been neglected. A scale analysis also showed that gravity and viscosity forces are small compared to gradient pressure and Coriolis forces for many types of flow, so we will largely neglect them in our calculation. The results of substituting and averaging for horizontal motion (e.g eastward) is given by (for other components of motion see Holton, 1992):

$$\frac{D\overline{\mathrm{u}}}{Dt} - f_{co}\,\overline{\mathrm{v}} = -\frac{1}{\rho}\frac{\partial \bar{p}}{\partial x} - \left[\frac{\partial}{\partial x}\left(\rho\overline{\mathrm{u}'\mathrm{u}'}\right) + \frac{\partial}{\partial y}\left(\rho\overline{\mathrm{u}'\mathrm{v}'}\right) + \frac{\partial}{\partial z}\left(\rho\overline{\mathrm{u}'\mathrm{w}'}\right)\right], \tag{1.6}$$

where f_{co} is the Coriolis parameter and related to latitude Φ, through: $f_{co} = 2\Omega\sin(\Phi)$.

Clearly disturbances in the flow have added new terms to the mean Navier-Stokes equation. The new terms in the bracket on the right side of Equation (1.6), which depend on the turbulent fluctuations, are called Reynolds stress terms. Reynolds stress terms are non-linear and represent the momentum fluxes. For example, the $\rho\overline{\mathrm{u}'\mathrm{w}'}$ term in Equation (1.6) describes the vertical flux of horizontal momentum. Similarly, $\overline{\mathrm{w}'\theta_p'}$ represents the vertical turbulent heat flux in which θ_p is the potential temperature or simply the temperature that a parcel of dry air at pressure, p and temperature, T would have if it were expanded or compressed adiabatically to a standard pressure, p_s. The potential temperature is given by:

$$\theta_p = T\left(\frac{p_s}{p}\right)^{\mathrm{R}/C_p}, \tag{1.7}$$

where R is the gas constant and C_p the specific heat capacity at constant pressure.

The non-linearity of turbulent equations such as Equation (1.6) makes them difficult for mathematicians to find exact solutions, however it is necessary for description of turbulent flow. Non-linear terms bring together air parcels with different velocities. This produces strong gradients in which perturbation may grow and airflow becomes turbulent. As a result of mixing, strong fluxes of momentum and energy will be created which modify large-scale motions.

Rotation is another important characteristic of a turbulent flow. In a flow, vorticity is a measure of rotation and is highly correlated to disturbances. Vorticity is related to the velocity, $\mathbf{U}$, through the following equation (Holton, 1992):

$$\boldsymbol{\omega} = \boldsymbol{\nabla} \times \mathbf{U}, \tag{1.8}$$

where ω is the vorticity and perpendicular to the flow direction.

In turbulent motion, the strong velocity gradients in all directions generates vortices which are called eddies. Eddies carry turbulent kinetic energy and they have a wide range of scales. For example in the atmosphere, they can be hundreds of kilometers in diameter to scales of a few centimeters.

One point needs to be made here. Eddies with scales of hundreds of kilometers are associated with 2-D turbulence in which energy is moved from smaller scales to larger scales. The opposite happens in 3-D turbulence where instead energy transfers from larger eddies of scales of a few kilometers to smaller ones. It is also assumed that eddies act in a manner similar to molecular diffusion so that the flux of a given field is proportional to the local gradient of the mean. In this case, we can define the diffusion coefficient through the following equations (Holton, 1992):

$$\overline{\mathrm{u}'\mathrm{w}'} = -k_m \left(\frac{\partial \overline{\mathrm{u}}}{\partial z} \right), \tag{1.9}$$

$$\overline{\theta_p' \mathrm{w}'} = -k_h \left(\frac{\partial \overline{\theta_p}}{\partial z} \right), \tag{1.10}$$

where k_m is the eddy viscosity coefficient and k_h is the eddy diffusivity of heat. It should be noted that unlike the molecular viscosity coefficient, eddy viscosities depend on the flow condition rather than the physical properties of the fluid.

The cascade of kinetic energy from larger eddies to smaller ones and the conversion of kinetic energy to heat by viscosity in the smallest eddies is a defining feature of 3-D turbulence. Kolmogorov (1941) described turbulent motion as an unstable flow with perturbations which generate "turbulent eddies of first order". These produce irregular displacements with velocities which are less than the mean flow. These eddies are also unstable and they produce "second order eddies" with smaller characteristic sizes and velocities. The process of reduction in size of turbulent eddies will continue until the effect of viscosity on very small eddies (due to the large associated shear) becomes dominant and energy will be dissipated to heat (Vinnichenko et al., 1973).

1.2 Causes of Turbulence in the Atmosphere

The main causes of turbulence in the atmosphere are due to differences in the large scale temperature and velocity fields. Atmospheric processes which produce these differences are itemized below:

- Uneven heating of various parts of the earth surface which leads to development

of thermal convection circulations. As solar radiation heats the earth's surface, the temperature in the lower layer of the atmosphere increases and convection starts. The motion of air parcel is unstable since in rising, the parcel finds itself warmer than its surroundings and continue to rise. Because the rising parcel exchanges heat with cooler air around it, at some point, it becomes denser. However, it can not descend through the rising air, so it moves horizontally for some distance and begins to descend. This is called convection circulation. Such flows are the primary cause of turbulence in the boundary layer of the atmosphere. This form of turbulence is usually associated with large eddies of approximately a few kilometers in size (Ahrens, 2000).

- Surface friction slows down the wind in the lowest layers of the atmosphere causing the air to turn over in turbulent eddies. It also generates large vertical wind gradients.

- Deformation of flow by barriers and obstacles on the earth surface produces wavy disturbances and rotary motions. Obstructions such as buildings, trees, mountains etc., disrupt smooth wind flow into eddies in the downstream of the flow. Higher wind speeds and rougher surfaces produce stronger turbulence. One of the most hazardous types of turbulence is produced by lee waves and rotors on the lee side of the mountains. When air is forced to flow over a mountain under stable conditions, air parcels are displaced from their equilibrium levels and undergo buoyancy oscillations as they move downstream of the mountain. Vertical currents within these oscillation are sometimes very strong and can produce vortices called rotors when they are combined with surface friction. Rotors can cause severe turbulence beneath mountain waves (Holton, 1992).

- Convergence and interaction of air masses with different characteristics which generates temperature and velocity differences near atmospheric fronts. Transition of air from one air mass to another one along the frontal boundaries produces turbulence.

- Growth of vertically propagating gravity waves formed in stable layers in the troposphere and stratosphere. Atmospheric gravity waves can only exist when the atmosphere is stably stratified so that an air parcel displaced vertically will undergo buoyancy oscillations. As these waves move upward, their amplitudes increase. When the wave amplitude reaches the critical level (i.e. where the phase speed of the wave equals the component of the mean wind in the propa-

gation direction of the wave), it breaks into turbulence, causing large amounts of wave energy to be transferred to turbulent kinetic energy (Nappo, 2002).

- Jet-stream turbulence is produced by both strong vertical and horizontal wind shear close to and within the jet-stream. Jet-streams are fast flowing air currents in the atmosphere which are thousands of kilometers long, a few hundred kilometers wide and only a few kilometers thick. Wind speeds in the central core of a jet-stream often exceed 100 knots and occasionally reach 200 knots. The main jet-streams are located near the tropopause, however they can occur at higher or lower altitudes (Ahrens, 2000).

These processes can act individually or simultaneously to produce convective or shear turbulence of differing intensity in the atmosphere. Regions of convective turbulence are generally visible by the presence of cumulus type clouds and can be avoided by aircraft. However, shear turbulence is often optically invisible, so it is called clear air turbulence (CAT). Mountain waves, gravity waves and jet-streams are the most important causes of CAT.

1.3 Transition from Non-turbulent to Turbulent Motion

Flow that is not turbulent is called laminar flow. Turbulent flow can be produced by the growth of perturbations in a laminar flow. Although there is no complete theorem that describes the laminar-turbulent transition, study of the Reynolds and Richardson numbers can be useful in this manner.

The Reynolds number (Re) is defined as a ratio of inertial force to viscosity force. If we only consider the dimensions, we have (Vinnichenko et al., 1973):

$$\mathrm{Re} = |\frac{\mathbf{U}.\nabla\mathbf{U}}{\upsilon\nabla^2\mathbf{U}}| \sim \frac{V_c L_c}{\upsilon}, \tag{1.11}$$

where $\mathbf{U}$ is the velocity, υ the kinematic viscosity of the flow, V_c the characteristic velocity of the flow and L_c the characteristic scale of the flow. It has often been observed that turbulent flows arise from laminar flows as Re increases. In fact inertial forces act to bring together volumes of fluid that are separate from each other and have different velocities. This produces wind shear which plays an important role in producing turbulence. In contrast, viscosity forces smooth out the variations in velocities. At low values of Re, when viscosity forces are dominant, the flow is laminar.

As Re increases, the effect of the viscosity force decreases and velocity fluctuations will be formed. This leads to a turbulent flow. However, it is difficult to define an appropriate flow scale due to scale variability of flows associated with different types of motions (i.e. gravity waves, turbulence, etc.) in the atmosphere.

Therefore, in the atmosphere, measuring the Richardson number is more useful. The relative importance of static stability and dynamics instability in producing turbulence is expressed by the Richardson number (Ri) through (Vinnichenko et al., 1973):

$$\mathrm{Ri} = \frac{g}{\theta_p} \frac{\frac{d\theta_p}{dz}}{\left(\frac{d\overline{\mathrm{U}}}{dz}\right)^2}, \tag{1.12}$$

where $\frac{d\overline{\mathrm{U}}}{dz}$ is the vertical gradient of the mean wind velocity, g the gravity acceleration and θ_p the potential temperature. Theoretical and laboratory research suggest that laminar flow becomes turbulent when Ri is smaller than a critical value. Although there is some debate on the correct critical value, it seems that the value of 0.25 is a good approximation in the atmosphere. Note that the Richardson number is only an indicator of the presence of turbulence and says nothing about the intensity of turbulence (Stull, 1988).

1.4 Turbulent Energy Dissipation Rate

Turbulence is associated with the formation of eddies. The 3-D turbulent eddies have a wide range of scales from a few kilometers to a few centimeters. In 1941, Kolmogorov introduced one of the most important theories in turbulence. Kolmogorov proposed that the turbulent energy spectrum has three parts: an energy-containing subrange, an inertial subrange and a dissipation subrange. Most of the energy is in the energy-containing subrange and there is a continuous transfer of energy from the large scale eddies in the energy-containing subrange to smaller eddies in the inertial subrange (Panofsky and Dutton, 1984). In the dissipation subrange, eddies are small enough that viscosity becomes dominant due to the presence of large small-scale wind shears. It is also assumed that turbulence is isotropic in the inertial subrange which suggests that properties of turbulence are independent of direction in this range (Wyngaard, 2010). In the inertial subrange, the rate of transfer of kinetic energy per unit of mass is independent of scale. Therefore, the rate at which kinetic energy is transferred from one scale to smaller ones must be equal to the turbulent energy dissipation rate,

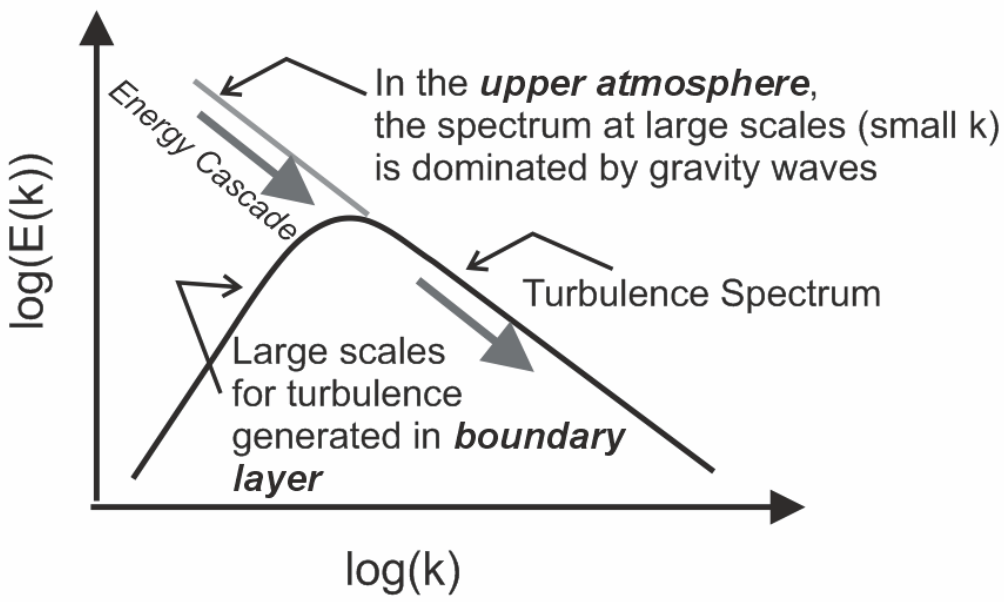

Figure 1.1: Diagram of energy spectrum, E(k) as a function of wave number k; in the upper atmosphere, the spectrum increases at small k due to the presence of gravity waves, whereas in the boundary layer, the spectrum decreases at small k.

ε or the rate at which turbulent kinetic energy is dissipated to heat by viscosity. The scale at which dissipation begins is called the inner scale. This scale is related to the so-called Kolmogorov microscale, μ, and it is related to energy dissipation rate, ε, and the kinematic viscosity, υ, through the following equation:

$$\mu = \left(\frac{\upsilon^3}{\varepsilon}\right)^{\frac{1}{4}}. \tag{1.13}$$

Figure 1.1 shows the typical turbulent energy spectrum for a flow in the atmosphere. The energy-containing subrange of the spectrum and the region of large scale eddies is associated with smaller wave number, k. The inertial subrange in which dissipation of energy is very small indicated by the word "turbulence spectrum" in the graph. The dissipation subrange (not shown in the Figure 1.1) is associated with larger k and the spectrum falls sharply for scales less than the inner scale due to energy dissipation within this region.

According to the Kolmogorov theory, the inertial subrange is isotropic. Therefore the velocity depends on wave number, k and ε at this range. Dimensional analysis (Kolmogorov, 1941) shows that the full three-dimensional energy spectrum of turbulent motion, $F\,(\mathrm{k})$ is given by:

$$F(\mathbf{k}) = \mathrm{A}\varepsilon^{2/3}\mathrm{k}^{-11/3}. \tag{1.14}$$

This function is due to all three velocity components and it can be visualized as a solid sphere which has highest energy density at the center, and decreasing energy density as |k| increases. This function is isotropic and it is often integrated over a shell of radius k. The resultant function, $S(\mathrm{k})$ represents the total energy in the shell and is written as (see Appendix A):

$$S(\mathrm{k}) = \mathrm{A}_0\varepsilon^{2/3}\mathrm{k}^{-5/3}. \tag{1.15}$$

Constants A and A_0 are 0.12 and 1.53 respectively (Hocking, 1999).

Coincidentally, the same spectral form as Equation (1.15) also holds for one dimensional spectra. However, the constant A_0 can not be used and should be replaced by a proper constant (Hocking, 1999) for the spectrum along and perpendicular to the direction of traverse through the flow. One should note that there are different types of spectra and it is important to distinguish these spectra (see Appendix B).

1.5 Turbulence Measurements and Applications

In the past few decades, many studies have been performed for a clearer understanding of turbulence, and this has led to development of various techniques which can be used to estimate turbulence in the atmosphere. The purpose of the review in this section is to present a summary of major studies in turbulence measurements.

The two main techniques that have been used to measure turbulence are in-situ (i.e. instrumented balloons, rockets and aircraft) and radar techniques. However, different approaches (i.e. spectral analysis, structure function, etc.) were taken to estimate and study turbulence.

Rees et al. (1972) used rocket techniques to measure the intensity of turbulence in the upper atmosphere ($\sim$ 90 km altitude). The turbulent energy dissipation rate, ε, which also defines the intensity of turbulence, was estimated from the rate of expansion of the rocket trail. This method is mostly used to measure turbulence in the upper atmosphere which is hard to reach by other in-situ techniques.

High-resolution vertical profiles of wind speed, pressure, humidity and temperature in the lower and middle atmosphere measured by instrumented balloons with sensors have been used in studies of small-scale structures in the atmosphere. Barat (1982) deduced the kinetic energy of turbulence, ε, from spectral analysis (and also by

structure function analysis) of wind velocity. His observations showed that turbulence is intermittent. He also suggested that breaking of gravity waves into turbulence plays an important role in stratospheric mixing. However, estimation of ε may be biased by wind shear (change of wind speed with height) in balloons or aircraft measurements (Barat and Bertin, 1984). Meillier et al. (2008) investigated the possibility that gravity waves are the cause of turbulence patches in the nocturnal boundary layer of the atmosphere. More detailed analysis of boundary layer turbulence by balloons (Balsley, 2006) showed that the top of the boundary layer can be estimated in terms of a significant decrease in ε.

While spectral analysis is the method that atmospheric scientists mainly use to deduce turbulence from in-situ measurements, the direct estimation of turbulence by measuring the Thorpe length (Luce et al., 2002; Gavrilov et al., 2005; Kantha and Hocking, 2011) which is based on the reordering of temperature profiles, has been used as an alternative method.

Radars have become important tools in studying the dynamics and fine-structure of the atmosphere. Many turbulence studies have been undertaken using radars (Gage et al., 1980; Balsley and Gage, 1980; VanZandt et al., 1978; Hocking and Mu 1997; Nastrom and Eaton, 2002). The half-width of the radar spectrum contains useful information on turbulence, and the spectral-width method uses this information to estimate ε. Hocking (1983) investigated the spectral "contamination" (i.e. effect of beam-width, pulse length and wind shear) of radar backscatter from turbulent patches and developed a formula for estimation and removal of these contaminations (due to non-turbulent effects). A more comprehensive form of this formula was introduced in 2003 by the same author. Nastrom (1997) developed another formula for calculation of non-turbulent effects. The spectrum-width method occasionally produces negative turbulent energy dissipation rate, ε (Nastrom and Eaton, 1997; Jacoby-Koaly et al., 2002; Narayana Rao et al., 2001) and this needs to be examined further. This will be an important focus of this thesis.

Aircraft measurements have been one of the most reliable sources of information on turbulence (Taylor, 1972; Fairall et al., 1980; Cornman et al., 1995). However, many authors use aircraft measurements to verify radar measurements. Comparisons between radar-retrieved ε and aircraft measurements, by Jacoby-Koaly et al. (2002) and Shaw and Lemone (2003), showed that there was a modest correlation between the two techniques. However, the measurements were made using radars with a broad beam, and the results are of questionable validity. Furthermore, it was found that on average, radar overestimates ε in the case of strong shear (Meischner et al., 2002).

In addition to ε, the refractivity structure function, C_n^2 is another useful parameter for studying turbulence. C_n^2 is a measure of the fluctuations of refractive index in the atmosphere. Numerous studies have been done on measurements of C_n^2 and estimation of ε from C_n^2 (Hocking, 1985; Hocking et al., 1986; Hocking, 1999).

In all approaches, it was assumed that turbulence is isotropic. However, it is possible that turbulence is anisotropic. Hence, the effect of anisotropy needs to be calculated and considered (Hooper and Thomas, 1995; Hocking and Hazma, 1996; Hocking and Rottger 2001; Nastrom and Tsuda, 2001, Hocking and Hocking, 2007).

Studies of the climatology of turbulence are also very important. Seasonal and diurnal variations of turbulence parameters such as energy dissipation rate, refractivity structure function and turbulence diffusivity were studied (Fukao et al., 1994; Nastrom and Eaton, 1997; Narayana Rao et al., 2001). Such studies are essential for an accurate evaluation of weather forecast models (Frehlich and Sharman, 2010).

1.6 Instrumentation and Methods

Turbulence is characterized by irregular random motions of eddies. For so-called "three-dimensional" turbulence, the larger eddies can have length scales of about 10^3 m, while the length scales of the smallest eddies are about 10^{-3} m, although exact values vary with height. Clearly, the spatial and temporal separations of eddies in a turbulent motion can be very small and it is often unresolved to observations. Although all measurement techniques attempt to determine turbulence at sufficient resolution, accurate estimation of turbulence is still very challenging.

Turbulence measurements can be carried out using radars and in-situ instrumentation such as balloons, rockets and aircraft. In this chapter, we will concentrate on radar and aircraft techniques and the methods which can be used to estimate the turbulent energy dissipation rate. The advantage of aircraft techniques is that they often provide us with higher resolution data. However, radars can record data continuously and for long periods of time. The obvious difference between radar and aircraft techniques is that while the instrumented aircraft has to fly directly through turbulent flow to measure turbulence, the radar is located on the ground and measures turbulence by receiving the reflection of a radar signal from turbulent patches in the atmosphere.

1.6.1 Radar Techniques

Radar stands for Radio Detection And Ranging. Radars were developed to detect and determine the range of aircraft using radio techniques, but they became a powerful tool in monitoring weather. They also have been used successfully to measure wind and turbulence in the atmosphere. Radars have a wide range of variability, depending on their application. Radars which operate in the frequency range 3-30 GHz and observe precipitation are called weather radars, but also can be called "precipitation radar" and even "Doppler radar". The radars generally have beams which point quasi-horizontally. In this thesis, we will use the term "Doppler radar" to describe any radar which has Doppler techniques, not just weather radar. Radars which are designed to directly observe backscatter produced by fluctuations of atmospheric refractive index are called atmospheric radars. These types of radars use HF (3-30 MHz), VHF (30-300 MHz) or UHF (300 MHz- 3 GHz) frequency bands and have a large vertical coverage.

The measurement techniques are similar in principle for both atmospheric and weather radars. In both cases, radio waves are radiated into the atmosphere by the radar transmitter and information will be extracted through the analysis of reflected radio waves from the target. However, the most important features which make atmospheric radars different from weather radars are the choice of frequency and methods of data analysis.

Wind profilers are atmospheric radars, designed to operate at 50-1000 MHz with vertical and non-vertical radar beams. Although wind measurement is the primary capability of wind profilers, they have several other measurement capabilities. Wind profilers can be used to measure turbulence in the atmosphere. They are also important tools in study of gravity waves, fronts and jet-streams. The advantage of using a wind profiler is that profiles of wind velocity and turbulence parameters can be measured more frequently compared to other techniques (i.e. balloons, aircraft and rockets).

1.6.2 Range and Range Resolution

Measurement of the distance to a target, or ranging, is one of the important characteristics of a radar. Ranging is made by measuring the time delay of the echo signal from the target with respect to the transmitted signal. This is one of the basic principles of radar operation.

In the lower and middle atmosphere, the speed of radio waves is approximately

equal to the speed of light, c. If a short pulse is transmitted and the backscattered signal from the object at R_0 can be detected at time delay t, and the range, R_0, can be estimated through (e.g. Sato, 1989):

$$R_0 = \frac{\mathrm{c}t}{2}, \tag{1.16}$$

where t is the of round trip between transmission and reception.

Radio waves are usually transmitted in short pulses of length $\triangle t$. The received echo from such a pulse also has a time duration of $\triangle t$. Therefore, the range resolution can be explained as if the target has a finite length of $\triangle R$:

$$\triangle R = \frac{\mathrm{c}\triangle t}{2}. \tag{1.17}$$

The range resolution can be improved by reducing $\triangle t$. However, by reducing $\triangle t$, wider filters are needed, since the noise contaminating the signal increases.

1.6.3 Radar Equation

In order to design a radar, it is important to know how strong the backscattered signal is. The relation between the transmitted and received power in a radar is determined through the radar equation. If we assume that power, p_t, is fed to a monostatic antenna (i.e. the transmitter and receiver are located together as one piece of equipment), the received power, p_r, from a hard target can be expressed as (Sato, 1989):

$$p_r = \frac{p_t A^2 e_R}{4\pi\lambda^2 R_0^4}\sigma_c, \tag{1.18}$$

where A is the effective area of antenna, e_R the loss factor which represents the attenuation of the received signal due to the antenna, transmission line, connects etc., λ the radar wavelength, R_0 the distance of the target from the antenna, and σ_c the cross section of the target illuminated by the radar beam.

For distributed targets, the total received power, p_r, is the sum of the echo power, p_t, scattered from individual targets. In this case, the radar equation for a bistatic antenna (i.e. the transmitter and receiver are separate) is given by (Hocking, 1985):

$$p_r = \frac{p_t e_R e_T G_T A_R}{4\pi R_0^2}\sigma_v \frac{\mathrm{V}}{\ln 2}, \tag{1.19}$$

where G_T is the transmitter gain (ability of the antenna to increase power in a certain

direction), A_R the effective area of the receiver and e_T the efficiency of transfer of power from the transmitter to the transmitting antenna, e_R the efficiency of transfer of signal from the antenna to the receiver, σ_v the power backscatterd per unit solid angle, per unit incident power density, and per unit volume and V is the volume illuminated by the radar beam.

1.6.4 Scattering Mechanism

Irregularities in the refractive index of the atmosphere cause radio waves to scatter. The refractive index of the atmosphere, n, can be written as (Gage, 1990):

$$n - 1 = \frac{3.73 \times 10^{-1} e}{T^2} + \frac{77.6 \times 10^{-6} p}{T} - \frac{\mathrm{N}_e}{2\mathrm{N}_c}, \tag{1.20}$$

where p (millibar) is the atmospheric pressure, e (millibar) the partial pressure of water vapor, T (Kelvin) the absolute temperature, N_e (m^{-3}) the number density of electrons, and N_c (m^{-3})= $1.24{\times}10^{-2} f^2$ (MHz^2) the critical plasma density for the frequency f. The contribution of each term to the refractive index is not the same for different regions of the atmosphere. The atmosphere is often divided into the four regions of troposphere, stratosphere, mesosphere and thermosphere (from 80-120 km; not shown in Figure 1.2) according to the temperature structure (see Figure 1.2). The first term in the right side of the Equation (1.20) is due to water vapor and dominates in the lower troposphere. The second term contains the contribution due to dry air and tends to be dominant in the upper troposphere and stratosphere. The third term depends on the density of electrons and becomes important above 70 km.

Variations in atmospheric properties, such as temperature, pressure and water vapor, produce inhomogeneity in the refractive index which scatters the radio wave. The majority of scattering is due to small scale variations of the refractive index, which are caused by small scale fluctuations of temperature, pressure, water vapor, etc (Doviak and Zrnic, 1984).

Inhomogeneities can be due to turbulence, but may also occur due to other processes which can lead to horizontally stratified reflectors. Fresnel scatter, or specular reflection, is another mechanism responsible for partial reflections in a radar beam from sharp vertical changes in refractive index which are horizontally extended. These reflecting layers are generally caused by horizontally stratified temperature discontinuities in the atmosphere. The process is also called partial reflection, because only a small fraction of the signal power is reflected. Fresnel reflection is aspect sensitive (i.e. the backscattered signal power for a vertically directed beam is significantly greater

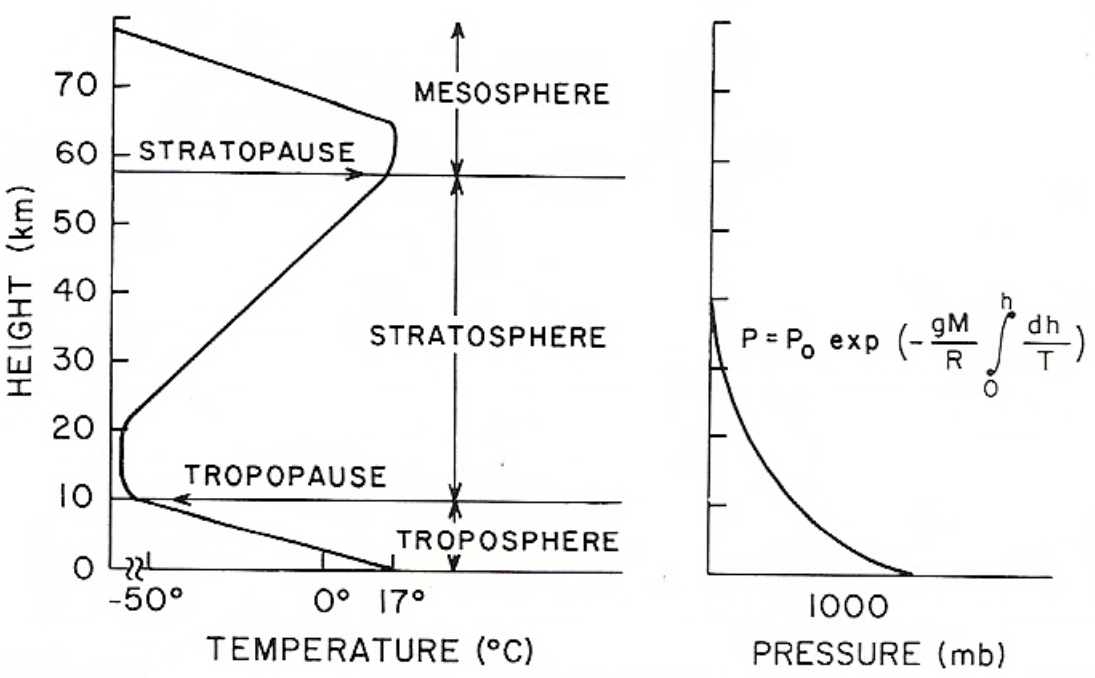

Figure 1.2: Vertical profiles of temperature (left) and pressure (right) in the atmosphere (from Doviak and Zrnic, 1984).

than off-vertical beam at the same altitude), since reflected echoes due to this process are much stronger with a vertical radar beam (Gage, 1990).

1.6.5 Doppler Radar

It was discovered by Christian Doppler that the shift in frequency caused by moving sources of sound was proportional to the speed of the source. This effect is called Doppler shift. The same effect occurs when sound waves are reflected from a moving target.

Doppler radars use the Doppler shift to detect motion. They not only measure the power received from a target, but they also measure the rate of motion of the target toward or away from the radar. When a target moves toward a radar, the frequency of backscattered signal is increased. When the target is moving away from the radar, the frequency is decreased. The radar then compares the received signal with the frequency of transmitted signal and measures the shift, giving the radial speed of the target.

Doppler radars primarily detect the echo that returns directly along the radar beam, therefore they can only measure the component of the motion along the radial axis. This component is called the radial velocity, u_r and is related to the Doppler

shift frequency, f_d through the following equation (Sato, 1989):

$$f_d = \frac{2f}{\mathrm{c}} u_r, \tag{1.21}$$

where f is the frequency of radar.

A typical value of f_d for the radar frequency of 50 MHz and radial velocity of 10 m/s is about 3 Hz. The typical bandwidth of transmitted pulses is 100 kHz-1 MHz. In addition to the Doppler shift, Doppler radars also measure phase shift. In this method, the phase difference of the time series of echos from consecutive transmitted signal separated by the period of T_p is calculated. Then the radial velocity can be estimated through the relation (Sato, 1989):

$$\triangle\Phi = \frac{4\pi f T_p}{\mathrm{c}} u_r, \tag{1.22}$$

where $\triangle\Phi$ is the phase shift.

1.6.5.1 The Doppler Beam Swinging Method

Doppler radar can only measure the projection of the wind velocity vector along the radial direction of the radar beam. The Doppler Beam Swing (DBS) determines horizontal and vertical wind speeds by steering the radar beam and measuring radial velocity in different directions.

Figure 1.3 shows the principle of the DBS method. The radial projections of horizontal and vertical wind velocities, u_p and w_p are measured at two zenith angles of α and -α. Therefore, the horizontal velocity, u and vertical velocity w are given by (Rottger, 1989):

$$u_p = \frac{V_1 - V_2}{2\sin\alpha}, \tag{1.23}$$

$$w_p = \frac{V_1 + V_2}{2\cos\alpha}, \tag{1.24}$$

where $V_i = u_p + w_p$ and indices 1 and 2 are indicators of beam directions at zenith angles of α and -α. It should be noted that this method assumes a uniform velocity field above the radar. Hence, it is important to choose the zenith angle properly. Sometimes the method is simplified further by using $w = 0$.

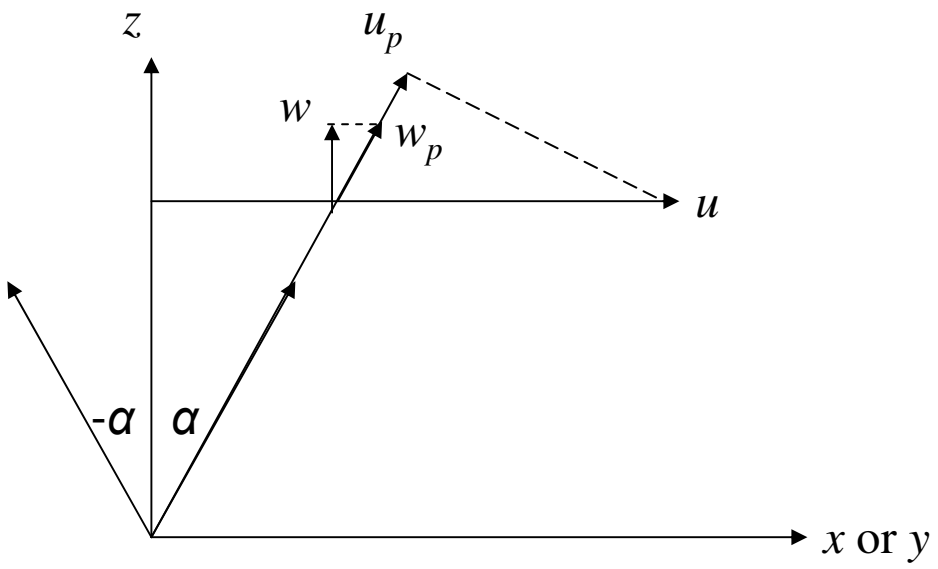

Figure 1.3: Schematical diagram of the Doppler Beam Swing (DBS) method. In this figure, α and $-\alpha$ are zenith angles.

1.6.6 Signal to Noise Ratio

Noise appears as random variations in the echo signal received by the radar. Noise is caused by internal sources (e.g. electronic components of radar) and external sources (e.g. thermal radiation in nature, man-made interference, etc.). The noise power, p_n, can be estimated by (Keeler and Passarelli, 1990):

$$p_n = kT_sB_s, \tag{1.25}$$

where k is the Boltzman constant, T_s the temperature of the system and B_s the total bandwidth of the system, and where the term T_s derives from internal noise, receiver noise, sky noise, and man-made noise. Therefore, the system noise is defined by the antenna design, radar location, and frequency bandwidth.

Signal to noise ratio (SNR) is a measure of signal strength relative to background noise. SNR is defined as:

$$\text{SNR} = \frac{p_r}{p_n}, \tag{1.26}$$

where p_r is the received signal power given by Equation (1.19) and p_n is the measured noise power defined by Equation (1.25). The SNR can be improved by increasing the pulse length, however this reduces the range resolution.

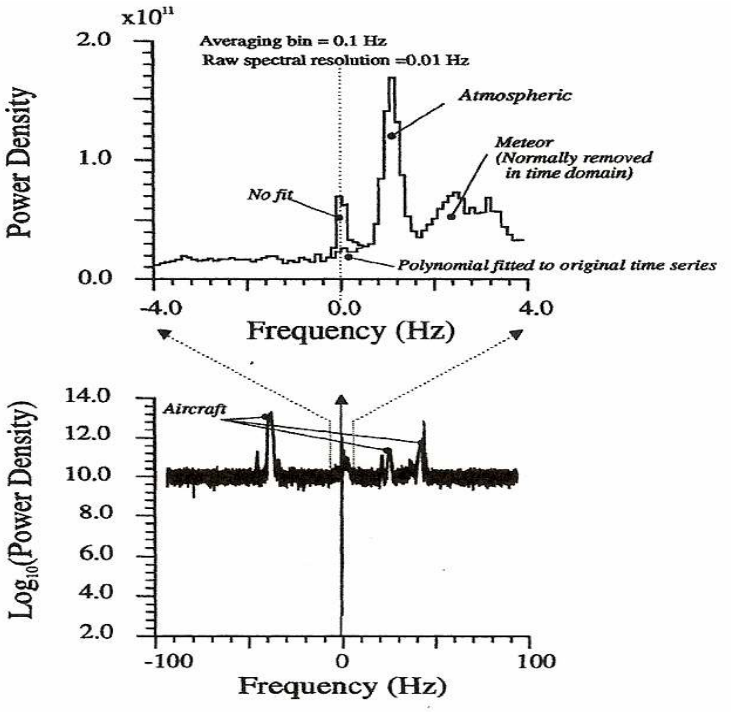

Figure 1.4: Contribution of aircraft and meteors to a radar signal. The lower graph shows the whole spectrum while the upper shows only the central ± 4 Hz of the spectrum (from Hocking, 1997).

1.6.7 Radar System Description

Three main radars are used in this study: radars at Walsingham, Harrow and Negro Creek, all in Ontario, Canada. Typical parameters are given for the Walsingham radar in Table 1.1, but many of the features, such as peak power, measurement mode, duty cycle, height resolution, numbers of beams and ranges covered, are common to all radars. The radars are separated by typically 200 km.

The first step in data analysis is to remove meteors and aircraft noise in the time domain. Meteors occur in the signal because the radars often use a reflection frequency in excess of 3000 Hz, so meteors at typical ranges of 200 km are often range-aliased and can appear at heights of 1-15 km. Aircraft and meteors amplitudes increase in a short period of time, and therefore can be removed by a search algorithm which searches for strong falling signals (see Figure 1.4). Then a polynomial fit is applied to the raw data to remove effects of very specular, slowly fading echoes.

The next step is to produce a spectrum and to search for spectral peaks. In particular, it is important to notice the aliasing frequency used. Data are typically recorded at 1000-3000 Hz, depending on the radar operation mode, but coherent

Title	Value
Location	Walsingham: 42.637°N;80.573°W
Operating frequency	44.5 MHz
One way half-power half-beamwidth	2.3°
Total area of antenna field	4000 m^2 (partially filled)
Mean power	3200 W
Peak power output	40 kW
Gain	25 dB
Wind measurement mode	Doppler
Pulse length	500 or 1000 m
Mean power aperture product	1.6×10^7 Wm^2
Duty cycle	5-10 %
Height resolution	0.5-1 km
Number of beams	5(Vert.+10.9°off-vert. to N,S,E,W)
Range (off-vertical beam)	0.4-14 km
Range (vertical beam)	0.4-14 km
Digitizer aliasing frequency	$>$ 100 Hz

Table 1.1: The Walsingham radar parameters

integration is only performed over typically 16 data points, so the frequency range in the spectral domain is of the order of 30 to 100 Hz. This has many advantages in regard to rejection of interference and dealing with noise. For example, aircraft peaks are easily removed from the signal, since they generally have large velocities and therefore are shifted out to the higher frequency regions of the spectrum, which are of no interest for atmospheric work. After producing a spectrum, a suitable spectral peak is chosen and a Gaussian fit is applied in this region of the spectrum. The spectral offset, peak value and spectral width are determined and used to estimate the radial velocity and turbulence (Figure 1.4).

The most important differences occur in the antenna configuration and subsequent beam widths. Figure 1.5 shows the main two designs used by the radars. The design used at Walsingham is shown in Figure 1.5(a), and can be seen to be a large cross-structure. It will be referred to as a "type-I" design. The layout used at Harrow and Negro Creek is shown in Figure 1.5(b), and is more compact; it is referred to as a type-II radar.

Due to the larger cross structure, the Walsingham radar has a narrower main beam than the other radars, though it has larger sidelobes (sidelobes surround the main beam and contain very low power densities). The Negro Creek radar has a spacing of

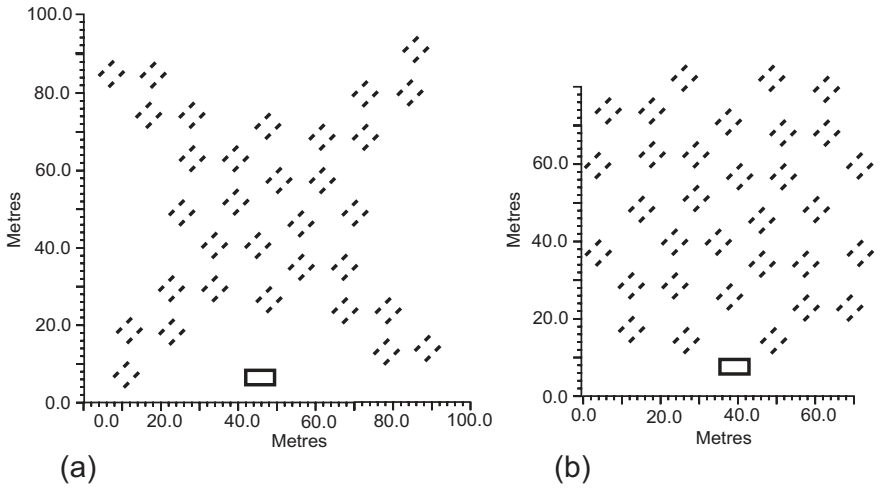

Figure 1.5: Layout of the antennas in the arrays discussed. (a) shows a type-I radar, and (b) shows a type-II radar. Antennas are clustered in groups of 4 (quartets) with separations of a half-wavelength between antennas. Quartets are positioned so that they are 1.5 wavelengths diagonally centre-to-centre. In each case there are 128 antennas.

Radar parameters	Walsingham	Harrow	Negro Creek
Location	42.637°N; 80.573°W	42.039°N; 82.892°W	44.632°N; 80.859°W
Operating frequency	44.50 MHz	40.68 MHz	48.92 MHz
One-way half-beamwidth	2.3°	2.75°	3.30°
Two-way half-beamwidth	1.63°	1.95°	2.34°

Table 1.2: Radar parameters

only 1.25 wavelengths diagonally between quartets (in contrast to the more common spacing of 1.5 wavelengths diagonally for this radar-type), and so has a broader main beam than any of the other radars. Harrow has an intermediate beam width (see Table 1.2). The radar beams are steered to 4 azimuthal directions sequentially and then vertical. One complete cycle takes typically 5 minutes.

1.6.8 Methods

There are two main methods that can be used to estimate turbulence from radar measurements: the refractivity structure function method and spectral-width method. The first method estimates the refractive index structure constant, C_n^2, which is a measure of the refractive index fluctuations induced by turbulence. When C_n^2 is measured, it is then converted to ε, but the conversion makes several assumptions. The second method (spectral-width method) estimates more directly turbulent energy dissipation, ε, which is a measure of the intensity of turbulence in the atmosphere. The latter method is the method of our interest in this study, however we will review both methods.

1.6.8.1 Refractivity Structure Function Method

The backscatter of radio wave from the turbulent patches is caused by the inhomogeneities in the refractive index produced by turbulence. Refractive index structure constant, C_n^2, is a measure of variability of refractive index in the atmosphere and is given by (Hocking and Mu 1997):

$$C_n^2 = 66.4 \frac{p_r Z^2 \lambda^{1/3}}{p_t A e_R^2 \alpha_t \left(0.5 L_t\right)}, \tag{1.27}$$

where p_r is the received power, p_t the transmitted power, Z the distance to the scatterers from the radar, λ the radar wavelength, A the radar effective area, e_R the loss factor which describes power losses in the cables, transmitter and receiver of the radar, α_t a factor that describes how the true gain of the radar beam is different from the ideal directivity (α_t is generally close to 1), and L_t the transmitted pulse length.

It should be noted that C_n^2 is not a measure of intensity of turbulence. However it is possible to convert C_n^2 to the turbulent energy dissipation rate, ε, which is a better estimator of the strength of turbulence. The relationship between C_n^2 and ε is given through (Gage et al., 1980 ; Hocking and Mu, 1997):

$$\varepsilon = \left(\gamma C_n^2 \frac{\omega_B^2}{F^{1/3}} M^{-2} \right)^{3/2}, \tag{1.28}$$

where $\gamma \approx (0.7)^{-1}$, F is the fraction of the radar volume filled by turbulence, ω_B the Brunt-Vaisala frequency and M the potential refractive index gradient.

The Brunt-Vaisala frequency is the frequency at which an air parcel oscillates in the atmosphere and is given by (Holton, 1992):

$$\omega_B^2 = g \frac{\partial \ln \theta_p}{\partial z} \tag{1.29}$$

where g is the gravity acceleration, θ_p the potential temperature and z the height.

The potential refractive index gradient, M depends on the variation of potential temperature, θ_p and humidity, q as a function of height and is given by (Vanzandt et al., 1978):

$$M = -77.6 \times 10^{-6} \frac{p}{T} \left(\frac{\partial \ln \theta_p}{\partial z} \right) \times \left[1 + \frac{15500\, q}{T} \left(1 - \frac{1}{2} \frac{\partial \ln q / \partial \ln z}{\partial \ln \theta / \partial \ln z} \right) \right], \tag{1.30}$$

where p is the pressure in millibars and T the absolute temperature. Note that the humidity term in the bracket is dominant in the lower troposphere (below 10 km).

Measurements of energy dissipation rate using refractivity structure function method requires measuring temperature, pressure and humidity (usually determined by balloons) which makes the technique more complicated.

1.6.8.2 Spectral-Width Method

Patches of turbulence in the atmosphere contain irregularities which produce signal backscatter. For VHF radar, the spatial scale of $l = \lambda/2$ (the so-called Bragg scale) determines the backscattering from isotropic turbulence; that is the radar detects velocity spectra associated with eddies with the range scale of half the radar wavelength ($l \sim 3$ m) up to the volume thickness (500 m) sampled by radar. Therefore, the VHF radar can measure turbulence of scale sizes that approximately covers the entire inertial subrange. It should be noted that the irregularities in the turbulent patches may be anisotropic, but are often considered as isotropic. If it is assumed that radar observes the entire inertial subrange which obeys Kolmogorov theory, then the relationship between the standard deviation of the radial velocity, σ_t, and turbulent energy dissipation rate, ε, can be written as (Hocking, 1999):

$$\sigma_t^2 \propto \int_{k_B}^{k_v} \varepsilon^{2/3} k^{-5/3} dk, \tag{1.31}$$

where, k is the wavenumber of the spectrum, and k_v and k_B are the highest and lowest wavenumbers of the inertial subrange respectively.

Using Equation (1.31), we can extract ε through (Hocking, 1999):

$$\varepsilon \approx C \omega_B \sigma_t^2, \tag{1.32}$$

where C is a constant and ω_B the Brunt-Vaisala frequency. We will discuss the above equation and estimation of σ_t^2 in more detail shortly.

Time series of data — typically 20-40 seconds in duration — are collected and then spectrally analyzed. The resulting spectra are recorded, and their spectral widths determined. Determination of the spectral width is a key step. It is possible to find the variance of the signal using weighted moments, but a more rigorous procedure is to use spectral fitting. Use of weighted moments is prone to error, since removal of the effect of noise is difficult. In such determinations, it is necessary to find the quantity $\int \left(f - \overline{f}\right)^2 P(f)\, df$, where f is the frequency, $\overline{f}$ is the mean frequency, and P is the power spectrum. If the power spectrum is non-zero across the whole frequency domain due to noise, and the noise is not properly removed, the above integral changes. Furthermore, if there are other interfering spectral components, such as those due to aircraft, meteors (aliased), radio interference, precipitation, etc., they will affect the determination of the spectral variance.

In our case, a Gaussian function is fitted to the spectrum, and a least-squares chi-square parameter, χ^2 is determined, as described by Bevington (1969), but adapted for real numbers. Then χ^2 can be calculated through $\chi^2 = \sum \frac{(\text{observed value-expected value})^2}{\text{expected value}}$, where in our case, the observed value is the measured spectrum and the expected value is the fitted Gaussian spectrum. The estimated χ^2 is compared to a critical value, χ_c^2.

Spectra which are bimodal, or have other non-atmospheric components such as aircraft and radio interference, are rejected, in preference to giving bad estimates. Use of a wide aliasing frequency, as discussed above, also helps produce better quality spectra. The Gaussian function used is of the form $A_0 \exp -(f - f_0)^2/2\sigma_f^2 + D_0$. A_0 is the amplitude, f_0 is the offset of the peak, σ_f is the standard deviation of the spectrum in Hz, and D_0 is an offset which varies according to the noise level of the spectrum. Increased noise increases the value of D_0 and also amplifies the variability of the spectral values relative to the Gaussian reference. Large levels of noise results in

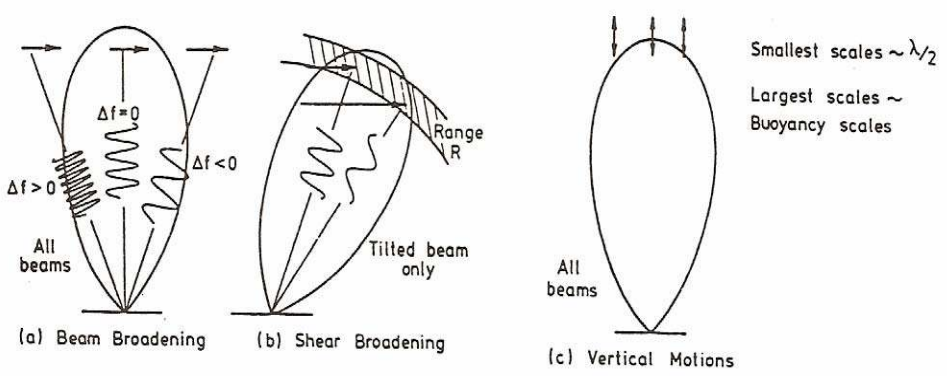

Figure 1.6: Different causes of beam broadening in radar (from Hocking, 1983).

large values of D_0 and increased χ^2 values. Spectra that have a modified chi-squared parameter that exceeds a specified limit χ^2_c are rejected. This includes rejection of spectra contaminated by interference.

Because of our use of this fitting procedure, the effects of poor signal to noise ratio (SNR) are reduced - spectra for which the signal is noisy simply do not pass these initial tests and are not included in further analysis. Hence studies of SNR need not be a major focus of this work. Our fitting procedure also ensures that we do not accept spectra which are bimodal or show other strange characteristics.

Once an experimentally determined spectral width has been found, the next step is to find a so-called "non-turbulent" (or "beam-broadened" or "beam-shear-broadened") contribution, so that the turbulence contribution can be calculated. Figure 1.6 illustrates the non-turbulent effect schematically. It can be seen from this figure that scatterers in different parts of the polar diagram of the radar produce different Doppler shifts, resulting in a broad spectrum. Figure 1.6(b) also shows the shear broadening effect, where changes in horizontal wind speed with height also produce Doppler shifts which broaden (or in some cases narrow) the spectrum. Spectral broadening due to vertical oscillations of scatterers is shown in Figure 1.6(c).

The details of the determination of the non-turbulent contribution will be discussed shortly, but for now we note that the turbulence contribution (the spectral half-power half-width that would be recorded if the beam-broadening contributions did not exist) is given by the following formula:

$$f^2_{turb} = f^2_e - f^2_{nt}, \tag{1.33}$$

where f^2_{turb}, f^2_e and f^2_{nt} are the squares of the spectral half-power half-width due to turbulence, experimental measurements and non-turbulent effects respectively. Some-

times, this is written in the form:

$$\sigma_t^2 = \sigma_e^2 - \sigma^2, \tag{1.34}$$

where σ_t^2 is the variance of the radial velocity fluctuations (which can generally be considered as approximately the variance of the vertical velocity fluctuations), σ_e^2 the experimentally determined spectral variance, and σ^2 the variance expected due to beam-broadened effects. Note that the latter term has no subscript. The term σ^2 relates to f_{nt}^2 through the relation $\sigma^2 = \left(\frac{\lambda}{2}\right)^2 \frac{f_{nt}^2}{2\ln 2}$.

The relation between the energy dissipation rate and f_{turb} is given by Equation (1.32) and can be written as (Hocking, 1983; Hocking, 1999):

$$\varepsilon = C\sigma_t^2\omega_B = C\left(\frac{\lambda}{2}\right)^2\left(\frac{f_{turb}^2}{2\ln 2}\right)\omega_B, \tag{1.35}$$

where λ is the radar wavelength and ω_B the Brunt-Vaisala frequency which is given by Equation (1.29). Hocking (1983) gave $C = 0.49$, but assumed that the radar measured the longitudinal velocity, and guessed about the relative contributions of turbulence and larger scale contributions to the spectrum. A more thorough analysis in Hocking (1999) recognizes that the radar measures the transverse component, giving $C = 0.27$. We will therefore use this value for C. An alternative expression for ε is therefore:

$$\varepsilon = 1.7\sigma_t^2/T_B \tag{1.36}$$

We will use this expression for our analysis. Here, T_B is the Brunt-Vaisala period. To begin, we will use the climatological values for T_B. The climatological value of ω_B is approximately 0.01 Hz ($T_B = 10$ min) in the troposphere and 0.02 Hz ($T_B = 5$ min) in the stratosphere. We will discuss about this in more detail in Chapter 4, and we will present the values of ω_B estimated for various conditions at our radar sites.

If it is assumed that only beam broadening contributes to the width due to non-turbulent effects, then the beam-broadened spectral width, is approximately given by (Hocking, 1985):

$$f_{nt}^2 = (1.0)\left(\frac{2}{\lambda}\right)^2 \Theta_{1/2}^2 u_0^2, \tag{1.37}$$

where u_0 is the total wind speed (assumed uniform with height in this simple equation), λ the radar wavelength and $\Theta_{1/2}^2$ the half-power half-width of the effective (two-way) radar beam. However, even at that time, Hocking did not recommend simple use of this formula, which was meant as a guide – a more thorough calculation

that recognized that the wind varied across the pulse length was recommended.

Nastrom (1997) looked specifically at the effects of a shear in the wind, and gave the following analytical expression for determination of the non-turbulent spectral variance:

$$\begin{aligned}\sigma^2 \approx & \frac{v^2}{3}u_0^2\cos^2\alpha - \frac{2v^2}{3}\sin^2\alpha\left(u_0\frac{\partial u}{\partial z}R_0\cos\alpha\right) \\ & + \frac{v^2}{24}\left(3+\cos 4\alpha - 4\cos 2\alpha\right)\left(\frac{\partial u}{\partial z}\right)^2 R_0^2 \\ & + \left(\frac{v^2}{3}\cos 4\alpha + \sin^2\alpha\cos^2\alpha\right)\left(\frac{\partial u}{\partial z}\right)^2\frac{(\Delta R)^2}{12},\end{aligned} \tag{1.38}$$

where v is the one-way half-power half-width, α the zenith tilt angle, u_0 the wind speed, $\frac{\partial u}{\partial z}$ the vertical shear of horizontal wind speed, R_0 the range, and ΔR the range resolution. The first term is only due to beam-broadening and the last term is only due to shear-broadening. The terms in the middle are due to both beam and shear-broadening. Hocking (1983) used a numerical model which uses the full wind profile to estimate the beam-shear-broadening, which was further expanded upon in Hocking (2003). The scattered power received in the velocity range u to $u+du$, at range R_0, is given by:

$$S\left(u,R_0\right)du = \int P\left(\alpha,\phi\right)\left[\sigma_s/r^2 * g\left(r\right)\right]d\Omega. \tag{1.39}$$

Here, the integral is between minimum and maximum possible values of ϕ. $S(u,R_0)$ is the received spectrum, P the combined transmitter and receiver polar diagram for the radar which is a function of zenith angle, α and the azimuth angle, ϕ. σ_s is the backscattering cross-section per unit volume (not to be confused with the spectral variances) and $g(r)$ defines the pulse shape as a function of range, r. The symbol "*" represents a convolution (The convolution of $f\left(r\right)$ and $g\left(r\right)$ is defined by: $f\left(r\right) * g\left(r\right) = \int_{-\infty}^{+\infty} f\left(x\right)g\left(r-x\right)dx$). R_0 is the lag in the convolution, and corresponds to the range at which S is detected by the radar. $d\Omega$ is defined by the following equation (Hocking, 1983):

$$d\Omega = \left(\tan\alpha\right)du\,d\phi/\cos\left(\phi-\phi_0\right), \tag{1.40}$$

where ϕ_0 is the direction of horizontal wind. Therefore, the spectral width can be estimated for any given range, wind speed and direction. In order to consider the

vertical wind gradient, the layer of interest is divided to small sub-layers with constant wind speed and direction. The sum of the all the spectra due to the full wind profile gives the theoretical spectrum expected due to non-turbulent effects. With our radars, this integral has been parametrized with look-up tables in such a way that it can run in real time, and this will be further described in Chapter 3. There are differences between the algorithms discussed above for determining the instrumental spectral width, and we will examine these differences in the next chapter.

1.6.9 In-situ Techniques

High-resolution measurements of turbulence are possible using in-situ techniques. The essential characteristic of these techniques is that measuring instruments like anemometers, soundings and accelerometers are mounted on special structures such as towers, balloons and aircraft. In the case of towers, the measurements are absolute in a coordinate system fixed to earth, in contrast to aircraft or sounding balloons in which the instrument is moving with respect to ground. Measurements by towers are generally limited to heights close to the surface. Sounding balloons can be used to measure turbulence into the middle atmosphere (~ 40 km), however the displacement of the balloons needs to be determined by radar from the ground or GPS. A great percentage of in-situ measurements are obtained by aircraft. These aircraft are equipped with meteorological instruments that record thermal and dynamics characteristics of the atmosphere over a wide range of altitudes. We will employ such methods later in this thesis. Therefore, in the following subsections, we will discuss about aircraft methods of measuring turbulence in the atmosphere.

1.6.10 Aircraft Techniques

In order to measure turbulence, some research and commercial aircraft are instrumented with Integrated Navigation System (INS), which is a navigation system. INS uses a computer and motion sensors, such as accelerometers, to estimate the position and acceleration of the aircraft in the atmosphere. In order to find the linear acceleration of the system, navigation systems are also equipped with an accelerometer, which estimates the acceleration in the inertial reference frame fixed to the system. Therefore, the acceleration is measured relative to the moving system. The initial position of the aircraft is provided by another source such as GPS and after that the system updates its position and velocity by integrating information received from motion sensors. The advantage of this technique is that it needs no external refer-

ences to determine its position or velocity once it has been initialized. However, the disadvantage of these systems is that any small errors in the measurements of position or acceleration are accumulated by integration and increase with time.

It is also possible to measure the position and velocity of aircraft using satellite navigation systems such as GPS systems. This information can be used as backup or can be combined properly to INS information to reduce the errors. The accuracy of GPS measurements does not depend on the duration of operation. However, a serious problem with this system is the possibility of signal outages caused, for example, by antenna shading (Kaniewski, 2006).

The INS/GPS system measure the velocity of the aircraft relative to the ground. However, the goal is to determine the velocity of the air motion with respect to the ground. The true wind velocity can be derived from the vector difference between the air velocity relative to the aircraft and the aircraft velocity relative to the ground. The aircraft is equipped with pressure transducers which measure the total pressure and static pressure. The total pressure is made up of dynamic pressure and static pressure. The static pressure is always present whether the aircraft is moving or at rest. The dynamic pressure is due to air motion and is only present when the aircraft is moving. Therefore, by subtracting the static pressure from total pressure, the dynamic pressure and subsequently the velocity of air motion will be determined.

1.6.11 Methods

Extracts of the turbulent energy dissipation rate, ε, from in-situ measurements is possible using statistical methods, such as spectra analysis (Quintarelli, 1993), structure function (Barat and Bertin 1983; Meischner 2001), autocorrelation and true airspeed-based approaches. The latter has been developed by the National Center for Atmospheric Research (Cornman, 1995) in order to measure ε from commercial aircraft measurements. In this study, we will use structure function and true airspeed-based methods to the measure energy dissipation rates from Twin Otter and commercial aircraft data respectively.

1.6.11.1 Structure Function

Kolmogorov theory (see section 1.4) assumes that the turbulence is statistically similar at different scales in the inertial subrange and therefore, turbulence is isotropic at this range. This means that turbulent parameters such as velocity are independent of the turbulence scale. This helps us to define the structure function method. There are

several structure functions, but the main ones are given as (e.g. Hocking, 1999):

$$D_{\parallel}(r) = \overline{\mid u_{\parallel}(x+r) - u_{\parallel}(x) \mid^2}, \tag{1.41}$$

$$D_{\perp}(r) = \overline{\mid u_{\perp}(x+r) - u_{\perp}(x) \mid^2}, \tag{1.42}$$

where it is assumed that we travel in a straight line in the turbulent medium and take measurements along the way. Measurements along the direction of motion are referred to "parallel" and measurements perpendicular to this direction are called "perpendicular". In Equations (1.41) and (1.42), u is the velocity, r the displacement and indices $\parallel$ and $\perp$ represent the parallel and perpendicular components relative to the probe trajectory respectively.

For the inertial subrange, the relationships between the structure functions and energy dissipation rate, ε, are given by:

$$D_{\parallel} = C_d r^{2/3} \varepsilon^{2/3} \tag{1.43}$$

$$D_{\perp} = \frac{4}{3} C_d r^{2/3} \varepsilon^{2/3} \tag{1.44}$$

where C_d is close to 2.0 (Caughey et al., 1978). It should be noted that sometimes the three-dimensional form of the structure function is used. In that case, the total structure function can be written as $D_{tot} = D_{\parallel} + 2D_{\perp}$, since there are two perpendicular and one parallel components.

The structure function method will be applied to wind data measured by Twin Otter aircraft in order to estimate the turbulent energy dissipation rate, ε (Chapter 5). The aircraft is instrumented to measure three components of wind speed over a frequency range from 0 to 10 Hz. One should note that it is not possible to have a frequency of zero, however, the frequency can be very small (corresponding to very long periods).

Furthermore, aircraft software employs complementary filtering routines such as the Kalman filter to improve the accuracy of measurements. In order to use Kalman filtering to remove noise from a signal, the measurements must be done in a linear system. In such systems, there is a linear relationship between measured values and the true values that need to be estimated. Many physical processes, such as a moving aircraft or vehicle, can be approximated as a linear model. A very simple form of the Kalman equation is given by (Simon 2001):

$$\mathbf{y}_k = C_k \mathbf{x}_k + \mathbf{z}_k, \tag{1.45}$$

The vector $\mathbf{x}_k$ contains all the information about the present state of the system, $\mathbf{z}_k$ represents the noise, C_k a matrix and $\mathbf{y}_k$ are the measured values. We can use $\mathbf{y}_k$ to estimate $\mathbf{x}_k$ values. However, $\mathbf{y}_k$ is contaminated by noise. Using the Kalman algorithm, it is possible to estimate $\mathbf{x}_k$ by making the assumption that the average of the state estimate is equal to the average of true values and the fact that we need an estimator that results in the smallest possible error variance.

1.6.11.2 True Airspeed-Based

True airspeed, V_t, is defined as the difference between the aircraft velocity (with respect to the ground), V_a, and the wind velocity, V_w. Therefore, we can write:

$$V_t = \left[(V_a - V_w)_x^2 + (V_a - V_w)_y^2 + (V_a - V_w)_z^2 \right]^{1/2}, \tag{1.46}$$

where x, y and z refer to parallel and perpendicular components of the velocity. Since the x component (parallel to aircraft trajectory) of the inertial velocity (with respect to the ground) is often much larger than other terms, Equation (1.46) can be written approximately as:

$$V_t \approx (V_a - V_w)_x \left[1 + \frac{1}{2} \frac{(V_a - V_w)_y^2 + (V_a - V_w)_z^2}{(V_a - V_w)_x^2} \right]. \tag{1.47}$$

The second term, in the square bracket, is typically much less than one. Therefore, the true airspeed is closely equivalent to the longitudinal component of the wind velocity, thus reducing to the following:

$$V_t \approx (V_a - V_w)_x . \tag{1.48}$$

Now, if we consider the fluctuations of the true airspeed, V_t' , we can write:

$$V_t' \approx \left(V_a - \overline{V}_a\right)_x - \left(V_w - \overline{V}_w\right)_x . \tag{1.49}$$

where $\overline{V_a}$ and $\overline{V_w}$ are the mean values of V_a and V_w respectively. If it is further assumed that fluctuations of aircraft speed are much less than fluctuations of wind velocity, then:

$$V_t' \approx \left(\overline{V}_w\right)_x - (V_w)_x = -\left(V_w'\right)_x . \tag{1.50}$$

Given the above assumption, the turbulent energy dissipation rate, ε can be estimated through the following equation (Cornman, 1995):

$$\phi_u(k_x) = \frac{18A\varepsilon^{2/3}k_0^{-5/3}}{55}\left[1+\left(\frac{k_x}{k_0}\right)^2\right]^{-5/6}, \tag{1.51}$$

where ϕ_u is the von Karman spectrum, A a constant, k_x the wavenumber along the motion (x axis) and k_0 is related to the gamma function, Γ and the longitudinal integral length scale, L_u through:

$$k_0 = \frac{\Gamma\left(\frac{5}{6}\right)\sqrt{\pi}}{\Gamma\left(\frac{1}{3}\right)L_u}. \tag{1.52}$$

In order to calculate ε values to a higher accuracy, a quality control test is performed on the data. A running-window median test is applied to the data. The window length is chosen to have enough points for statistical estimations and it is short enough to include changes in the data reasonably well. For each new set of data, the window is moved forward one step. Then the Z parameter is calculated through:

$$Z = \frac{y - y_m}{\max\left[y_u - y_l, \text{min-range}\right]}, \tag{1.53}$$

where y is the data point, y_m the median, y_u and y_l are the upper and lower percentile (i.e. 80 and 40) values of data over the window respectively. The variable "min-range" is chosen to prevent small variations in data. In the last step, the histogram of Z values is produced and outliers are determined and removed from the data.

Each ε estimate is calculated over 10 seconds. This is updated for every new set of data (e.g., 4 or 8 Hz). Then time series of ε values are generated for statistical estimations, and the mean and peak values of ε are reported every minute. In order to save communication costs, the turbulent energy dissipation rate is only reported if it exceeds a pre-determined value (e.g., "moderate" or "light-to-moderate").

1.7 Objective of this Thesis

The main objective of this thesis is the study of the major factors that can affect turbulent energy dissipation rate measurements using wind profiler radars and to develop ways to improve these measurements. We will apply the spectral width method to extract turbulence from the measured radar backscattered signal. The use

of this method is challenging, since weak turbulence or any errors can lead to negative apparent values of turbulence strengths.

Therefore, it is important to address and examine all the factors that can cause negative values of turbulence and to better estimate the errors associated with the procedure. This would allow a more reliable estimate of turbulence to be made by radar.

In order to achieve our goal, we have used radars at Walsingham, Harrow and Negro Creek, which are part of the O-QNet radar network. The radars measure both wind speed and turbulence in the lower atmosphere over the 1-10 km altitude range. Details about the radars and other methods of turbulence measurement are given in Chapter 1 of this thesis.

In Chapter 2, the data to be used are presented, and samples are given. These examples include negative values. Mean energy dissipation rates, both with and without negative values included, are displayed. Possible reasons for the negative values and major contributors to production of negative values of turbulence are introduced. We compare the earlier models and derive a formula which estimates turbulence more accurately. Applications of these formulations are demonstrated with real data. This chapter is an expanded version of a paper which has already been published (Dehghan and Hocking, 2011).

In order to determine turbulence, the Brunt-Vaisala frequency needs to be estimated. This is presented in Chapter 3, where the daily and monthly variations of the Brunt-Vaisala frequency in the lower atmosphere and mainly in the troposphere are also included.

In Chapter 4, our calculations of turbulence by radar are compared to turbulence values deduced from high-resolution aircraft measurements. The aircraft data include measurements by Twin Otter aircraft (provided by Environment Canada) around the upper boundary layer of the atmosphere, and data measured by commercial aircraft over the 1-10 km altitude range. In regard to the Twin Otter data, we have raw data sampled at a resolution of 10 Hz, and so can apply structure function procedures to estimate the strength of the turbulence. This method is applied to both longitudinal and transverse components of wind velocity measured by aircraft and compared to radar measurements. With regard to the commercial aircraft data (provided by the National Center for Atmospheric Research), we were not supplied with raw point-by-point velocity measurements, but rather were given estimates of the energy dissipation rates directly, which we can then compare to the radar data.

In Chapter 5, we discuss our results and present our conclusions.

Chapter 2

Instrumental Errors in Spectral-width Turbulence Measurements by Radars

Measurements of turbulent energy dissipation rates by radar spectral-width procedures requires differencing two numbers to produce a difference which is small relative to the two initial numbers. In particular, the square of a so-called "beam-broadening" component must be subtracted from the square of a measured spectral width. Because the difference is relatively small, it is very sensitive to statistical fluctuations in each of the initially measured parameters. The method by which the measured spectral width is determined can impact the accuracy of the measurements, and, in addition, the beam-broadened component is affected by errors in the measured wind, variability in the mean wind, wind-shear, and aspect-sensitivity of the scatterers. All these effects can impact the measurements of turbulence, and in some cases can even produce physically unrealistic "negative" values of turbulence strength. In this chapter, we investigate the relative importance of (i) variability of the mean wind within the averaging period, (ii) digitization errors and the accuracy of determination of the spectral width, (iii) the particular beam-broadening model employed, and (iv) anisotropy of the scatterers. Although these terms are often discussed in the literature, we have quantified their relative importance. The accuracy of determination of the spectral width is the most important source of error, followed by variability of the mean wind in the averaging period. In addition to these studies, we also develop a new formula for accurate determination of the beam-broadened spectral width. This includes a new term missing from earlier formulations.

2.1 Sample Data and Negative Turbulent Energy Dissipation Rate

In this section, we show some examples of energy dissipation rates deduced from radar measurements. In particular, we concentrate on July, 2007, during which a good range of atmospheric conditions occurred. We also look at negative values for turbulent energy dissipation rate, ε, in this time frame, and briefly investigate their impact. One word of warning needs to be noted. In this study, we used only data recorded with off-vertical beams, in order to avoid the effects of specular reflections. The vertical beam is almost always contaminated by scatterers and reflectors which are elongated horizontally, and behave in a manner different to isotropic turbulence, so we concentrate only on off-vertical beam data.

2.1.1 Typical Measurements

Figure 2.1 shows the wind speeds and directions for the month of July, 2007 measured with the radar at the Harrow site. For most of our analysis, we will concentrate on this data set, since most of the parameters that we need to discuss are well represented by it. Wind speeds varied between a few m/s to 30 and 40 m/s, giving a broad range of conditions. Measurements from the Walsingham radar will also be presented for July 2007, as required. The Negro Creek radar was not operational until late 2008, so when we need to do comparisons with Negro Creek we will use data from July 2009.

Figure 2.2 shows height-time plots of the strength of the turbulence throughout the month for a beam pointing to the north-west. The upper graph (denoted "model N") shows ε values produced assuming Equations (1.38) and 1.35 while the second one shows the energy dissipation rates determined using Equations (1.39), (1.40) and (1.35). The two sets of results are similar in general appearance. The third graph shows data recorded on a beam pointing to the North-east, orthogonal to the first. Again, the general appearance is similar to the other two, suggesting very little variation in azimuthal view-direction.

Figure 2.2 also shows the large dynamic range of turbulence in the atmosphere. Background values are generally of the order of 10^{-4} W/kg, consistent with Lee et al., 1988 (who catalogued an extensive group of in-situ measurements of turbulence strengths), and also with Hocking and Mu (1997). However, superimposed on this general background are short bursts of turbulence which rise well above 10^{-3} W/kg (red and black colors). These are consistent with so-called: "white-caps" bursts of

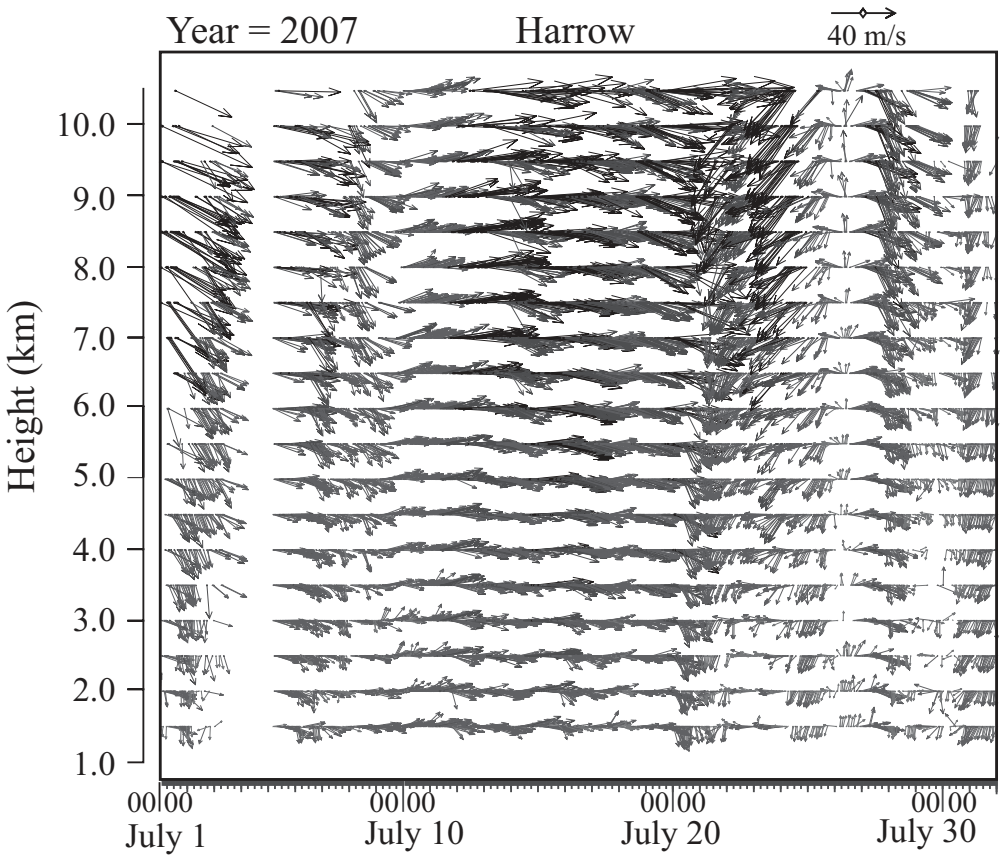

Figure 2.1: Plots of wind speed and direction recorded with the Harrow radar for the month of July, 2007. Vectors pointing to the top of the page represent a northward (southerly) wind, and vectors pointing to the right indicate an eastward (westerly) wind. Wind strengths are represented by the length of the vector, with the length of a vector representing 40 m/s shown at the upper right of the figure.

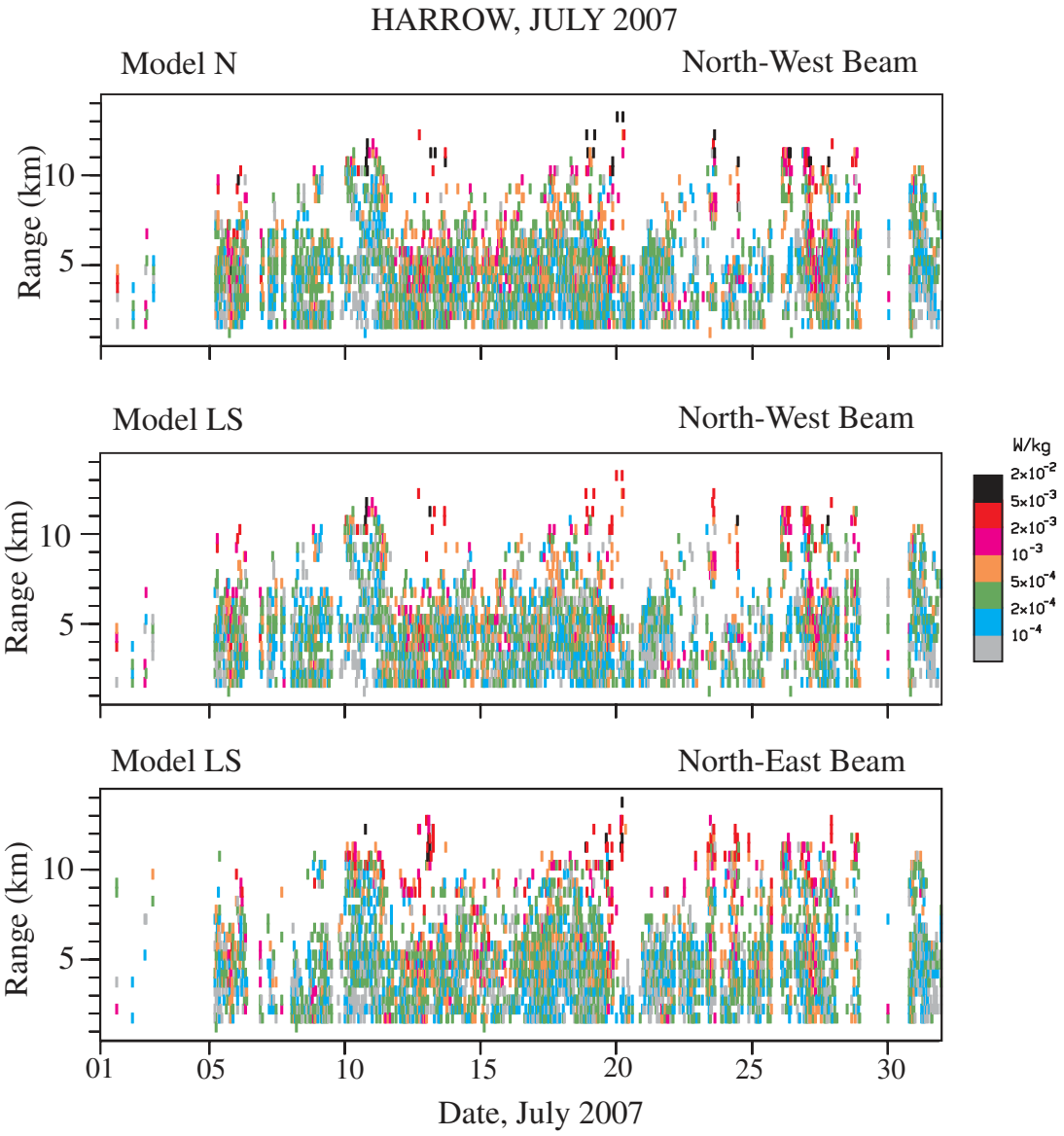

Figure 2.2: Height-time plots of the turbulent kinetic energy dissipation rate for the Harrow radar in July, 2007. The upper graph (labeled N) was calculated using Equation (1.38) for the beam-broadening term. The second graph was produced using a proxy for a fully numerical model (labeled "LS", for "layer-summing" method). Both of the upper graphs used data recorded with a beam pointing to the North-West at 10.9° from zenith. The lower graph shows data for an orthogonal beam pointed in the North-East direction, using the proxy for the numerical model.

strong episodes of turbulence, as described by Fairall et al., (1991), Hocking (1991), and Hines (1991). Despite the generally positive appearance of this data-set, however, one problem arises. A significant number of measurements of turbulence strengths show negative values (not plotted in Figure 2.2). These are physically unrealistic, and the cause of such values needs to be understood. In previous studies, the existence of such negative values has been mentioned (e.g. Nastrom and Eaton, 1997; Narayana Rao et al., 2001), but sometimes the chosen practice is to ignore them (e.g. Jacoby-Koaly et al., 2002, among others). This may be, or may not be, a valid practice, and needs to be investigated. Previous studies have discussed the cause of these values in a general sense, but not quantitatively. Our objective here will be a quantitative study of some of the more important potential reasons for these negative values.

Figure 2.3 shows the impact of these negative values. The figure displays vertical profiles of monthly averaged values of ε from 2 to 9.5 km for both the Harrow and Walsingham radars in July 2007 for two distinct cases. In the first case, averages are formed using only positive values of ε , while in the second case the averages include all measured values of ε, including the negative ones. It can be seen that from 2 km altitude to around 5-6 km, the two profiles are similar in magnitude (to within at least a factor of 2). However, above approximately 6 km, the two different sets of estimates diverge.

In order to further emphasize this effect, Figure 2.4(a) shows the percentage of negative measurements of ε as a function of height for the Harrow radar for July 20-31, 2007. We have performed these calculations using two different estimates of the beam-broadened spectrum. One profile (labeled N) uses the model of Nastrom (1997) (Equation (1.38) in this study). The other (labeled LS) uses a parametrization of the full spectral model developed using Equations (1.39) and (1.40). Below 5 km altitude, the percentages are approximately between 5 and 20%, but above this height they rise markedly, reaching 40% at 7-8 km. An exact description of the models N and LS will be given in section 2.2.

An immediate suspicion arises that the positive vertical gradient of percentages might be due to an increase in the SNR ratio, since scatter from the higher altitudes tends to be weaker, as is well known. But as discussed earlier, our use of fitting spectral procedures, and rejection of unsuitable or noisy spectra, makes this unlikely. An alternative possibility is that the increase in percentages is due to increasing wind speeds, since the vertical gradient of wind speed is positive for our data. In order to test this possibility, the turbulence strengths have been binned according to wind-speeds. Bins of 0-3, 3-6, 6-9 m/s etc., have been chosen, and then the percentage of

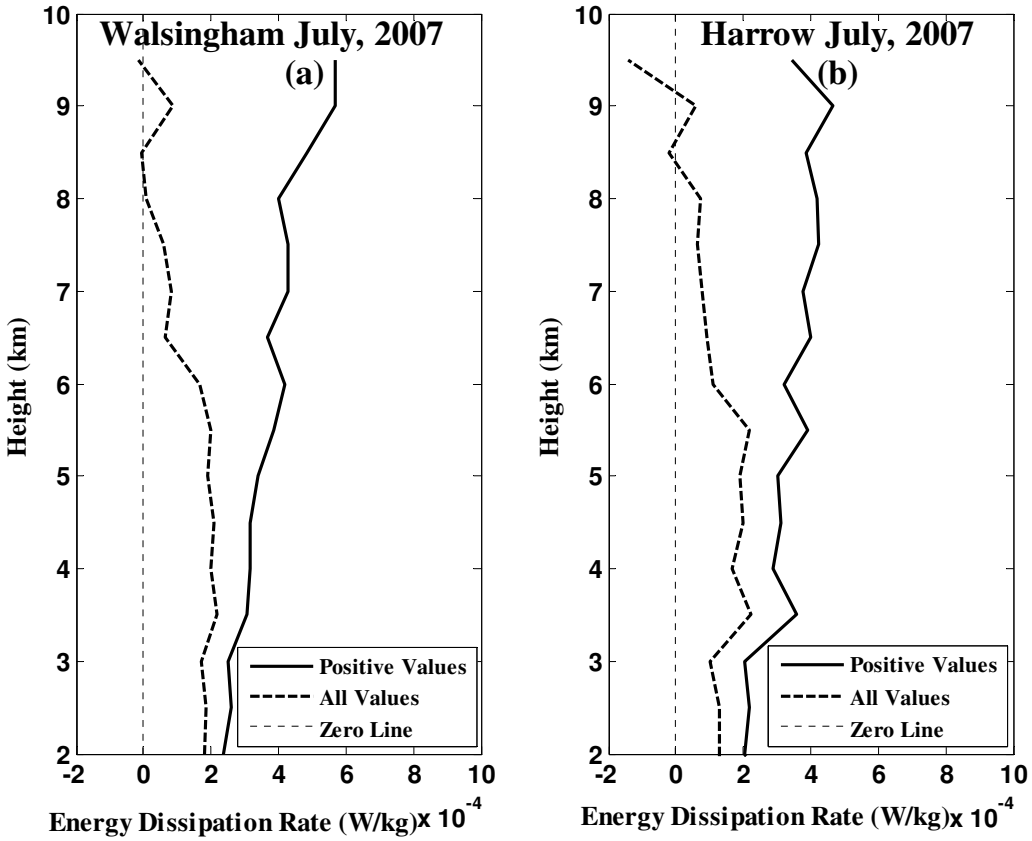

Figure 2.3: Vertical profiles of energy dissipation rate for the (a) Walsingham and (b) Harrow radars for July 2007, using all data (broken lines) and positive values only (solid lines).

negatives has been plotted as a function of height for each bin. The results are shown in Figure 2.4(b), using the "LS" model from Figure 2.4(a).

The individual profiles no longer show any significant variation with height, and clearly the percentage of negative values increases with greater wind speeds. Typical percentages are less than 10% for wind speeds less than 9 m/s, then rise to about 20% for winds of 9-12 m/s, 30% for winds of 12-15 m/s, and then above 15 m/s the percentages reach and exceed 40%. Other sites show the same effect. There is a slight decrease at 10 km, which may be due to the fact that some of the data at this height was stratospheric. In Figure 2.4(c), we have binned all the data from all heights (2-10 km altitude) together, but kept the separate wind-speed bins. The percentage of negative measurements clearly increases as a function of wind-speed, and the slope is least for the Walsingham radar (with the narrowest radar beam) and greatest for the Negro Creek radar (which has the widest beam). (The Negro Creek radar did not exist in 2007, so we have shown data for July 2009 as a proxy, as well as September 2008 to verify that the tendency to a larger slope is common to the Negro Creek radar). It is now necessary to turn to consider possible reasons for this dependence.

2.1.2 Possible Reasons for Negative Turbulence Strengths

In the previous section, the possibility that the SNR ratio might impact the percentage of negatives was largely ruled out. This is because of our use of a spectral fitting procedure. It may not be possible to ignore SNR issues if weighted moments are used for the determination of spectral widths, but that was not the case here. We now turn to other possible reasons for the negative turbulence strengths.

One commonly assumed reason for these negative estimates is that the scatterers are anisotropic, causing an effective beam that is narrower than the true beam-width. If the beam-broadening contribution is calculated on the basis of the beam-width of the radar, but no account is made for this anisotropy when the beam-broadened spectrum is calculated, the theoretical spectrum will be too wide, and may exceed the true spectral width, giving rise to negative values in Equation (1.33). Another commonly assumed reason relates to the temporal and spatial variability of the mean wind field over the radar. Over time scales of a few tens of minutes, and over spatial scales of a few kilometers, the wind field must vary. If a Doppler system is used to measure the mean wind field, it will be in part confounded by this effect. For example, the wind is measured at two different points in the sky by two different radar beams,

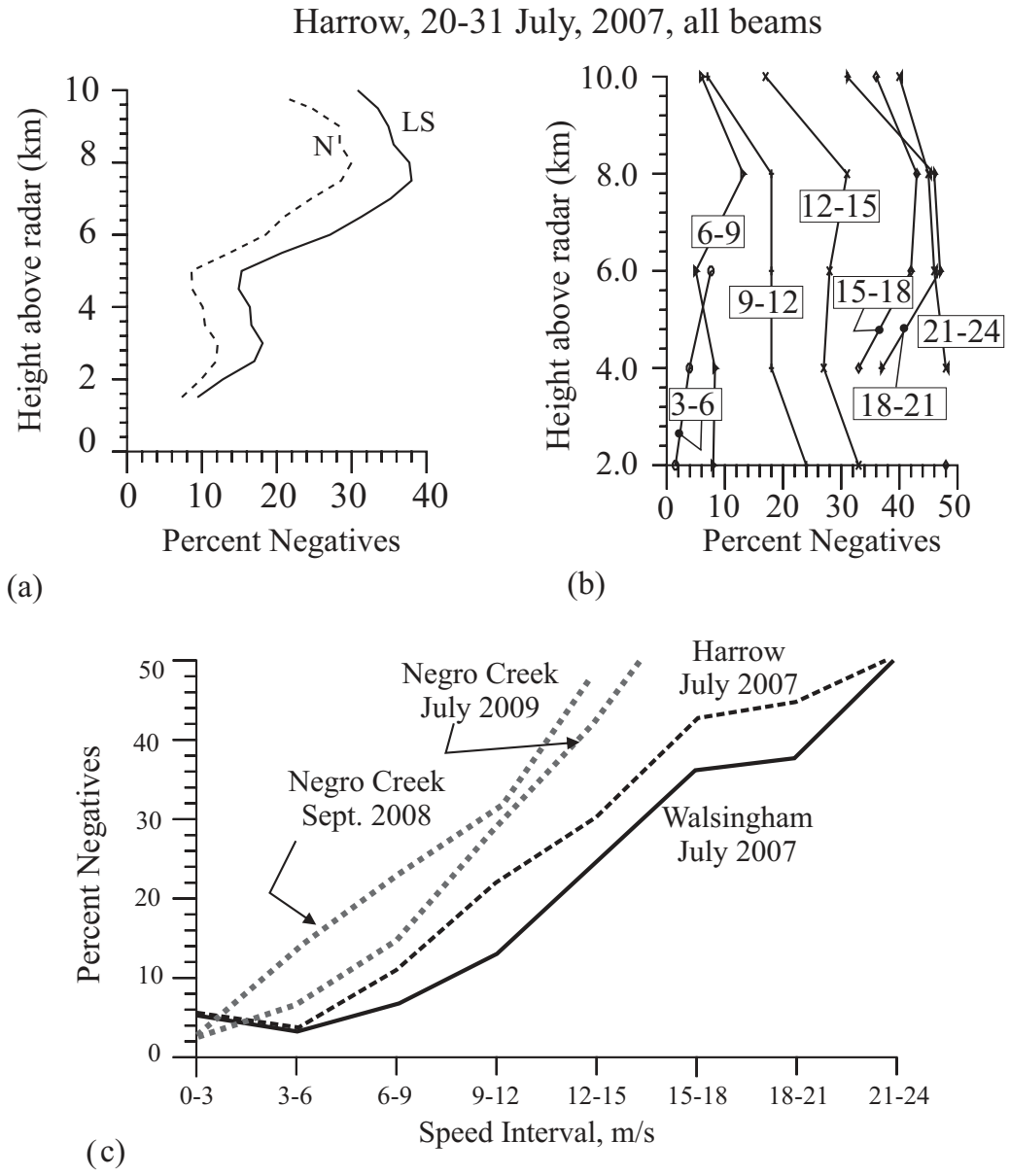

Figure 2.4: (a) Vertical profiles of percentage of negative turbulent energy dissipation rate, for the Harrow radar, 20-31 July, 2007, using models N and LS.(b) Percent of negative as a function of height after being classified into different bins based on total wind speed.(c) Plots of the percentage of negative ε values as a function of wind speed for 3 different radars, summed over altitudes from 2-10 km. Walsingham has a one-way half-power half-width of 2.3 degrees, Harrow has a value of 2.75 degrees and Negro Creek 3.3 degrees. Negro Creek had not been built in 2007, so we show July 2009 as a substitute, plus have added September 2008 in order to confirm that the Negro Creek radar generally has the largest percent of negatives.

and the measurements are at physically distinct locations, separated by typically 2-3 km or more. The wind field is also sampled at different times in these two beams. By combining the two radial velocities, a composite "mean wind" is determined, but it may not be a true reflection of the real wind — there may never really be such a thing as a true "mean wind". The wind calculated is only an approximation of the wind field at that time — albeit generally quite a good one. But if the strength of turbulence is determined for a particular beam at a particular height and time, yet the mean wind used for the calculation of the beam-broadened effect is an hourly mean, then there is a good chance that the true beam-broadened spectrum relevant at the time may have differed from the one determined using the assumed wind profile. Thus the beam-broadened spectrum used for turbulence extraction may be wider than the true one, reducing f_{turb}^2 in Equation (1.33), and possibly making it even negative. It is also possible that the beam-broadened component may be under-estimated, so that ε increases. This possibility has been discussed in the literature, but not generally quantified.

Another possible source of error is in the accuracy of determination of the spectral variance (or equivalently, the spectral width). This quantity is limited by a variety of effects, including the system resolution. Shorter data samples will have worse resolution — a 10 second data-set will have a resolution of only 0.1 Hz. Noise may further worsen the calculation. As discussed earlier, the variance determined by weighted moments tends to overestimate the true value unless done very carefully.

Another issue that could be important relates to the accuracy of the determination of the "beam-broadened" component. Although Figure 2.2 suggested that models "N" and "LS" produced similar results, Figure 2.4(a) showed differences in the details, with the "LS" method showing higher percentages of negative values than model "N". In the following sections, we will consider each of these possibilities in turn. The first item for discussion will be the last one discussed, namely the accuracy of the determination of the "beam-broadened" variance.

2.2 Comparison between Different "Beam-broadening" Models

Equation (1.38) was developed by Nastrom (1997) as an analytical expression for calculation of the spectral variance due to a mean wind and a wind shear, as a function of various radar-related terms. The model made the following assumptions:

(i) The model is two dimensional, and assumes only an x-z vertical plane.

(ii) The polar diagram is assumed to have sharp edges at $\pm v$, where v is the one-way half-power width of the beam.

(iii) The polar diagram is assumed to have constant gain within the region between $-v$ and $+v$, and changes abruptly to zero gain further from the beam-centre.

(iv) All calculations are performed with the one-way beam only.

(v) The pulse is assumed to be a square function.

(vi) The returned power is calculated by assuming the pulse is centred at a fixed range R_0, and does not consider that the returned power is a convolution between the scattering function and the pulse.

(vii) No consideration is made for dependence of backscattered power on range within the pulse.

(viii) The receiver is assumed to have an infinite band-width.

(ix) It is assumed that the beam-width is unchanged as the beam moves to off-zenith angles.

Figure 2.5(a) shows the assumed situation. Radar scatter at a particular range is assumed to come from within the darkest shaded section, and from nowhere else. The distance across the dark area along the beam is the effective pulse length, and the distance perpendicular to the radial direction is proportional to the beam-width. The beam does not taper off with zenith angle in the way that a real radar beam does, and the pulse starts and stops abruptly. This is actually unrealistic, since even a square pulse will be smoothed by the receiver upon reception, unless the receiver has an infinite bandwidth. For help with future discussions, we have also added some key scales on the diagram; notice in particular the lengths $\Delta R \cos\alpha$ and ζ, which represent the vertical projection of the pulse, and the vertical distance from the lower point of the beam at L to the upper point at U. Both these scales are important in regard to wind shear, as will be seen in due course. Another somewhat important scale is the vertical projection of the distance from U to C, which is of the order of $\sqrt{\left[(2R_0 v)^2 + (\Delta R)^2\right]}$. However, this term will be covered by other terms involving ΔR and ζ, and so we consider ζ and ΔR as the main basic vertical length units.

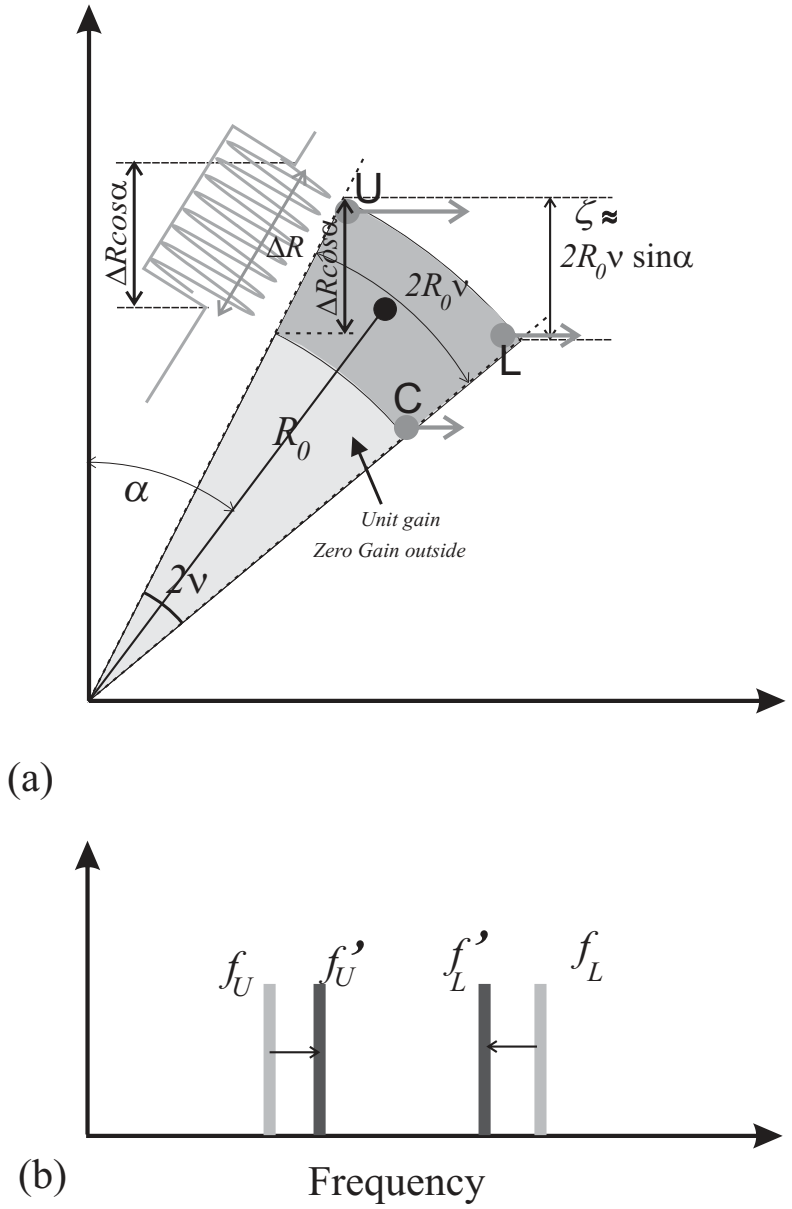

Figure 2.5: (a) Diagram of the polar diagram assumed for model "N" in the text. Despite of an oversimplification of the true polar diagram, it is useful for descriptive purposes. Note in particular the two critical scales ζ and $\Delta R \cos\alpha$. (b) Demonstration of beam and shear-broadening using two samples scattering points, U and L. See text for details.

As noted, many of the assumptions listed above are not valid for a real radar. The assumptions also result in unrealistic spectra; Figure 2.6 shows the spectrum produced for a mean wind and wind shear for the Nastrom model, and for a more realistic beam. The sharp corners on the spectrum produced under the above assumptions are especially noticeable and not realistic. The smoother spectrum was produced by the model discussed in regard to Equations (1.39) and (1.40) earlier.

However, by choosing such a simple model, it was possible for the author (Nastrom) to achieve an analytical expression for the broadening of the beam due to non-turbulent effects. The advantage is that it highlights the key terms that might be important in even a three-dimensional model, even if their proportional contributions might be in error. The simple diagram also helps visualize some of the effects. For example, Figure 2.5(b) highlights the cause of the broadening. The grey lines at f_{U} and f_L represent spectral lines produced by scatterers moving horizontally at the same speed at the points U and L in Figure 2.5(a). The different frequencies arise due to the different zenith angles of the two points. When scatterers from throughout the beam are considered, the spectrum fills in and has finite width. If the wind speed at U is increased, and at L is decreased, as shown in Figure (2.5a), then f_{U} moves to $f_{\mathrm{U'}}$ (due to its increased radial velocity) in Figure 2.5(b), and f_{L} moves to $f_{\mathrm{L'}}$, (due to its decreased radial velocity), and the overall spectrum will narrow. This illustrates the phenomenon of wind-shear spectral narrowing (e.g. Hocking, 1983; May et al, 1988; Nastrom et al., 1997).

Nastrom (1997) gives both an "exact" solution and an approximate one. Equation (1.38) was the "approximate" expression, but in view of the various assumptions which were made in deriving the "exact" expression, it has no greater claim to accuracy than the approximation. The approximation contains most of the pertinent terms needed to describe the spectral beam-broadening effect.

Given the various assumptions relating to this model, it should come as no surprise if the true contributions of the various terms were to differ from the model representations. An example is the first term, which involves division by 3, but all other calculations of this term by other authors involve division by 4ln2, as will be seen shortly.

However, in view of the key scales indicated in Figure 2.5, we will modify Equation (1.38) by using the expression $\zeta = 2vR_0 \sin\alpha$, as discussed in regard to that figure. We will also group the terms ΔR and $\cos\alpha$ where possible. We will also use the (very accurate) approximation that $(3 + \cos 4\alpha - 4\cos 2\alpha) = 8\alpha^4$ (easily verified by expanding the cosine terms as Taylor expansions to the third term), which we will

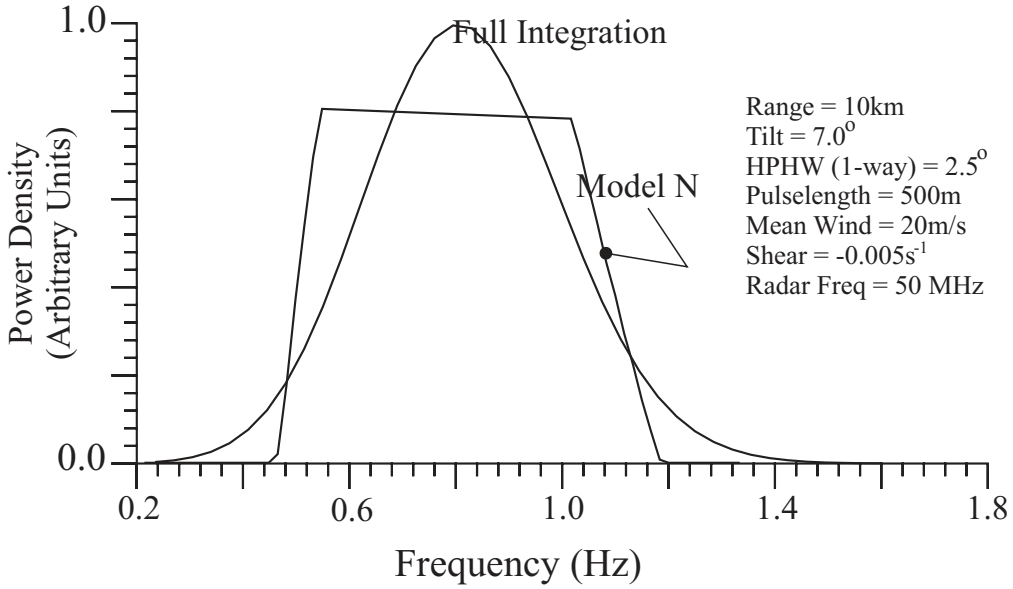

Figure 2.6: Spectra deduced using model N and a full integration, for identical wind, wind-shear and matching radar parameters.

write as $8\sin^4\alpha$. We also will use the fact that the first term inside the first set of brackets in the last part of the equation is negligible, viz. $\left(\frac{v^3}{3}\right)\cos 4\alpha \ll \sin^2\alpha\cos^2\alpha$. This can be seen by considering a relatively extreme example. If we assume a value of $v = 3°$, and $\alpha = 5°$ (which would normally be ill-advised, since the beam tilt is only just greater than the beam-width), then $\left(\frac{v^2}{3}\right)\cos^4\alpha = 8.59\times10^{-4}$, while $\sin^2\alpha\cos^2\alpha$ is 8.7 times bigger, or almost an order of magnitude larger. If α is 7°, the ratio is 18, and for larger tilts and narrower beams, even larger. Considering that this last additive term is already a small contributor, except for extreme pulse-lengths, then a sub-contributor which is an order of magnitude smaller than the $\sin^2\alpha\cos^2\alpha$ term can readily be ignored. In addition, we must also divide the whole equation through by $\cos\alpha$, since in a realistic situation the beam broadens inversely proportionally to $\cos^2\alpha$ as it tilts. Hence, adapting Equation (1.38), we now write:

$$\begin{aligned}\sigma^2 \;\approx\; & \frac{v^2}{3}u_0^2\cos\alpha - \frac{v}{3}\sin\alpha\left(u_0\frac{\partial u}{\partial z}\zeta\right) + \frac{2\sin^2\alpha}{24}\cos^p\alpha\left(\frac{\partial u}{\partial z}\zeta\right)^2 \\ & + \left(\sin^2\alpha\right)\cos^q\alpha\left(\frac{\partial u}{\partial z}\right)^2\frac{\left(\Delta R\cos\alpha\right)^2}{12}.\end{aligned} \tag{2.1}$$

Here, p and q are nominally each equal to -1. The terms each involve u_0, $\frac{du}{dz}$, ζ and ΔR, so in principle the expression for σ^2 should depend on the following terms:

$$\begin{aligned}&\text{(i) } u_0^2, \text{(ii) } u_0\left[du/dz\right]\zeta, \text{(iii) } u_0\left[du/dz\right]\left(\Delta R\cos\alpha\right)\\&\text{(iv) }\left[du/dz\right]^2\zeta, \text{(v) }\left[du/dz\right]^2\left(\Delta R\cos\alpha\right)^2, \text{(vi) }\left[du/dz\right]^2\zeta\left(\Delta R\cos\alpha\right).\end{aligned} \tag{2.2}$$

Our intent is to use these terms to develop a new expression for the beam-broadening term which more accurately matches the 3-D model described by Equations (1.39) and (1.40). We expect these terms to be the main terms even for a proper 3-D model. Term (i) of (2.2) appears in the first term of Equation (2.1), term (ii) appears in the second term of Equation (2.1), term (iv) appears in the third term of (2.1), and term (v) appears in the last term of (2.1). The terms (iii) and (vi) do not appear in the 2-D solution. It may not be surprising that the last term does not appear, since it involves a cross-term in the two largely independent length scales. However, we might expect term (iii) to play a role in a 3-D situation.

It is also expected that with a more realistic model, the relative contributions of the terms may change. Our intent is to develop an analytical expression for a three-dimensional model, so we will use the same terms as those in Equation (2.1), but allow each to have a multiplicative constant, with one exception. Term1 is given as $\left(\frac{v^2}{3}\right)u_0\cos\alpha$ but most derivations in three-dimensions produce a constant equal $4\ln 2$ in place of the constant 3. This was discussed by Nastrom (1997) and various references therein (Atlas, 1964; Sloss and Atlas, 1968; Atlas et al., 1969; Gossard et al., 1990). The same is true for the model of Hocking (1983, 1985), who showed that the beam-broadening term should be $f_B = 1.0\left(\frac{2}{\lambda}\right)u_0\theta_{1/2}$, where λ is the radar wavelength and $\theta_{1/2}$ is the two-way half-power half-width which equals $v/\sqrt{2}$. If we multiply through by $\lambda/2$ to convert to velocity instead of frequency, and divide through by $\sqrt{2\ln 2}$ to convert the half-power half-width to the standard deviation (valid for a Gaussian function), and then square, we obtain $\sigma^2 = u_0^2 v^2/\kappa$, where $\kappa = 4\ln 2$.

We will therefore write that the three-dimensional analytical expression for σ^2 is as follows:

$$\begin{aligned}\sigma^2 \;\approx\;& \frac{v^2}{\kappa}u_0^2\cos\alpha - a_0\frac{v}{\kappa}\sin\alpha\left(u_0\frac{\partial u}{\partial z}\zeta\right) + b_0\frac{2\sin^2\alpha}{8\kappa}\left(\cos^p\alpha\right)\left(\frac{\partial u}{\partial z}\zeta\right)^2\\&+c_0\left(\cos^s\alpha\sin^t\alpha\right)\left(u_0\xi\right) + d_0\left(\cos^2\alpha\sin^2\alpha\right)\left(\cos^q\alpha\right)\xi^2,\end{aligned} \tag{2.3}$$

where we have defined $\zeta = [du/dz]\,\Delta R/\sqrt{12}$ for consistency with Equation (2.1). The constants a_0, b_0, c_0, p, s, t and q need to be determined. Note the introduction of a new term involving $u_0\xi \propto u_0\,[du/dz]\,\Delta R$ which did not exist in Equations (1.38) and (2.1).

The full 3-D computer model defined by Equations (1.39) and (1.40) was then run for over 3000 combinations of pulse length, beam width, beam tilt, range, wind speed and wind shear. Pulses used were 200 m, 500 m, 800 m, and 1 km, and beam tilts were 7°, 10.9° and 15°. One-way beam widths used were 1.5°, 2.3°, 2.5°, 2.75°, and 3.0°. Ranges used were 5, 10, 15 and 20 km, and wind speeds were 40, 20, 10 and 5 m/s. Wind shears used were -0.01, -0.008, -0.005, -0.002, 0, 0,002, 0.005, 0.008 and 0.01 m/s. In addition, the model had the capability to assume that the scatterers occurred in discrete layers, rather than being homogeneously distributed throughout the atmosphere. The layer depth could be varied, but for our calculations we have used a fixed depth of 1 km, since this is comparable to the buoyancy scale of turbulence.

The polar diagram assumed took the following form. The power transmitted or received at zenith angle θ and azimuth ϕ was given by:

$$P(\theta,\phi) = A_0 \exp\left\{-\left(y_1^2 + y_2^2\right)/\theta_0^2\right\}, \tag{2.4}$$

where $y_1 = \sin\theta\sin\phi - \sin\alpha\sin\varphi_0$, $y_2 = \sin\theta\cos\phi - \sin\alpha\cos\varphi_0$ and θ_0 is the two-way 1/e half beam-width. This gives a Gaussian polar diagram peaking at (α, φ_0), and broadens proportionally to $\cos\alpha$ as the beam tilts from vertical (i.e. as α changes). (The polar diagram is the 2-D Fourier transform of the aperture function of the antenna field with phase adjustment, and the above expression effectively expresses it in terms of direction cosines, which incorporates a broadening of the beam as it tilts).

The result of the fitting gave the following values for the variables used: $a_0 = 0.945$, $b_0 = 1.50$, $c_0 = 0.03$, p=0, s=2, t=2 and q=0. Interestingly, the second terms in Equations (1.38) (or 2.1) and (2.3) actually agree to about 4%. The other terms show bigger relative differences. One modification was required to Equation (2.3), however. A new term involving $u_0\xi$ was introduced in equation (2.3), but extensive studies showed that the term produced better agreement with the model if the modulus of the quantity was used. The final model formula was:

$$\sigma^2 \approx \frac{v^2}{\kappa}u_0^2\cos\alpha - a_0\frac{v}{\kappa}\sin\alpha\left(u_0\frac{\partial u}{\partial z}\zeta\right) + b_0\frac{2\sin^2\alpha}{8\kappa}\left(\frac{\partial u}{\partial z}\zeta\right)^2 \\ +c_0\left(\cos^s\alpha\sin^t\alpha\right)|u_0\xi| + d_0\left(\cos^2\alpha\sin^2\alpha\right)\xi^2, \tag{2.5}$$

This equation will be referred to as model "C" (for "current") in this text, while Equations (1.38) and (2.1) will be referred to as model "N". The full integral (Equation (1.39)), which is used as a reference, will be referred to as the "full model". If the difference between the variance for the model and the full model is found (absolute value only), and is divided by the variance from the full model in each case, the mean displacement is found to be 12.45 % for Model N. If the first term of Equation (1.38) is adjusted to use a division by 4ln2 instead of 3, the error in model N reduces to 6.9 %. For model C, the difference reduces to 5.7 %.

Further improvement to model C may be achieved by some modest adjustments at critical points. The correction term involves incorporation of a set of Gaussian and hyperbolic tangent corrections, and will be referred to as model "Cc" for "Current-corrected". With model Cc (the numerical code is given in Appendix C), the mean error reduces to 4.1 %, relative to a full model.

Figure 2.7(a) shows a histogram of the differences in the models N, C and Cc compared to the full model. Note that model N is shifted to the left. This offset can be removed by replacing the "3" in the first term of (1.38) by 4ln2. However, an additional point of note is the bulge in values at the point X. This bulge also appears in models C and Cc if the new term involving $|u_0\xi|$ is not included. Without this term, the percentage error for model C increases from 5.7% to 7.3%. The bulge is mainly associated with large pulse lengths and large wind-shears, and incorporation of the term involving $|u_0\xi|$ is necessary to obtain optimum agreement.

The above discussions have concentrated on use of percentage errors, but in some ways the absolute errors are more important. The mean displacement of Model N is -0.06 m^2/s^2. By contrast, over 90% of all of the values for model Cc are within ± 0.05 m^2/s^2 of the corresponding variance for the numerical integration. The question now arises as to the importance of an offset of 0.05 m^2/s^2. Since $\varepsilon = 1.7\left(\sigma_t^2/T_B\right)$, if we take a Brunt-Vaisala period of 600 s, then an offset in ε of $\delta\varepsilon$ can be written as $\delta\varepsilon = 0.0028\delta\left(\sigma^2\right)$, so an error $\delta\left(\sigma^2\right) = 0.05$ corresponds to an error in ε of 1.4×10^{-4} W/kg.

We have also adopted one extra algorithm, described by Figure 2.8, which parametrizes the full model in a different way. Previous analyses with the full model have been used

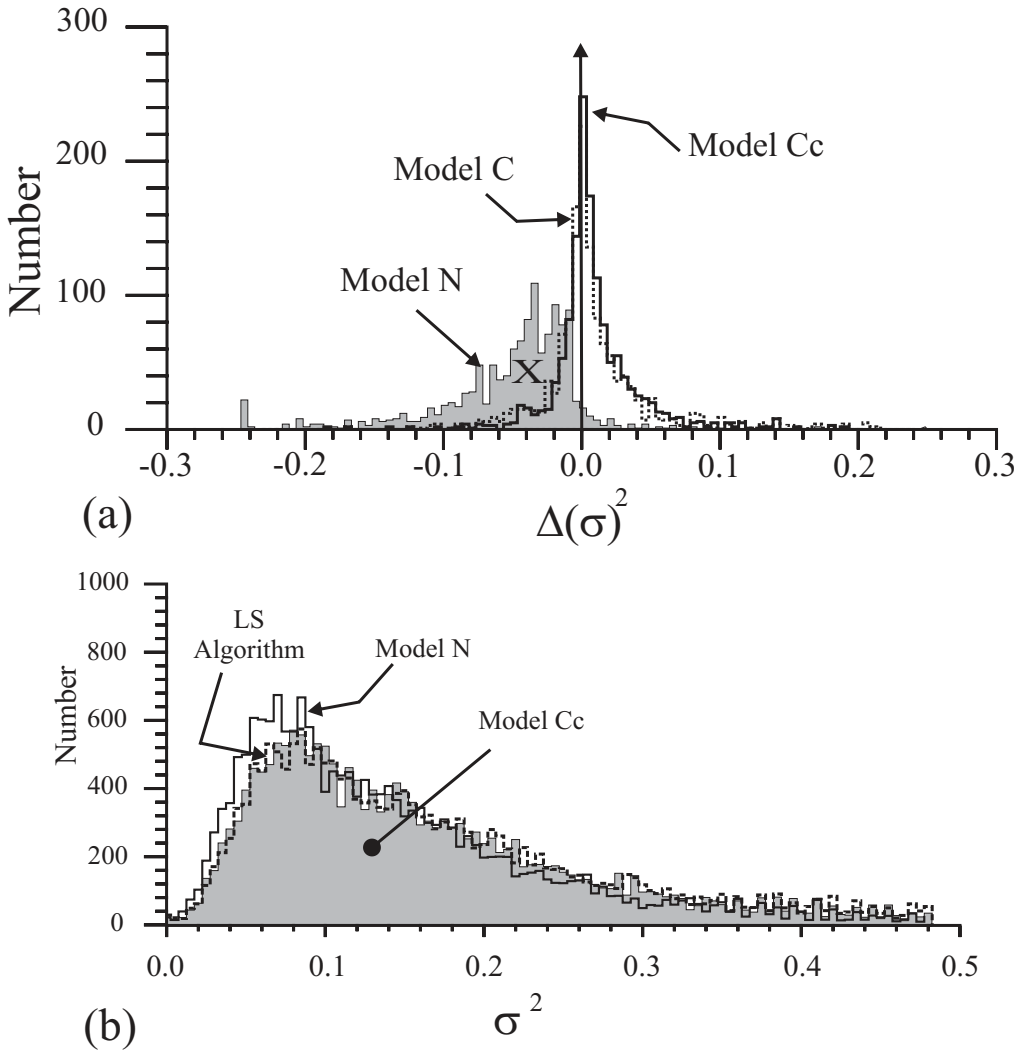

Figure 2.7: (a) Histograms of the differences in the variance expected due to geometric effects alone ("beam-broadening") for various analytic models, relative to a three-dimensional numerical calculation. A selection of beam tilts, beam-widths, pulse-lengths, ranges and wind speeds have been chosen, as described in the text. Model N refers to Nastrom (1997), and model C refers to the new model developed in this paper. Model Cc refers to model C with additional adjustments. The mean displacement of model N is -0.06 m^2/s^2, while for models C and Cc it is -0.001 and 0.004 m^2/s^2 respectively. (b) Beam-broadened spectral variances deduced with the three models for realistic winds, taken from the Harrow radar for July 1-31, 2007. Note that the shaded areas in figures (a) and (b) are not for the same model — the shading is chosen simply to improve the visual contrast between the models.

to produce model spectra, expressed as Gaussians, for thin layers of the atmosphere. The widths, offsets and spectral widths have been expressed analytically as functions of range, pulse-width, offset of the layer from the center of the pulse, beam-width, zenith tilt and so forth, and stored in a subroutine. The final spectrum is determined by evaluating the Gaussian spectra for each layer using these parameters, and summing the resultant spectra frequency by frequency. This method will be called the "LS" method (for "Layer-Summation" method). The advantage of this method is that it allows accurate computation and display of the actual spectra, whereas the methods N, C and Cc only produce a number for σ^2. Spectra can be asymmetric in the case of strong shears, and it is often useful to see the shapes of the spectra, which LS can produce. Furthermore, the calculation can deal with any form of wind profile, including ones with more complex profiles than a simple wind shear. It can deal with situations in which the wind profile shows curvature (none, zero, second, and higher derivatives), and is better suited to cases for which the wind profile shows complex structure (such as a mixture of rotational and linear wind shears).

Figure 2.7(b) shows the distribution of the theoretical variance σ^2 (before inclusion of turbulence) for all of the wind profiles recorded with the Harrow radar in July 2007. The previous models dealt only with wind shears parallel to the beam, but in the real situation, shears may exist perpendicular to the beam as well. We have dealt with these in the same way that Nastrom and Tsuda (2001) did. We have determined the value for σ^2 using the wind components parallel to the beam, and then for the case perpendicular to the beam. For the perpendicular case, we ignore any transverse wind shears and use only the first term in Equations (1.38), (2.1) or (2.5). We have then added the two terms.

Model LS is included in this case, but not model C, since addition of model C simply makes the graph harder to read. It produces a histogram similar to models LS and Cc. The most noticeable difference is that model N produces a larger number of small values of σ^2, around 0.06 to 0.08 m^2/s^2. Hence in the event of turbulence of the order of 10^{-4} W/kg, model N may produce errors of the order of a factor of 2 or so. Hocking and Mu (1997), show that such values are relatively common. On the other hand, turbulence is a hard parameter to measure, and an error of a factor of 2 might be considered relatively small in the overall picture. The occurrence of smaller theoretical values of σ^2 will also reduce the number of negative occurrences of ε, as seen in Figure 2.4(a). This does not make it a better model, however.

Despite the potential inherent advantages of the LS model, it does not seem to provide any real advantage over model Cc in a practical situation, and we will use

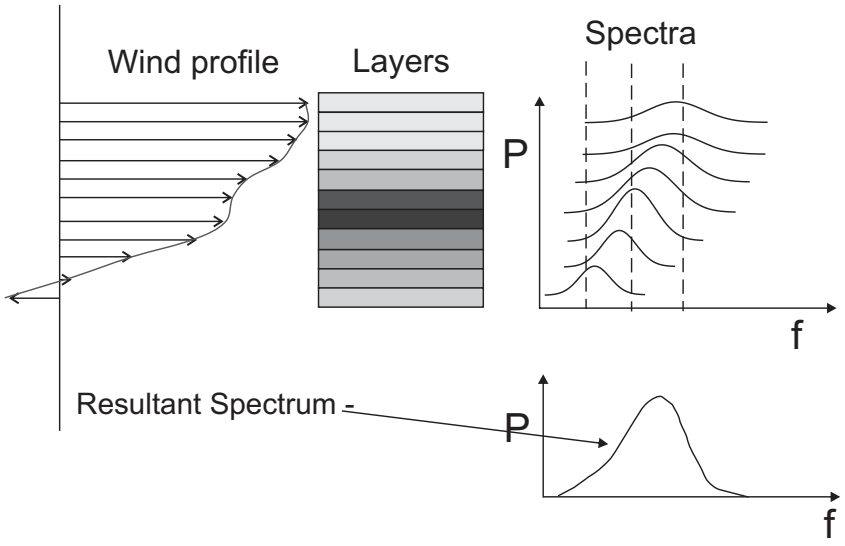

Figure 2.8: Illustration of the integration scheme proposed by Hocking (2003). Only a one-dimensional profile is shown, for simplicity. Spectra are calculated in small, thin sublayers. Backscattered powers from each sub-layer are shown as a grey-scale. The spectra, weighted according to backscattered power for each sub-layer, are summed to produce a final spectrum.

the two models interchangeably throughout the rest of this text.

Figure 2.9 shows the results of applying the various models to real data, again using data from Harrow for July 2007. All data in the height range of 1.5 to 10 km have been used. Here, the distributions of measured turbulence values are shown for model Cc and model N, and for 3 different azimuthal beam directions. Results are all quite similar, and the only noticeable difference is a slight tendency for model N to be shifted to more positive values, as would be expected from the fact that Figure 2.7(b) shows an excess of smaller theoretical non-turbulent spectral widths. There is no noticeable difference between the beams, and the fourth beam shows similar values (not plotted in order to avoid congestion).

Overall, the agreement between the various models can be considered to be quite good. It is interesting (and even curious) that model "N" shows good agreement when the one-way 2-D polar diagram is used to represent the two-way 3-D polar diagram. Despite the various approximations of the model, though, the agreement of model N with the full model is generally fair, although it is prone to slightly underestimate the true non-turbulent width. This may be of some consequence for cases where turbulence is weak to moderate, but is of little consequence when turbulence is strong. We do recommend use of the more exact expressions for σ^2, but conclude that the

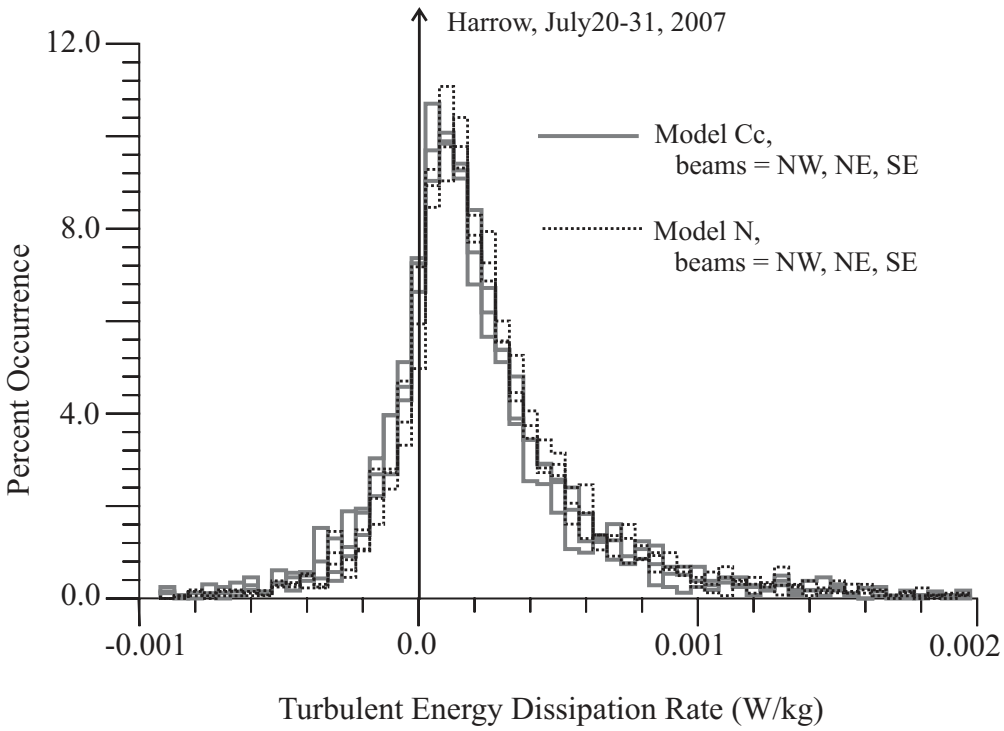

Figure 2.9: Histograms of turbulent energy dissipation rates produced for the month of July, 2007, for the Harrow radar, using models Cc and N for the instrumental beam-broadened calculations. The graphs cover all heights from 1-10 km.

choice of beam-broadening model used is only a modest contributor to errors in the percentage of negative turbulence estimates.

2.3 Anisotropic Turbulence

In the spectral width method presented to date, it has been assumed that turbulence is isotropic. When turbulence is anisotropic, the horizontal wind speed is underestimated by the radar by a factor, R_1 (Hocking, 1989), where

$$R_1 = \left[1 + \frac{\theta_0^2}{\theta_s^2}\right]. \tag{2.6}$$

Here θ_0 is the 1/e half-width of the two-way radar beam and θ_s is the anisotropy angular factor of the backscatterers (e.g. as defined in Hocking 1987, or Hocking, 1988, Appendix A). The half-power half-width of the radar beam also needs to be corrected by the factor, where:

$$R_2 = \left[1 + \frac{\theta_0^2}{\theta_s^2}\right]^{-1/2}. \tag{2.7}$$

(also shown in Hocking, 1988, Appendix A).

The parameter θ_s can be determined by comparing the powers on the vertical and off-vertical beams, using the relation (Hooper and Thomas, 1995):

$$\theta_s = \arcsin\sqrt{\frac{\sin^2\theta_2 - \sin^2\theta_1}{\ln\left[P(\theta_1)/P(\theta_2)\right]} - \sin^2\theta_0} \tag{2.8}$$

where $P(\theta_1)$ and $P(\theta_2)$ are the received backscatter power for two zenith angles of θ_1 and θ_2, and θ_0 is two way half-power half-width of radar beam. Values for θ_s have been measured many times in the atmosphere, and generally lie between 3° and 15° (Hocking et al., 1986). We also measure this parameter routinely with our radars e.g. see Hocking and Hocking (2007).

It is important to determine the effects of θ_s on our estimates of turbulence. Two possible scenarios exist in a realistic situation. First, it is possible that the user does not correct for the wind speed effect given by Equation (2.6). This is the most common case. Second, it is possible that the mean wind is corrected for the wind speed. In the first case, the theoretical beam-broadened width will be too narrow by an amount given by R_1R_2, where the first term arises because the mean wind used is too small, and the second arises because the aspect sensitivity term has been

ignored. The net result is that the theoretically determined spectral width will be too narrow by an amount $\sqrt{(1+\theta_0^2/\theta_s^2)}$ and σ^2 will be too small by factor of $(1+\theta_0^2/\theta_s^2)$. Hence determination of ε will result in values that are too large, rather than values that are too small, so these cannot contribute to the negative values for ε. If, on the other hand, the mean wind has already been corrected for the anisotropy, then the only missing term in the determination of the theoretical spectral width is the anisotropy factor, so in this case σ^2 will be too wide by an amount R_2^{-2}, or by a fraction $[1+(v^2/\theta_s^2 2\ln 2)]$, since $\theta_0 = \Theta_{1/2}/\sqrt{\ln 2}$, and the two-way half-power half-width is equal to $v/\sqrt{2}$. This will result in an increase in negative ε. For example, if $\theta_s = 5°$, and $v = 2.5°$, the correction is 18%. Although values of θ_s less than 5° occur, they generally dominate the vertical beam, and not the off-vertical beams. Hence this may be considered as an upper limit on the correction term for most radars. This correction is very similar to the percentage difference between model N and the full numerical model discussed in Figures 2.7(a) and 2.7(b), which was 12.5%. Hence in such a situation, the effect of anisotropy should be at about the same level of that shown in Figure 2.7(b). This would be a worst-case scenario, and the effect rapidly diminishes for narrower beams.

In our case, we have not corrected for the mean wind, so that aspect sensitivity should actually increase ε, rather than producing negative values. This should therefore not be a contributor to our observed negative values.

2.4 The Primary Error Terms

The possible sources of error discussed to date have been only modest contributors. We now turn to the issues of wind variability and spectral fitting accuracy, as they turn out to be the most important terms.

2.4.1 Effect of Variability of the "Mean Wind"

Of the selection of reasons discussed earlier, we are now left with (i) variability of the mean wind and (ii) errors in estimates of the experimental spectral width. Both are expected to be important in a qualitative sense, but it is necessary to quantify their impact.

In Figure 2.4, the percentages of negative values were presented in various forms, and there was strong evidence that the percentage was a function primarily of the mean wind (figure 2.4(b)). In Figure 2.9, we showed the distribution of values for all

heights and all wind speeds. In Figure 2.10, we show histograms of the distributions of values for 2 different height regions (1-5 and 5-10 km), two different radars (Harrow and Walsingham) and for 4 different bands of mean wind speeds (5-10 m/s, 10-15 m/s, 15-20 m/s and 20-25 m/s). The broader nature of the distributions for increased wind speeds is quite apparent. The standard deviations of each of the distributions are indicated on the figures.

In order to help quantify the effect, Figure 2.11 shows the standard deviations of the hourly wind data. The variance in the north-south components, and the east-west components, were each calculated separately for each hour of the month of July, 2007, for the Harrow radar, and then the two components were added for each hour. The square root was then taken, and plotted against the wind speed. The process was performed for different height bins, but the RMS values did not vary substantially with height, so we have lumped all heights together and produced Figure 2.11(a). There is a large cluster of points which is clearly seen, plus some apparent outliers. We apply substantial quality control to our data, using a Weber-Wuertz-type algorithm at the minute-by-minute scale, to reject outliers at the earliest stages of analysis (Weber and Wuertz, 1991). The algorithm compares the observed value, V with the median of surrounding observations, V_m. If the difference (V-V_m) exceeds the critical value, V_c, then V is an outlier. The critical value in this algorithm is given by (Lambert and Taylor, 1998):

$$\begin{aligned} V_c &= \max(V_1, V_2) \\ V_1 &= 0.2 \mid V + V_m \mid \\ V_2 &= a.\left(Ah^2 + Bh + C\right), \end{aligned} \tag{2.9}$$

where a, A, B, C are constants and h is the height at which the measurement is done.

In addition, at least 8 points were required per hour before a data point was plotted on this graph. So these apparent outliers are also real data, and not artifacts, and arise due to the passage of frontal systems and other events that produce rapid changes in the large-scale winds, giving rise to large RMS fluctuations. The data have also been binned according to the mean wind, and the medians and 68th percentile determined for bins of 5-10, 10-15, 15-20, 20-25 and 25-30 m/s are shown in Figure (2.11). These are plotted as dark filled circles and squares (respectively) on the graphs. An approximate line has been drawn through the medians. Figure 2.11(b) shows the same type of display for the Walsingham data, but for 5-10 km altitude.

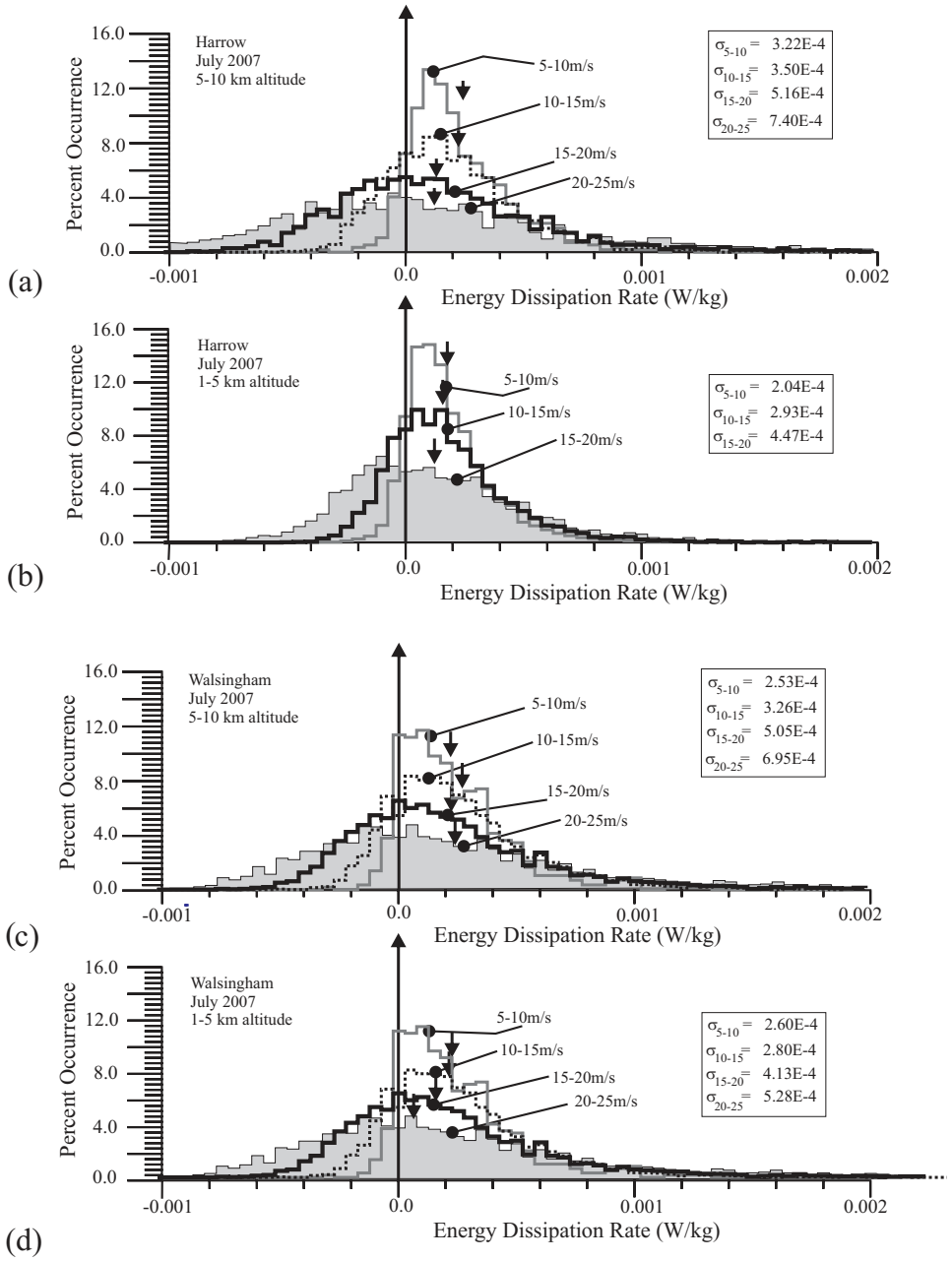

Figure 2.10: Histograms of the distributions of the turbulent energy dissipation rates for the Harrow and Walsingham radars for July, 2007. The histograms are separately produced within each set of graphs for wind-speed bins of 5-10, 10-15, 15-20 and 20-25 m/s. Figures (a) and (b) show distributions for the Harrow radar for 1-5 and 5-10 km altitude respectively, while (c) and (d) show the same for the Walsingham radar. Standard deviations for each distribution are shown in the boxes to the right. Mean values are indicated by the vertical arrows, and numerical values for the means appear in Tables 2.1 and 2.2.

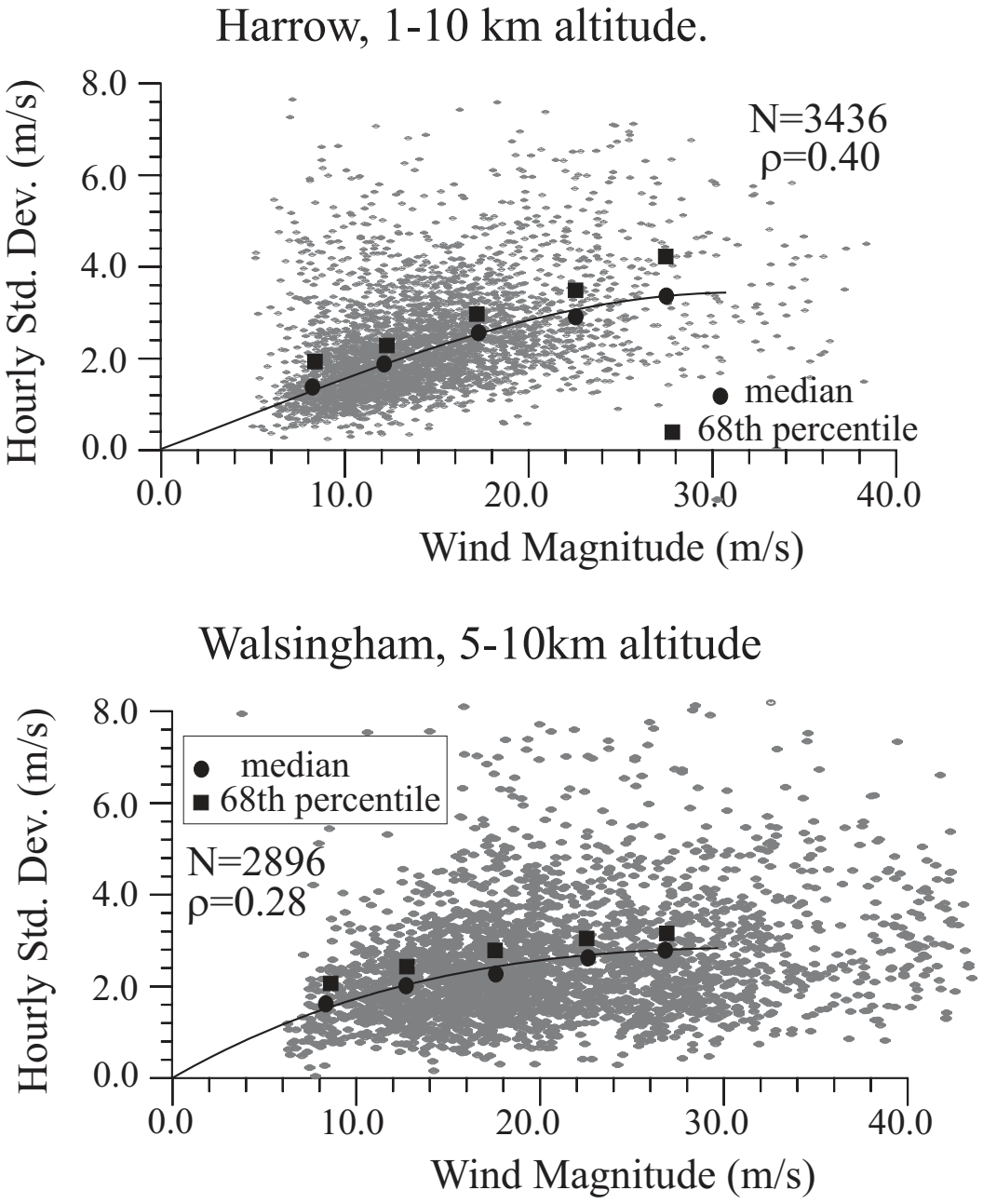

Figure 2.11: Hourly standard deviations of wind fluctuations plotted as a function of wind speed for the (a) Harrow and (b) Walsingham radars. Median values have been calculated in 5 m/s-wide wind-speed bins (5-10, 10-15, 15-20, 20-25, 25-30 m/s), and plotted as solid circles. The solid squares represent the 68th percentiles for the same bins. Total number of points used, and correlation coefficients, are shown as N and ρ. Both data sets are for July 2007, and for the heights indicated.

While the hourly standard deviations do increase with increasing mean wind speed, the increase is only modest, especially above 20 m/s. In order to further interpret the data, we need to develop a more complete theory about the errors, which we do in the next section.

2.4.2 Error due to variability of large-scale wind speed

The main term in the equation for σ^2 is the first term in Equation (2.5), so for purposes of error calculations we will concentrate on this term. Then we use

$$\sigma^2 = (4\ln 2)^{-1}\,\theta_{1/2(1)}^2 u^2, \tag{2.10}$$

$$\delta(\sigma^2) = (4\ln 2)^{-1}\,\theta_{1/2(1)}^2 2u\delta u, \tag{2.11}$$

where $\delta(\sigma^2)$ is the variation in σ^2 (the beam-broadened contribution to the variance), which we will consider here to be the standard deviation of σ^2. Here, u is the large scale wind speed, and $\theta_{1/2(1)}$ is the one-way half-power half-width of the polar diagram. Since $\sigma_t^2 = \sigma_e^2 - \sigma^2$, and $\varepsilon = 1.7(\sigma_t^2/T_B)$, we may multiply through by $1.7/T_B$ and take errors of each term, square and add to give $(\delta\varepsilon)^2 = (\delta\varepsilon_2)^2 + (\delta\varepsilon_1)^2$, where $\delta\varepsilon_2$ is the error in the turbulence strength associated with estimation of the experimental spectral width, and $\delta\varepsilon_1$ is the error associated with the beam-broadened term, as discussed above, therefore:

$$\delta\varepsilon_1 = 1.7\,(4\ln 2)^{-1}\,T_B^{-1}\theta_{1/2(1)}^2 2u\delta u. \tag{2.12}$$

We will call this the first error term, since we have discussed it first. For a half-power one-way half-width of 2.75°, and assuming a Brunt-Vaisala period (T_B) of 10 mins., as for the Harrow radar, gives $\delta\varepsilon_1 = 4.71\times10^{-6}u\delta u$. For Walsingham, $\delta\varepsilon_1 = 3.29\times10^{-6}u\delta u$. We will discuss application of this formula shortly, but first we will develop an expression for the error associated with determination of the experimental spectral width, denoted as $\delta\varepsilon_2$ above.

2.4.3 Errors in estimation of spectral width

An alternative reason for errors may relate to the accuracy with which the experimental spectral width can be determined. There are various reasons why this width may be in error. Noise naturally contributes, and its effect is worse if the "width" of the spectrum is determined by using a weighted integral for the variance. A superior

Height (km)	Speed (m/s)	δu (m/s)	$\delta\varepsilon_1$ $\times 10^{-4}$ $(\eta = 1)$	$\delta\varepsilon_2$ $\times 10^{-4}$ $(\eta = 1)$	$\delta\varepsilon_{total}$ $\times 10^{-4}$ $(\eta = 1)$	$\delta\varepsilon_{experiment}$ $\times 10^{-4}$	$\Delta\varepsilon$ $\times 10^{-4}$	$\overline{\varepsilon}$ $\times 10^{-4}$
1-5	5-10	1.92	0.67	1.3	1.46	2.03	1.41	1.9
	10-15	2.25	1.32	2.1	2.48	2.93	1.55	1.8
	15-20	2.81	2.35	3.0	3.81	4.47	2.34	1.5
5-10	5-10	1.92	0.67	1.3	1.46	3.22	2.87	2.4
	10-15	2.25	1.32	2.1	2.48	3.50	2.47	2.1
	15-20	2.86	2.35	3.0	3.81	5.16	3.48	1.6
	20-25	3.50	3.7	3.8	5.3	7.40	5.16	1.6

Table 2.1: Table of various parameters associated with the mean and errors involved with calculation of the strength of turbulence for the Harrow radar. The term δu refers to the value of the 68th percentile of the RMS fluctuations in the total mean wind (see Figure 2.11). See the text for the meaning of the terms $\delta\varepsilon_1$ and $\delta\varepsilon_2$. $\delta\varepsilon_{total}$ represents the square-root of the sum of the squares of terms $\delta\varepsilon_1$ and $\delta\varepsilon_2$. $\delta\varepsilon_{experiment}$ was taken from Figure 2.10, using the standard deviations provided there. $\Delta\varepsilon$ is calculated as $\sqrt{(\delta\varepsilon_{experiment})^2 - (\delta\varepsilon_{total})^2}$. The final column shows the mean values, also taken from Figure 2.10.

method is spectral fitting, as discussed earlier. Unfortunately, if the spectral width is over-estimated (as in the case of using weighted spectral moments), the percentage of negative estimates of will be reduced, giving the misleading appearance of improved data.

In the case of no noise, the width is still limited by the sampling rate of the data. The spectral resolution will be proportional to the frequency resolution, which will be proportional to the inverse of the data length.

For convenience, we will write that the error in the determination of the experimental value of σ_e, determined by whatever means, is proportional to $1/\tau$, where τ is the data-length of the sample. We will begin the derivation in terms of the measured spectral half-power half-width f_h, which has units of Hz, making it compatible with $1/\tau$. The quantity σ_e is of course related to f_h by $\sigma_e = (\lambda/2)f_h/\sqrt{2\ln 2}$, where λ is the radar wavelength. We will let the error in f_h, δf_h, be written as η/τ. In the best case, η will be of the order of unity, but it may be several times higher, especially if σ_e is found by weighted moments, or if noise levels are high.

The measured spectral half-power half-width is therefore $f_h \pm \delta f_h$, but the quantity that is needed for calculation of ε is f_h^2, and the act of squaring increases the error for large values of f_h (corresponding to large wind speeds) substantially, since $\delta(f_h)^2 = 2f_h\delta f_h = 2f_h\eta/\tau$. Using $\sigma_e = (\lambda/2)\, f_h/\sqrt{2\ln 2}$ then gives $\delta(\sigma_e^2) = (\lambda/2)^2\, 2f_h\eta/(\tau 2\ln 2)$, or

Height km	Speed (m/s)	δu (m/s)	$\delta\varepsilon_1$ $\times 10^{-4}$ $(\eta = 1)$	$\delta\varepsilon_2$ $\times 10^{-4}$ $(\eta = 1)$	$\delta\varepsilon_{total}$ $\times 10^{-4}$ $(\eta = 1)$	$\delta\varepsilon_{experiment}$ $\times 10^{-4}$	$\Delta\varepsilon$ $\times 10^{-4}$	$\overline{\varepsilon}$ $\times 10^{-4}$
1-5	5-10	2.09	0.52	0.98	1.11	2.60	2.35	2.3
	10-15	2.21	0.91	1.63	1.87	2.80	2.08	2.1
	15-20	2.38	1.37	2.28	2.66	4.13	3.14	1.7
	20-25	2.79	2.07	2.93	3.59	5.28	3.87	0.67
5-10	5-10	1.99	0.48	0.98	1.09	2.53	2.28	2.4
	10-15	2.38	0.98	1.63	1.90	3.26	2.65	2.6
	15-20	2.72	1.56	2.28	2.76	5.05	4.23	2.4
	20-25	3.00	2.22	2.93	3.67	6.95	5.90	2.5

Table 2.2: Table of various parameters associated with the mean and errors involved with calculation of the strength of turbulence for the Walsingham radar. The term δu refers to the value of the 68th percentile of the RMS fluctuations in the total mean wind (see Figure 2.11). See the text for the meaning of the terms $\delta\varepsilon_1$ and $\delta\varepsilon_2$. $\delta\varepsilon_{total}$ represents the square-root of the sum of the squares of terms $\delta\varepsilon_1$ and $\delta\varepsilon_2$. $\delta\varepsilon_{experiment}$ was taken from Figure 2.10, using the standard deviations provided there. $\Delta\varepsilon$ is calculated as $\sqrt{(\delta\varepsilon_{experiment})^2 - (\delta\varepsilon_{total})^2}$. The final column shows the mean values, also taken from figure 2.10.

$$\delta(\sigma_e^2) = \lambda\sigma_e\eta/\tau\sqrt{2\ln 2}. \tag{2.13}$$

At this stage σ_e is the "true" experimental signal standard deviation, but since this will be similar to the beam-broadened value, we may replace it with $\sigma = \sqrt{(4\ln 2)^{-1}}\theta_{1/2(1)}u$. We will also convert to an error in ε by multiplying by $1.7/T_B$ just as we did in equation (18), to give:

$$\delta\varepsilon_2 = \frac{1.7}{\left(2\sqrt{2}\right)\ln 2}\left[\frac{\theta_{1/2(1)}\lambda\eta u}{\tau T_B}\right]. \tag{2.14}$$

For the Harrow radar, with $\lambda = 300/40.68 = 7.37$m , $\theta_{1/2(1)}= 2.75°$, and $\tau = 30$s, this gives

$$\delta\varepsilon_2 = 1.704 \times 10^{-5}\eta u. \tag{2.15}$$

For Walsingham the constant is 1.303×10^{-5}.

2.4.4 Specific applications of the error formulae

Values for the error terms discussed above, compared to experimental errors, are shown in Tables 2.1 and 2.2, where we have assumed η=1. In the Harrow case, we

have assumed identical values for measured variances for 1-5 km and 5-10 km, since the results at the two different heights were very similar. In Table 2.2, we have treated the heights independently, but as can be seen the data sets gave very similar variances and we could have treated these as identical too.

Both error terms are important, and comparable, although the digitization error tends to dominate. However, this assumes a data-length of 30 s. If a radar uses a data length of 10 s (as is quite common), the second term increase 3 fold, vastly degrading the radar performance for measurement of turbulence strengths. If η is greater than 1, as is likely (and especially likely if weighted moments are used), the errors ($\delta\varepsilon_2$) increase even more.

In Tables 2.1 and 2.2, $\Delta\varepsilon$ is calculated as $\sqrt{(\delta\varepsilon_{experiment})^2 - (\delta\varepsilon_{total})^2}$. If it is true that $\eta = 1$, then $\Delta\varepsilon$ represents the true natural variability of the background turbulence strength. This is likely an upper limit. Alternatively, we could assume η is an error, in which case the values $\delta\varepsilon_{experiment}$ and $\delta\varepsilon_{(2)}$ can be used to place limits on η. Given that the ratio $\delta\varepsilon_{experiment}/\delta\varepsilon_{(2)}$ lies between typically 1.5 and 3, it suggests η is less than 1.7. The truth is somewhere between 1 and this value, with the relative contributions to the experimental error being distributed between a contribution for $\delta\varepsilon_{(2)}$ and a true natural variability. Variations in T_B can also have modest contributions to the error.

The mean values of the energy dissipation rates are shown as the last columns of the tables. Typical values are of the order of 1-3$\times 10^{-4}$ W/kg. These values are quite consistent with extensive in-situ data presented by Lee et al. (1988) and summarized in Hocking and Mu, (1997). It needs to be highlighted that these are average background values — turbulence is characterized by rarer but intense bursts of energy (as shown in Figure 2.2), which makes the distributions asymmetric, and radars are well suited for studying such events. However, this does not negate our estimates of the background average levels when such bursts are not present.

Chapter 3

Climatology of the Brunt-Vaisala Frequency

The Brunt-Vaisala frequency is the frequency at which a vertically displaced air parcel will tend to oscillate about its initial position. This requires that the atmosphere is statically stable (or stably stratified). The vertically displaced particle experiences a vertical acceleration which is given by the following equation (Holton, 1992):

$$\frac{d^2}{dt^2}(\delta z) = g\frac{\delta \ln \theta_p}{\delta z}(\delta z), \tag{3.1}$$

where δz is the displacement, g the gravity acceleration, and θ_p the potential temperature (see Equation (1.7)). Equation (3.1) is the equation of harmonic motion. Therefore, the frequency of the motion is given by (see Appendix D):

$$\omega_B^2 = g\frac{d \ln \theta_p}{dz}, \tag{3.2}$$

where ω_B is the Brunt-Vaisala frequency.

The Brunt-Vaisala frequency is a measure of atmospheric stability. If $\omega_B^2 > 0$, the atmosphere is stable, since the acceleration is toward the equilibrium position. If $\omega_B^2 = 0$, the atmosphere is neutral and if $\omega_B^2 < 0$, the atmosphere is unstable, which means that the air parcel displacement will increase exponentially with height (Holton, 1992). The Brunt-Vaisala frequency is a key parameter in estimating the turbulent energy dissipation rate, ε (see equation (1.32)). For average tropospheric conditions, $\omega_B \sim 0.01$ s^{-1} and it changes to about 0.02 s^{-1} in the stratosphere (e.g. Fairall et al., 1991; Kantha and Hocking, 2011). We have used the typical value of ω_B (0.01 s^{-1}) in this work. However, in this chapter we will look at the variations of ω_B during different conditions. Note that we will mostly focus on measurements in

the troposphere, since it is the primary region of interest.

3.1 Sample Measurements of the Brunt-Vaisala Frequency

Using Equation (3.2), ω_B was estimated from radiosonde data which was measured at the Walsingham and Harrow radar sites. The results are shown in Figures 3.1 and 3.2. Figure 3.1(a) is the vertical profile of ω_B^2 with the resolution of 40 m at Walsingham for March 2007. Note that the transition from troposphere to stratosphere is obvious as ω_B^2 increases from the typical value of 10^{-4} Hz^2 below 10 km to approximately 4×10^{-4} Hz^2 above 10 km. The negative values of ω_B^2 are indicative of instability in the atmosphere. It can be seen that most of the time, the atmosphere is stable ($\omega_B^2 > 0$). This is because any unstable regions that develop are quickly stabilized by convective overturning (Holton, 1992). The vertical profile of temperature in Figure 3.1(b) shows that temperature is increasing with height from the surface to 2 km and decreasing from 2 to about 11 km at the rate (lapse rate) of approximately 6° C/km. In the atmosphere, if a parcel of air warms (expands) or cools (compresses), with no interchange of heat with its environment, the process is called adiabatic. The rate of adiabatic cooling or warming is called adiabatic dry lapse rate, which is about 10° C/km for unsaturated air (e.g. Ahrens, 2000). Therefore, because the lapse rate at Walsingham is smaller than dry adiabatic lapse rate, we can conclude that the troposphere is statically stable.

Figure 3.2 shows the vertical profiles of ω_B^2 and temperature at Harrow in June 2007. The results are similar to the measurement results at Walsingham (Figure 3.1). However, the percent of negative ω_B^2 is greater at Harrow. This may be due to the fact that during summer (June), instability can increase due to convection. Another possible reason could be the higher resolution of measurements (15 m) in this case.

3.2 Analysis of the Brunt-Vaisala Frequency in the Troposphere

In this section, we will concentrate on the analysis of ω_B^2 in the troposphere. Figure 3.3 shows the distribution and vertical profile of ω_B^2 in the troposphere. The data were measured at Walsingham on March 3, 2007 and have a height resolution of 40 m. Figure 3.3(a) shows the distribution of ω_B^2. Each bin has a width of 10^{-4} with centers

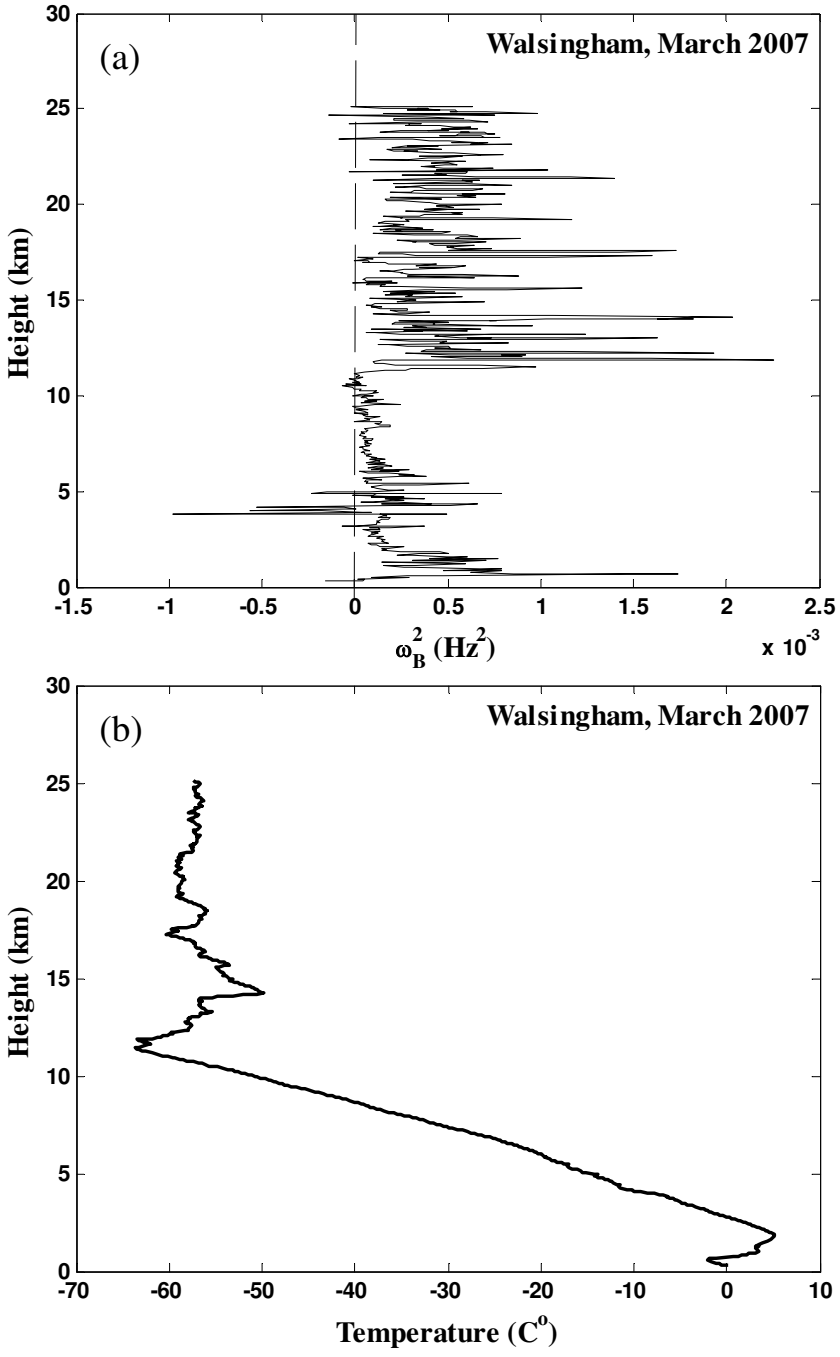

Figure 3.1: The vertical profiles of (a) the Brunt-Vaisala frequency squared, ω_B^2 and (b) temperature measured on March 2, 2007 at Walsingham. The resolution is 40 m.

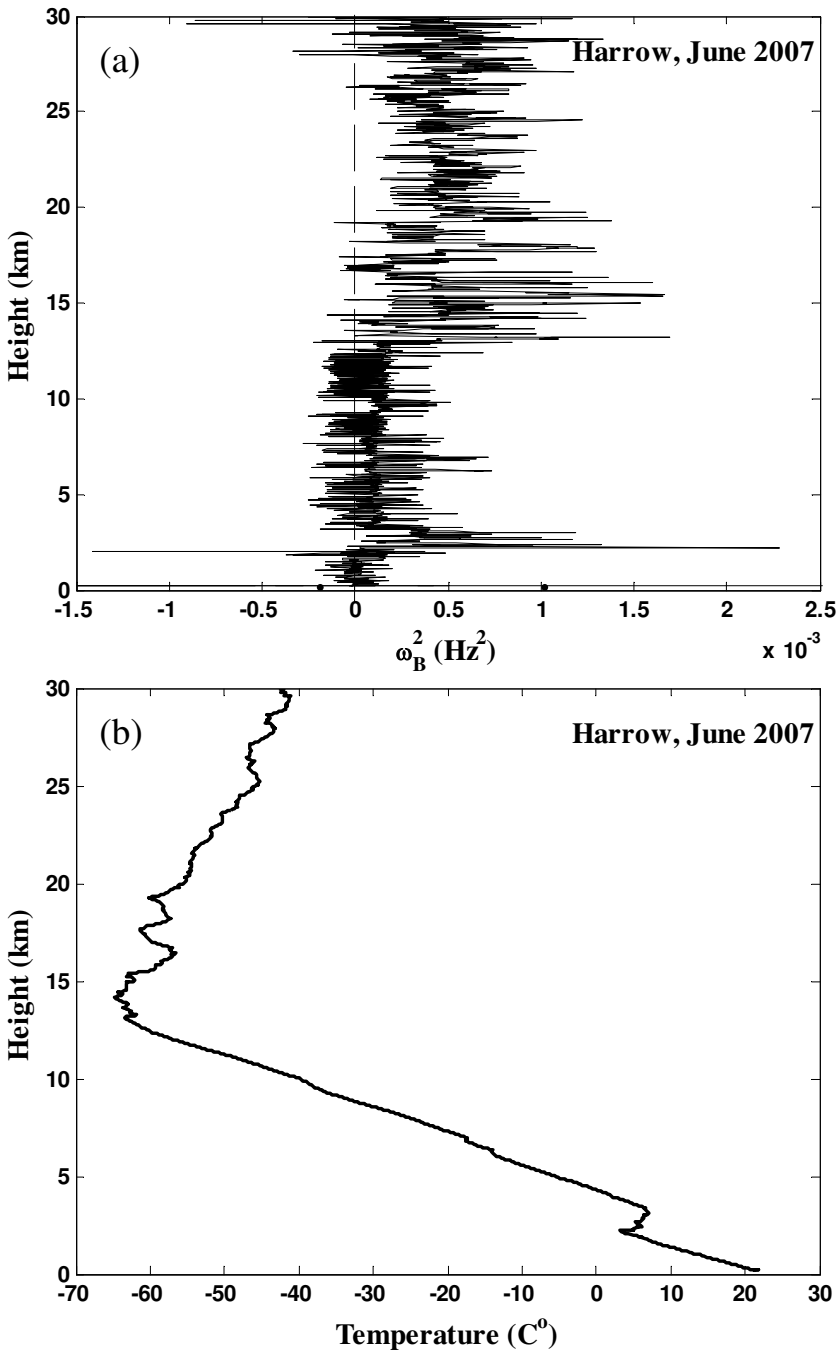

Figure 3.2: The vertical profiles of (a) the Brunt-Vaisala frequency squared, ω_B^2 and (b) temperature measured on June 26, 2007 at Harrow. The resolution is 15 m.

at 1×10^{-4}, 2×10^{-4} $\mathrm{H}z^2$ etc. It can be seen that 47% of the estimated Brunt-Vaisala frequencies have values of 10^{-4} $\mathrm{H}z^2$ within $\pm 0.5 \times 10^{-4}$ $\mathrm{H}z^2$. The percentage increases to 80% if we consider ω_B^2 with values of $10^{-4} \pm (1.5 \times 10^{-4})$ $\mathrm{H}z^2$. The vertical profile of ω_B^2 in Figure 3.3(b) also shows that the typical value of ω_B^2 is around 10^{-4} $\mathrm{H}z^2$ below 10 km. Note that below 2 km, the value of ω_B^2 increases to a maximum of 1.7×10^{-3} $\mathrm{H}z^2$. This may be due to the temperature inversion (increase of temperature with height in the troposphere) below 2 km, since the atmosphere is very stable during the inversion. The higher values of ω_B^2 below 2 km can affect the average value of ω_B^2. The average of ω_B^2 below 10 km is 1.6×10^{-4} $\mathrm{H}z^2$. However if do not include values below 2 km, the average changes to 1.2×10^{-4} $\mathrm{H}z^2$. Figures 3.3(c) and 3.3(d) are the same as Figures 3.3(a) and 3.3(b), except for the resolution which has changed to 120 m. This will smooth out the vertical profile of ω_B^2 and slightly changes the percentage in which ω_B^2 is within $\pm 0.5 \times 10^{-4}$ $\mathrm{H}z^2$ to 48%. Figure 3.4 presents the distribution and vertical profile of ω_B^2 measured on June 23, 2007 at Harrow. The results are similar to those in Figure 3.3. Note that the resolution (15 m) is higher at Harrow (Figures 3.4(a) and 3.4(b)). However, the data are smoothed to a resolution of 120 m in Figures 3.4(c) and 3.4(d). The distributions of ω_B^2 at Harrow shows that 42% and 80% of data with the resolution of 15 m, and 47% and 84% of data with the resolution of 120 m are within $\pm 0.5 \times 10^{-4}$ and $\pm 1.5 \times 10^{-4}$ $\mathrm{H}z^2$ respectively.

3.3 Variations of the Brunt-Vaisala Frequency in the Troposphere

In order to study the climatology of the Brunt-Vaisala frequency, distributions of the Brunt-Vaisala squared, ω_B^2 were determined for different days and months during February, March, June and July 2007 at Walsingham and Harrow. Then, the percentages that ω_B^2 values are within $(1 \pm 0.5) \times 10^{-4}$, $(1 \pm 1.5) \times 10^{-4}$ and $(0.25 - 4) \times 10^{-4}$ $\mathrm{H}z^2$ were calculated. In addition to that, measurement resolutions, averages and medians were estimated. The results for Walsingham and Harrow are shown in Tables 3.1 and 3.2 respectively. It can be seen that in general, measurements mostly are within $[1 \pm 0.5] \times 10^{-4}$ $\mathrm{H}z^2$. On average, the mean value and median of ω_B^2 is about $1.65 \times 10^{-4}$and 1.26×10^{-4} $\mathrm{H}z^2$ respectively. Therefore, using the value of 10^{-4} Hz for ω_B^2 in our calculation is reasonable.

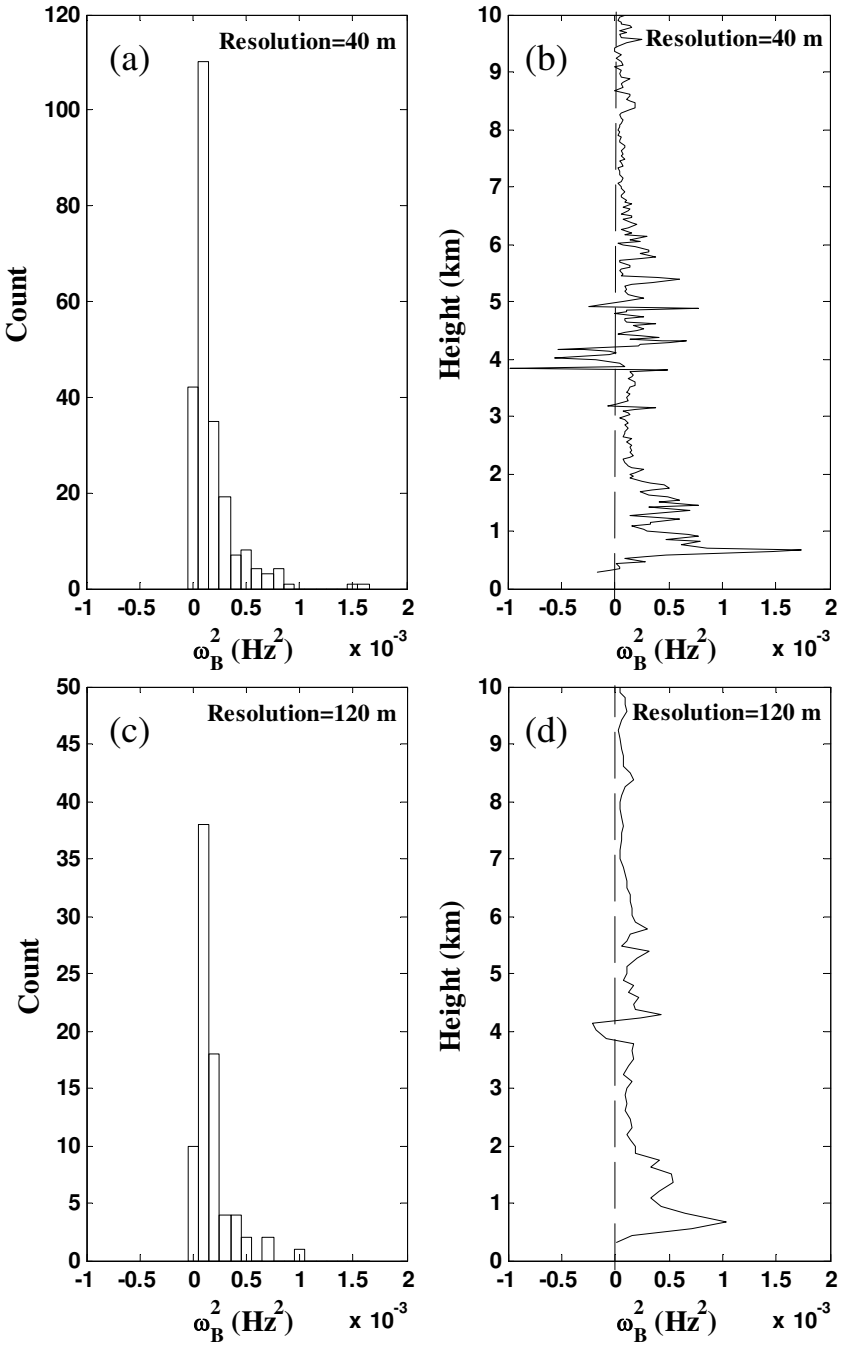

Figure 3.3: (a) The distribution and (b) the vertical profile of the Brunt-Vaisala frequency squared, ω_B^2 measured on March 2, 2007 at Walsingham with a resolution of 40 m. (c) and (d) the same as (a) and (b), but data have been smoothed to resolution of 120 m.

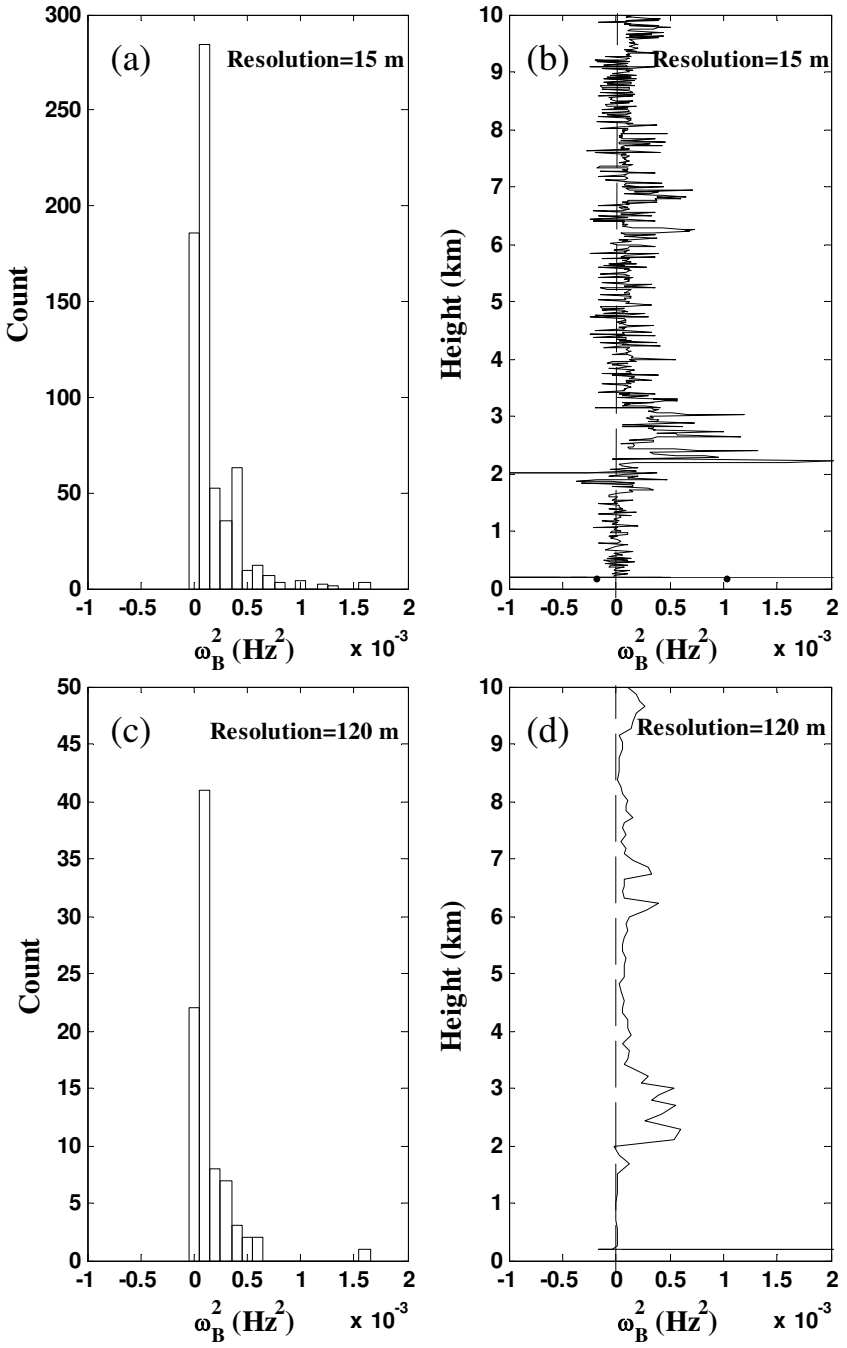

Figure 3.4: (a) The distribution and (b) the vertical profile of the Brunt-Vaisala frequency squared, ω_B^2 measured on June 26, 2007 at Harrow with a resolution of 15 m. (c) and (d) the same as (a) and (b), but data have been smoothed to resolution of 120 m.

ω_B^2	within $[1 \pm 0.5] \times 10^{-4}$ (Hz^2) %	within $[1 \pm 1.5] \times 10^{-4}$ (Hz^2) %	within $[0.25 - 4] \times 10^{-4}$ (Hz^2) %	resolution (m)	mean $\times 10^{-4}$ (Hz^2)	median $\times 10^{-4}$ (Hz^2)
Feb 25	33	74	73	36	2.01	1.35
Feb 26	40	83	76	30	1.53	1.02
Feb 27	43	78	86	44	1.86	1.25
Feb 28	39	73	82	27	1.98	1.45
Mar 1	30	76	68	28	1.80	1.09
Mar 2	47	80	80	40	1.64	1.14
Mar 3	33	70	72	38	2.24	1.42
Mar 4	38	69	81	44	2.21	1.58

Table 3.1: Statistical studies of ω_B^2 at Walsingham in February and March 2007, during evening hours. Note that the third column assumes an asymmetric distribution.

ω_B^2	within $[1 \pm 0.5] \times 10^{-4}$ (Hz^2) %	within $[1 \pm 1.5] \times 10^{-4}$ (Hz^2) %	within $[0.25 - 4] \times 10^{-4}$ (Hz^2) %	resolution (m)	mean $\times 10^{-4}$ (Hz^2)	median $\times 10^{-4}$ (Hz^2)
Jun 23	27	66	62	14	1.01	1.23
Jun 26	39	80	70	16	1.30	1.21
Jun 27	20	71	66	26	1.08	1.29
Jun 28	12	76	62	21	1.57	1.57
Jun 29	27	80	59	23	1.86	1.24
Jul 3	24	82	64	25	1.64	0.98
Jul 4	25	78	64	22	1.08	1.06

Table 3.2: Statistical studies of ω_B^2 at Harrow in June and July 2007, during morning hours. Note that the third column assumes an asymmetric distribution.

3.4 Conclusion of the Brunt-Vaisala Frequency Study

The estimation of the Brunt-Vaisala frequency, ω_B is needed for calculation of the turbulent energy dissipation rate, ε. ω_B is related to ε through $\varepsilon = C\omega_B\sigma_t^2$, where C is a constant and σ_t^2 is the spectral width. We discussed extensively about σ_t^2 and errors associated with this parameter in Chapters 2 and 3, and we examined the variation of ω_B in the troposphere in this chapter. In this thesis, we have used $\omega_B = 10^{-2}$ Hz for calculation of ε. It may be seen that our studies in this chapter have shown that the error due to variation of ω_B will be no worse than about a factor of 2 (the fourth column in Tables 3.1 and 3.2). In terms of other errors associated with ε, a factor of 2 is not considered as large for atmospheric turbulence.

Chapter 4

Comparisons of Energy Dissipation Rates Measured by Radar and Aircraft

In-situ measurements obtained from probes mounted on research and commercial aircraft can be used to characterize turbulence in the lower and middle atmosphere. It is the aim of this chapter to compare radar-estimated energy dissipation rates by comparing them with aircraft measurements. Rather than try and compare the data on a point-by-point basis, which is notoriously difficult for turbulence due to its inherent variability, we collect a large number of data sets and compare the two techniques in a statistical sense. The structure function method has been used to extract turbulent energy dissipation rate from wind data measured by Twin Otter aircraft. In addition, energy dissipation rates, ε measured by commercial aircraft were estimated during flight inside the aircraft, and spectral analysis was used to extract ε from wind speeds. The details of measurement techniques and methods mentioned above have been given in Chapter 2. In this chapter, we concentrate on the analysis of aircraft measurements and comparisons of different methods.

4.1 Twin Otter Data Processing

The aircraft measurements were obtained by Twin Otter aircraft during the Border and Air Quality and Meteorology Study (BAQS-Met) campaign conducted by a collaboration of university and government researchers (e.g. He et al., 2011) in June 2007. The aircraft was flown over Harrow in Southwestern Ontario. The three levels

Flight level	Date	Altitude (km)	Duration (min)	Aircraft speed (m/s)	Flight distance (km)
703	23-06-2007	1.4	46	68	188
709	26-06-2007	0.5	53	64	205
713a	27-06-2007	0.5	19	64	73

Table 4.1: Summary of level flight segments of Twin Otter aircraft.

of flight segments selected for the analysis are summarized in Table 4.1.

In order to estimate the structure function and energy spectrum (see sections 1.6.11.1 and 1.4), the first step is to find u_L, the horizontal velocity component along the direction of the flight path (longitudinal), u_N the horizontal velocity component normal to the flight path (transverse), and w, the vertical velocity.

These relate to the geographic components through the following equations (Frehlich and Sharman, 2010):

$$\begin{aligned} u_L &= u_{East} \sin\Psi + u_{North} \cos\Psi, \\ u_N &= u_{East} \cos\Psi - u_{North} \sin\Psi, \end{aligned} \tag{4.1}$$

where u_{East} and u_{North} are the east and north velocity components and Ψ is the aircraft heading.

In order to estimate the energy dissipation rate, ε the second-order structure functions were calculated from time series of velocity as:

$$\begin{aligned} D_L(r) &= \overline{[u_L(t + r/V_a) - u_L(t)]^2}, \\ D_N(r) &= \overline{[u_N(t + r/V_a) - u_N(t)]^2}, \\ D_W(r) &= \overline{[u_w(t + r/V_a) - u_w(t)]^2}, \end{aligned} \tag{4.2}$$

where D_L, D_N and D_W are the parallel, normal and vertical components of the structure function respectively. V_a is the aircraft speed and r the separation distance. Assuming isotropic turbulence, ε can be determined from Equations (1.43) and (1.44). Figure 4.1 shows the estimated structure functions of three components of wind as a function of r for the flight segment of 709. Structure functions were calculated for approximately 90-second intervals, representing 3000 data points per interval.

In Figure 4.1, there are two regions with linear slopes. The first region occurs at

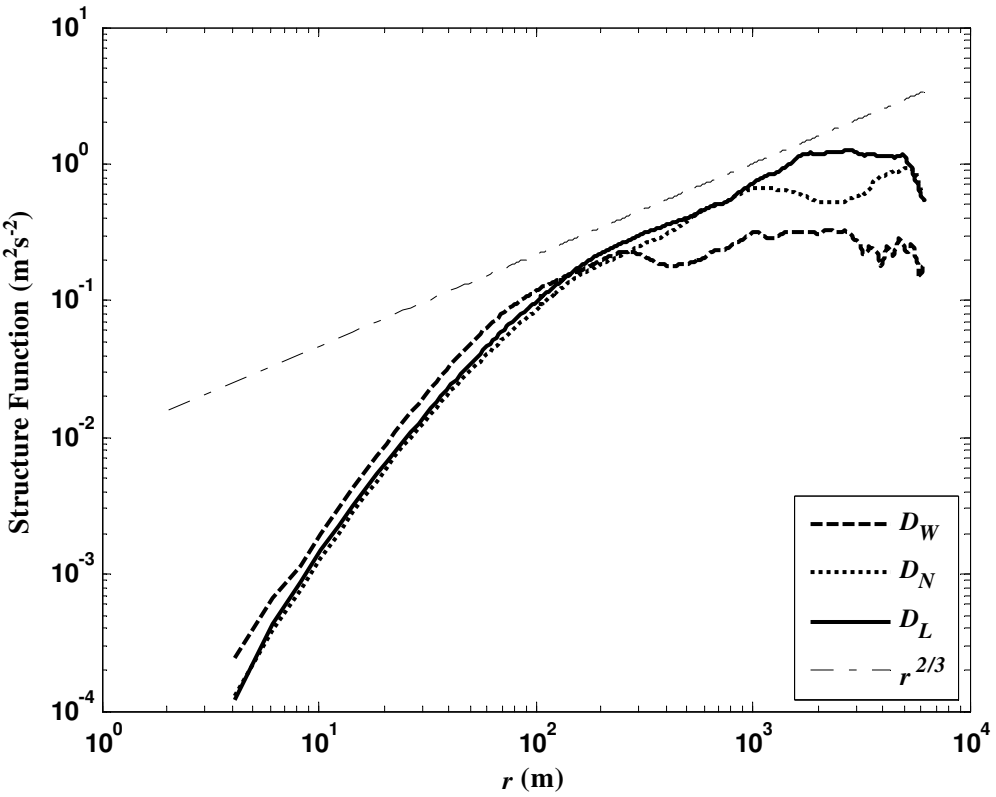

Figure 4.1: Structure functions from the flight segment of 709 as a function of separation distance. The dashed, dotted and solid lines represent the vertical, normal and longitudinal wind components respectively. The dotted-dashed line shows $r^{2/3}$.

scales smaller than 100 m in which the structure functions show power-law exponents higher than the Kolmogorov 2/3 exponent. This is not due to the short duration of segments, since we can see this behavior even in longer segments. This is also not due to viscosity. The viscous range occurs at scales smaller than approximately a few millimeters. Note that at this range, D_L, D_N and D_W are similar in magnitude and follow the same shape. However, they deviate at larger scales. This may be due to the fact that larger scale motions (buoyancy effects) tend to suppress vertical motions (anisotropic turbulence). The plateau shape at larger scale is expected for separation distances much greater than the largest eddies (Wroblewski et al. 2010) and clearly shows separation of scales. It can be seen that the plateau occurs at approximately 1500, 1000 and 300 m for D_L, D_N and D_W respectively in Figure 4.1. These values can be considered as indirect measures of largest scale eddies (buoyancy scales). The second region with the linear slope occurs at intermediate scales (between 100 m and buoyancy scale) and has a slope of 2/3 (Kolmogorov 2/3 law). Therefore, we can assume that this region is associated with isotropic turbulence. We will use this region for calculating the energy dissipation rate, and justify this assumption further shortly.

The structure functions in figure 4.2 show a similar pattern to those in Figure 4.1. The Kolmogorov region occurs at scales between 100 to 400 m. A notable feature that can be seen in Figure 4.2 at larger scales is that the slope increases significantly above the Kolmogorov range. This could be due to the aircraft trajectory effect. Lovejoy et al. (2004) showed that structure functions can be affected by aircraft trajectories at larger scales, since the aircraft no longer smooths out altitude fluctuations. However, Wroblewski et al. (2010) showed that measurements at sub-kilometer scales are more likely contaminated by trajectory effects. The same authors also suggested that the deviation from the Kolmogorov scaling exponent could be a transition between smaller-scale turbulence, adjusting to larger scales. Strong anisotropy can also affect the scaling exponent of 2/3. Another possible reason is bursts of gravity waves into turbulence which may inject an additional energy to smaller scales (e.g. Yague et al., 2006) leading to deviation of the structure function slope from the isotropic slope.

An alternative method for estimating energy dissipation rate, ε, employs spectral analysis. Assuming turbulence is isotropic, ε can be determined by the Kolmogorov -5/3 law given by Equation (1.15). Figure 4.3(a) shows a vertical velocity energy spectrum and Figure 4.3(b) shows the structure function for the same set of data used in Figure 4.3(a). The dotted-dashed lines in figure 4.3(a) and 4.3(b) corresponds to $r^{-5/3}$ and $r^{2/3}$ respectively. Based on Kolmogorov laws, the spectrum of fluctuations

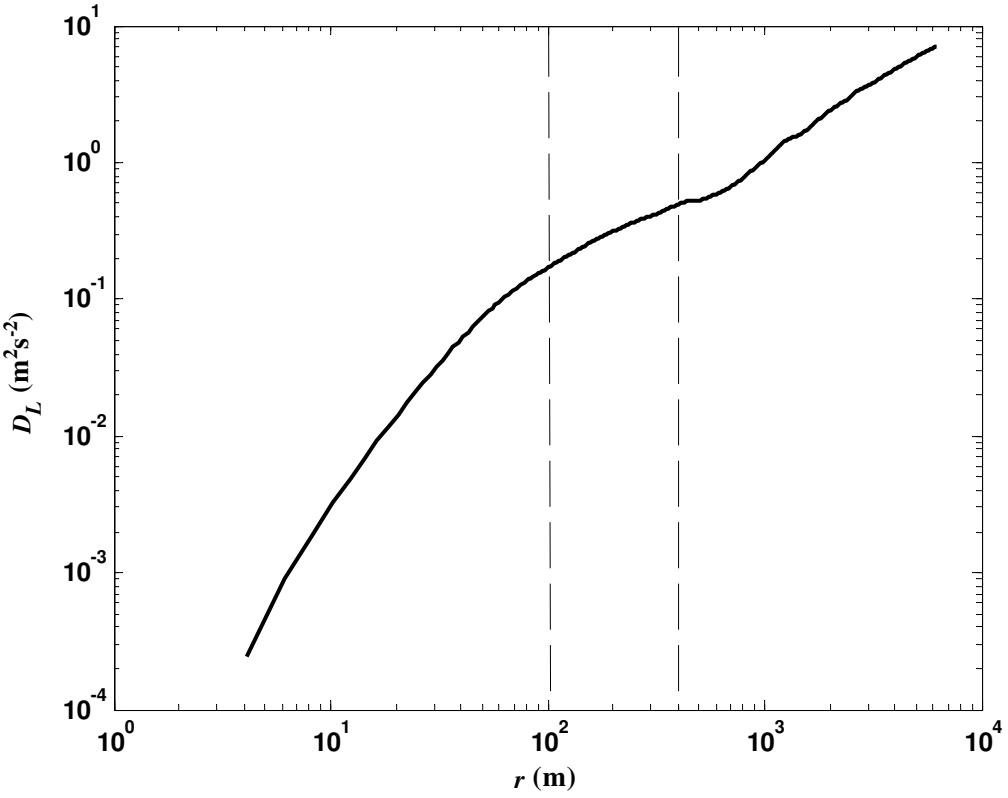

Figure 4.2: The parallel structure function from the flight segment of 709 as a function of separation distance. The vertical dashed lines show the beginning and end of Kolmogorov slope.

and structure function should follow the -5/3 and 2/3 slopes respectively for isotropic turbulent scales. It can be seen from Figure 4.3(a) that the spectrum is inherently noisier than structure function which makes it difficult to find the isotropic regions. In addition to this, structure functions can be calculated in a more straight forward way. They can be applied to any length of data and there is no need to remove the mean velocity. Another advantage of structure functions is the direct connection between the 'scales' and the result of measurements (Lindborg, 1999) and the fact that it is easier to find the transition from Kolmogorov scaling. Thus, we use the structure function method for this study. However, the spectrum does show clearly the impact of noise. As can be seen, the spectrum to the right of the vertical dashed line tends to flatten, and also there are some clear peaks. These effects are due to noise and instrument impact, concluding that no useful data can be expected at inverse scales greater than 6×10^{-2} m^{-1} (vertical dashed line in Figure 4.3(a)) or physical scales less than about 16 m. A scale of 16 m is also shown in Figure 4.3(b). From Figure 4.3(b), a 2/3 law does not settle in until a scale of $\sim$ 100 m, so even the region between 16 and 100 m seems impacted by noise and instrument effects. Therefore, we conclude that no useful information can be obtained from these in-situ measurements at scales $\leqslant$100 m. This will be important for our subsequent analysis.

Using Equations (1.43) and (1.44), values of energy dissipation rate were found using scales $>$ 100 (m). The results are summarized in Figure 4.5. Each estimated energy dissipation rate, ε, corresponds to 90 seconds of measurements. These short time estimates can provide us with information on local behavior of turbulence. The variations seen in time series of ε may be due to the intermittency or bursting nature of turbulence. Turbulence is intermittent both temporally and spatially in the atmosphere and it often occurs in thin layers which are separated by regions of weakly turbulent or semi-laminar (Hocking, 1999). It can also be seen that in general, ε values cover a range of order of magnitude between 10^{-3} and 10^{-7} W/kg. However, only values greater than 10^{-4} W/kg are reliable.

An ε value of 10^{-4} W/kg is associated with the buoyancy scale, L_B (the scale at which the transition between inertial subrange and buoyancy ranges begins) of about 100 m. This can be estimated through the following equation:

$$L_B \approx (2\pi/0.62)\varepsilon^{1/2}\omega_B^{-3/2}, \tag{4.3}$$

where ω_B is the Brunt-Vaisala frequency (see Chapter 4 for more detail). As we have discussed, structure functions are unreliable at scales $\leqslant$ 100 m, so if the buoyancy scale is less than 100 m, it is impossible to see a Kolmogorov spectrum This is possibly

Structure functions at 300	Percentage of structure functions > 0.2 m^{2}s^{-2}	Percentage of structure functions > 0.2 m^{2}s^{-2} that have a 2/3 slope
Vertical	27 %	38 %
Longitudinal	33 %	50 %
Normal	32 %	20 %

Table 4.2: The percentage of reliable measurements of energy dissipation rate using structure function method.

due to noise or influence of anisotropy. In the case of anisotropy, eddies have horizontal scales much greater than their vertical scales. Therefore, horizontal scales may be measured when vertical ones can not. This can affect the behavior of structure function. Hence, we will only consider ε values greater than 10^{-4} W/kg to avoid the effect of anisotropy and noise.

One should note that the missing data in Figure 4.5 are due to the fact that the structure functions did not exhibit (e.g. Figure 4.4) the expected $r^{2/3}$ associated with the inertial subrange. We noticed that only few percentage of measurements show the 2/3 scaling exponent.

As an exercise, we calculated the structure function at 300 m for 3 components of wind and determined the percentage that structure functions are greater than 0.2 m^{2}s^{-2} (corresponding to the energy dissipation of 10^{-4} W/kg). This estimation crudely allows us to only examine cases of large ε ($\varepsilon > 10^{-4}$).

We then found the percentage of values for which the structure functions are both larger than 0.2 m^{2}s^{-2} and have a 2/3 slope. The results are shown in Table 4.2. It is seen that typically less than half of the measurable structure functions more than 0.2 m^{2}s^{-2}, exhibit a Kolmogorov spectrum.

4.2 Commercial Aircraft data analysis

The data used for the analysis in this section are measured by Delta airline aircraft over Detroit. The algorithm used to estimate energy dissipation rate, ε on board was developed by the National Center for Atmospheric Research (NCAR). The details of this algorithm are given in Chapter 2. In general, spectral analysis was used to estimate and report ε values. twelve spectra were produced per minute and $\varepsilon^{1/3}$ was estimated from each spectrum. In order to save communication costs, ε values were

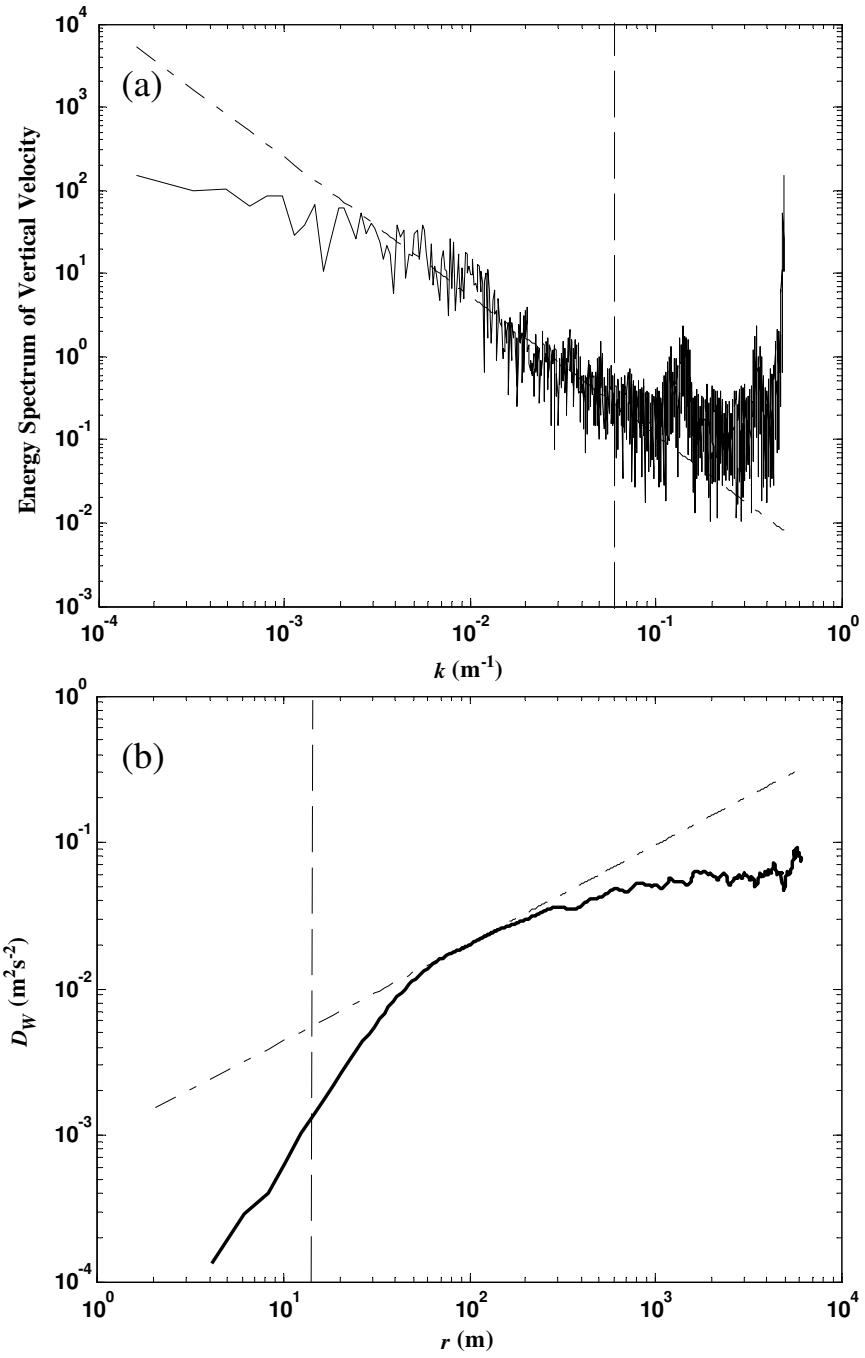

Figure 4.3: (a) Energy spectrum of vertical wind as function of wave number (k) for flight segment of 713a. The dotted-dashed line shows $r^{-5/3}$. (b) Structure function of normal wind as a function of separation (r) for the same data in (a). The dotted-dashed line shows $r^{2/3}$. In both figures, vertical dashed lines represent the noise cut-off scale.

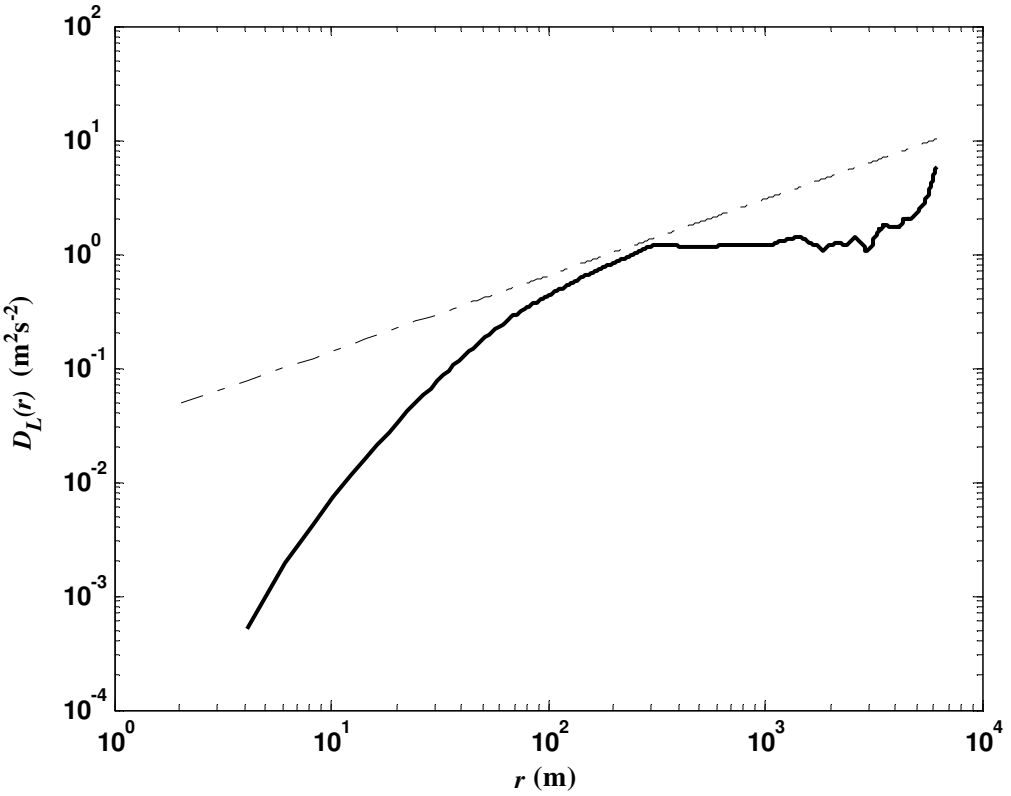

Figure 4.4: Structure function of longitudinal wind as a function of separation (r) for flight segment of 713a. The dotted-dashed line shows $r^{2/3}$.

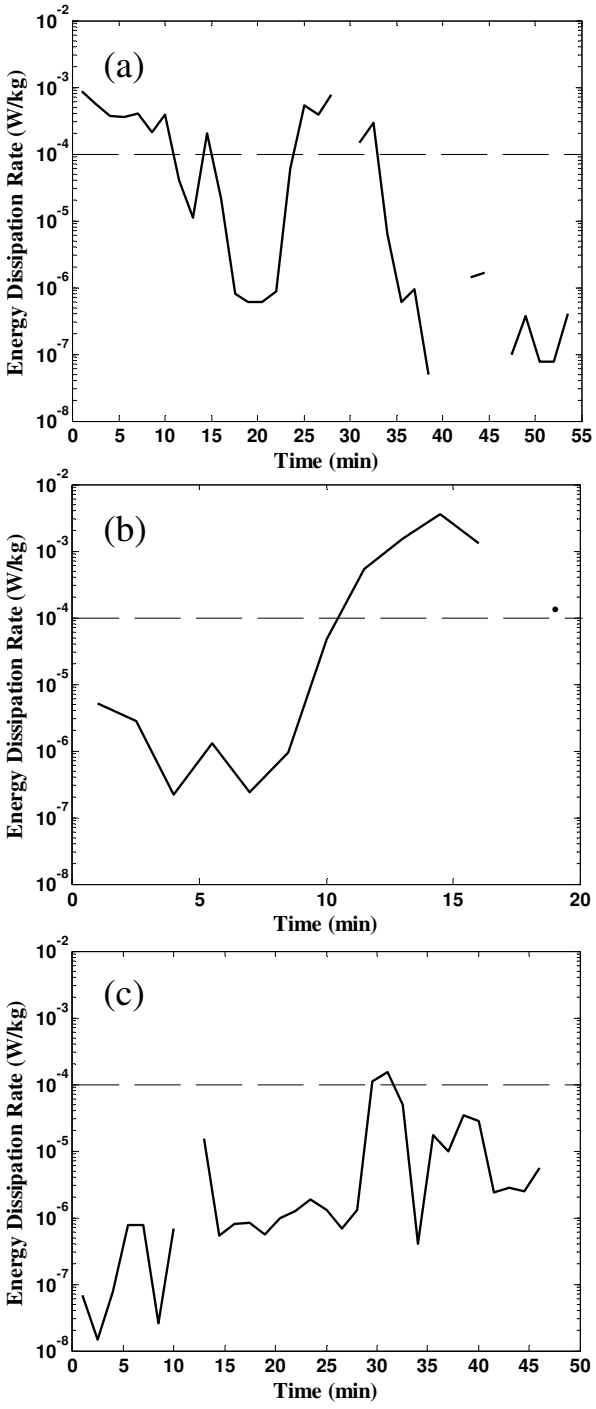

Figure 4.5: Time series of the energy dissipation rate, ε, estimated using structure functions for the flight segment of (a) 709, (b) 713a and (c) 703.

binned from 0 to 0.02, 0.02 to 0.04 $(W/kg)^{1/3}$ etc., and reported to the operational users. The reported zero values are not necessarily zero, but they are below the threshold value (e.g., "moderate" or "light to moderate"). Figure 4.6(a) shows the estimated energy dissipation rates, ε from commercial aircraft as a function of measurement event number rather than time, since there is more than one measurement per minute and we are mostly interested in the range of measured ε. The graph covers all heights from 150 m to 12.5 km (see figure 4.7(a)) for June 2009. Figure 4.6(a) also reveals that most of the measurements are zero or very small, correspond to weak turbulence. Occasionally they become very large which corresponds to intense turbulence. Figure 4.6(b) is the distribution of data used in Figure 4.6(a), however, zeros are removed. It can be seen that the majority of estimated ε have an order of magnitude that changes approximately from 10^{-5} to 10^{-3} W/kg.

Figure 4.7(b) shows the vertical profile of percentages of "zero ε" measured by aircraft during June, 2009. Note that each measurement corresponds to an average over 1 km. This means that the percentage at 1 km is the average of zero percentages from 0.5 to 1.5 km etc. Zeros are associated with very weak or light turbulence and Figure 4.7(b) shows that the percentage of zeros can exceed 90 %, indicating that intermittency is a common characteristic of turbulence in the atmosphere which is caused by sporadic and episodic instabilities (e.g. Mahrt, 1989). In order to compare the aircraft-estimated ε during different periods of 2009 and 2010, we produced cumulative histograms of ε data for all heights (from 150 m to 12.5 km) using the probability that the abscissa is exceeded. The results are shown in Figure 4.8. It can be seen that the probability that the measured ε exceeds 10^{-6} is 100 % dropping to approximately 10 % for 10^{-3} W/kg and to about 1 % for 10^{-2} W/kg.

4.3 Comparisons of Aircraft and Radar Measurements

In Figure 4.9, we show the cumulative distributions of estimated energy dissipation rate, ε, using commercial aircraft, Twin Otter aircraft and our radar at Harrow. Data are taken at different times, but all were near Harrow. Note that the least positive value obtained by radar have an order of 10^{-8} W/kg and the minimum non-zero values of ε measured by commercial and Twin Otter aircraft have an order of 10^{-6} and 10^{-8} W/kg respectively. In order to compare these measurements properly, distributions in Figure 4.9 have been produced only for ε values of greater than 10^{-6} W/kg. We

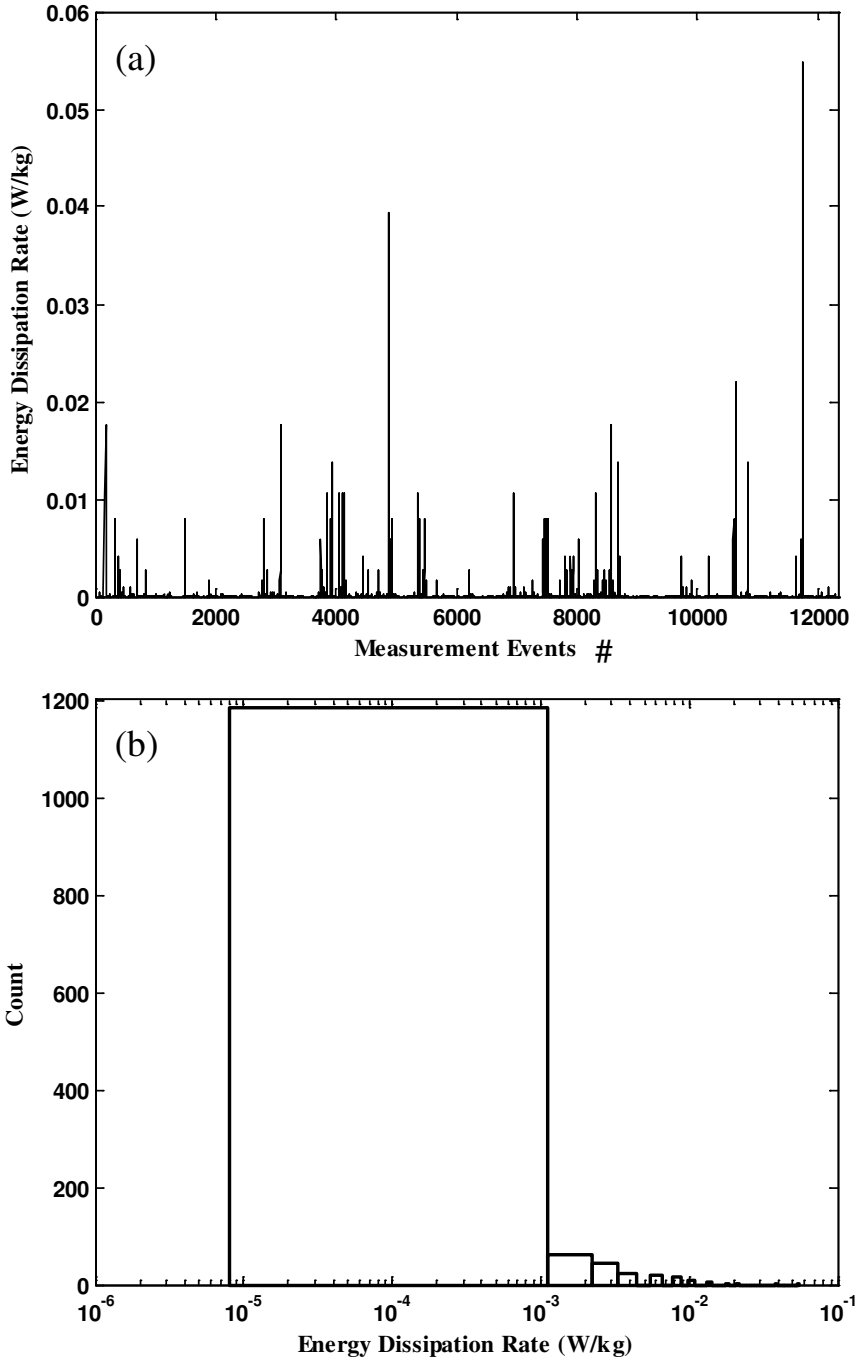

Figure 4.6: (a) Energy dissipation rates as a function of number of events for Delta airline during June 2009. (b) The distribution of energy dissipation rates for data used in (a). Zeros were not included, so percentage of "strong" turbulence events ($\geqslant 10^{-3}$ W/kg) is even less than the graph indicates.

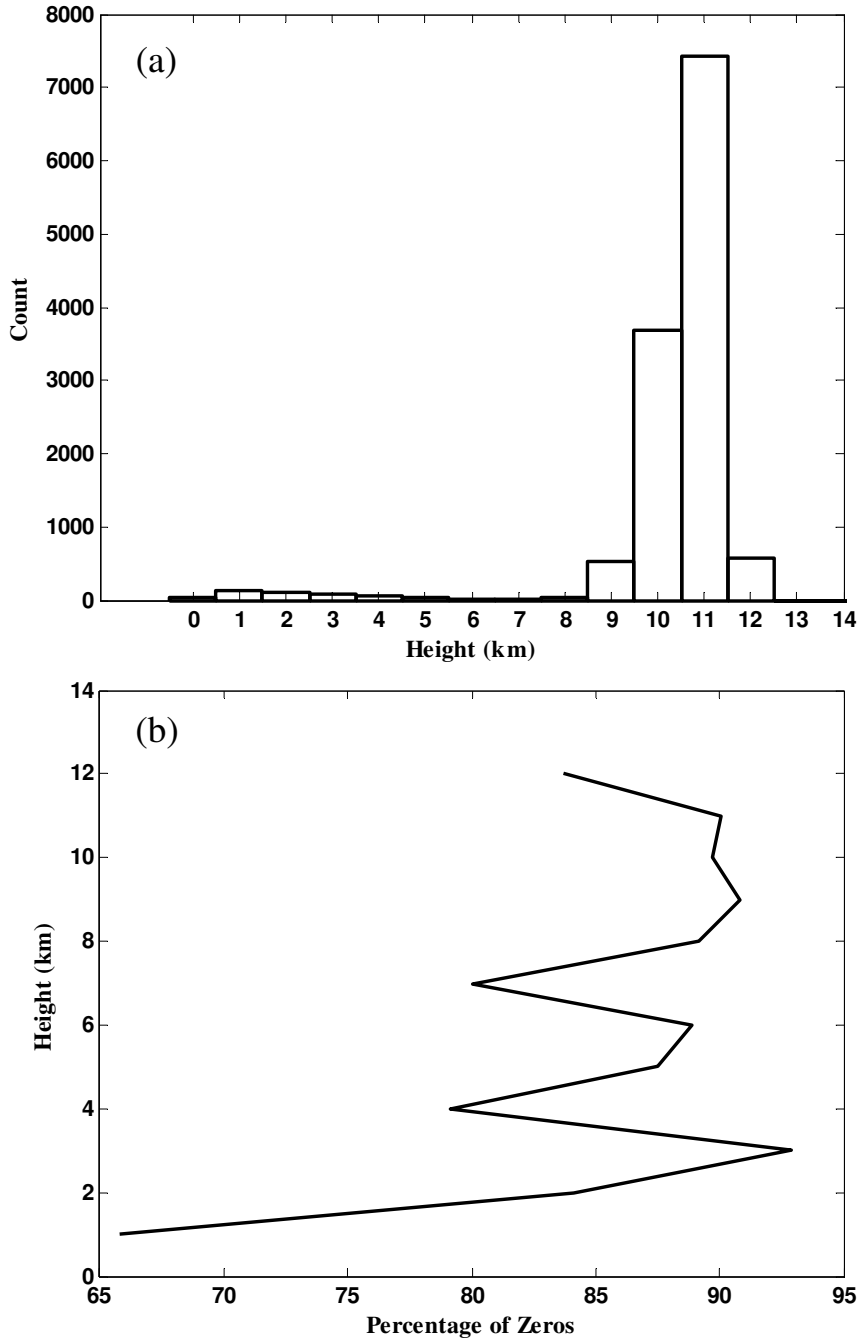

Figure 4.7: (a) The distribution of Delta aircraft altitude during June 2009. (b) The vertical profile of percentages that estimated energy dissipation rates were zero during June 2009. Each percentage represents an average over 1 km. Measurements are typically taken over the 8-12 km altitude range.

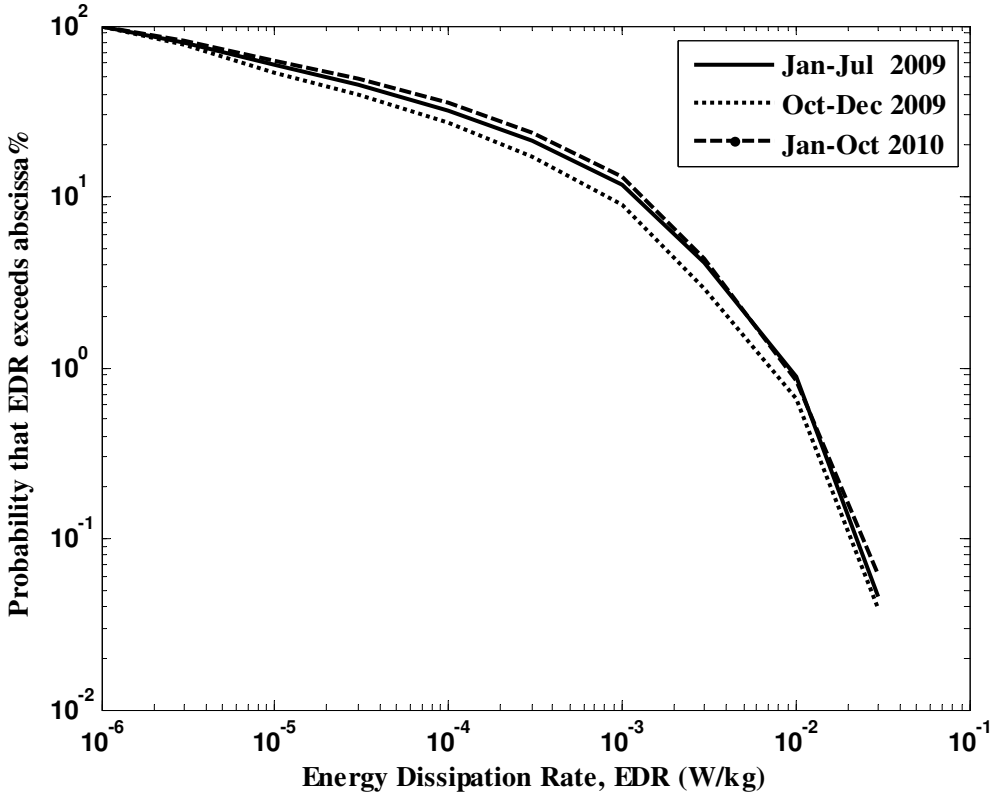

Figure 4.8: Inverse cumulative distributions of energy dissipation rates measured by Delta airline during the periods of January-June 2009, October-December 2009 and January-October 2010.

will discuss about the effect of zeros and negatives in Figure 4.10.

The commercial aircraft data were measured by Delta airlines at Detroit over a radius of 60 km from the Harrow radar and it covers a range of altitude between 150 m to 12.5 km. The Twin Otter measurements were performed at Harrow over the 0.5-1.5 km altitude range. For the purposes of comparisons, we will concentrate on the period of January-June 2009 since measurements of turbulence by radar are available for all these months. One should note that the aircraft data are computed during each minute and 1.5 minutes for commercial and Twin Otter aircraft respectively. However, the radar data are hourly averages. We need to use hourly averages in order to provide a mean wind profile with sufficient precision so that we can properly remove beam-broadening effects from radar spectral widths.

It can be seen from Figure 4.9 that measurements of energy dissipation rates by aircraft agree well with the radar measurements for the order of magnitudes of 10^{-6} to approximately 10^{-4} W/kg. However, the probability that the radar measures larger values of turbulence decreases more rapidly beyond this point. For example the chance of exceeding $\varepsilon = 10^{-3}$ W/kg is about 1 % for the radar, whereas the chances increase to about 12 % and 7 % for Delta and Twin Otter aircraft respectively. This is possibly due to the fact that hourly averages of radar data were used. Therefore, larger values get averaged out to lower values over the course of an hour. Furthermore, the method that has been used to estimate ε from radar data can affect the results. If the interest is only in the large values (the largest values can cause severe aircraft damage), we can use an interesting approach. We can assume that beam-broadening effect is zero since for the largest values of turbulence the effect of beam-broadening is minor. This allows us to use higher percentage of the data, since we do not need to know the beam-broadened spectral width. We can then show the measured (instantaneous) spectral widths. This will shift up the radar cumulative distribution (solid line in Figure 4.9) to the higher percentages (dotted line in Figure 4.9). For example, the probability that ε exceeds a value of 10^{-3} W/kg increases to about 7 % compared to 1 % when we removed the beam-broadening effects.

Figure 4.10 shows the cumulative distribution of aircraft and radar data when zero and "negative" values of energy dissipation rates are included. These negative and zero values are associated with very weak turbulence. However, we are not aware of the exact values of ε associated with these regions of weak turbulence. This makes the comparisons difficult and probably there is not a proper way to do it. However, we are interested in understanding how weak turbulence would affect our results. Therefore, we assumed that all the negative and zero values and all the values

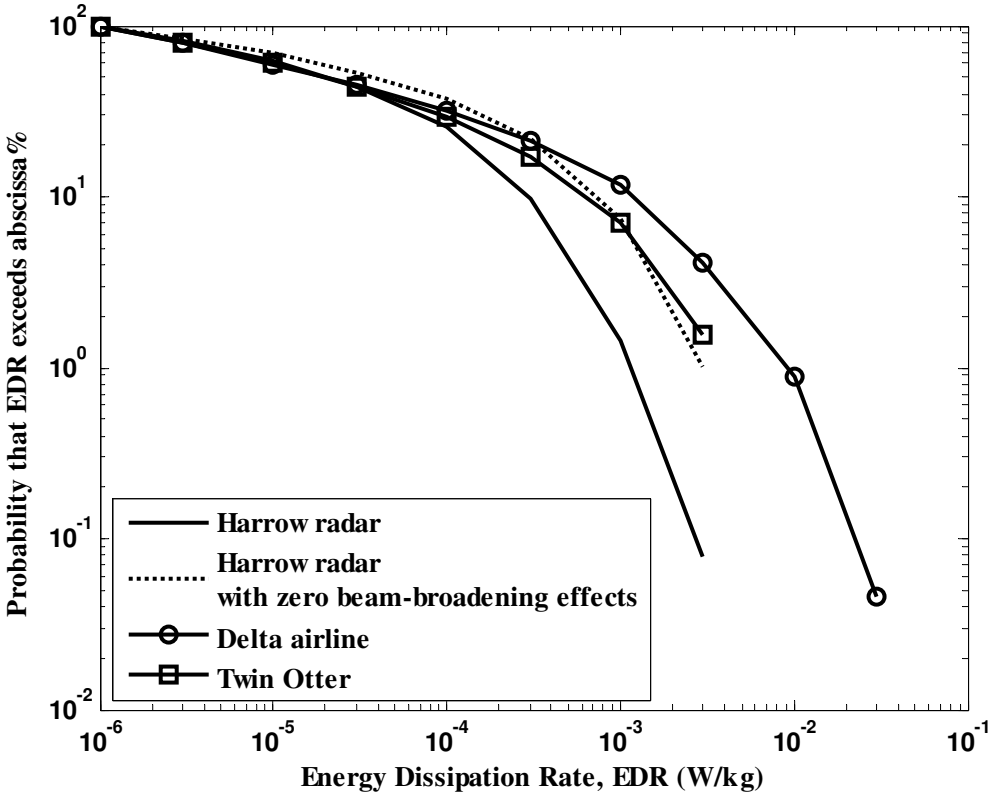

Figure 4.9: Inverse cumulative distributions of energy dissipation rates measured by different techniques. The solid and dotted lines represent measured energy dissipation rate by the Harrow radar for cases when the beam-broadening effects are removed and it is assumed that the beam-broadening effects are zero, respectively. The solid lines with circle and square marks represent Delta and Twin Otter aircraft, respectively. The Harrow and Delta data were measured during January-June 2009, and Twin Otter data were measured in June 2007.

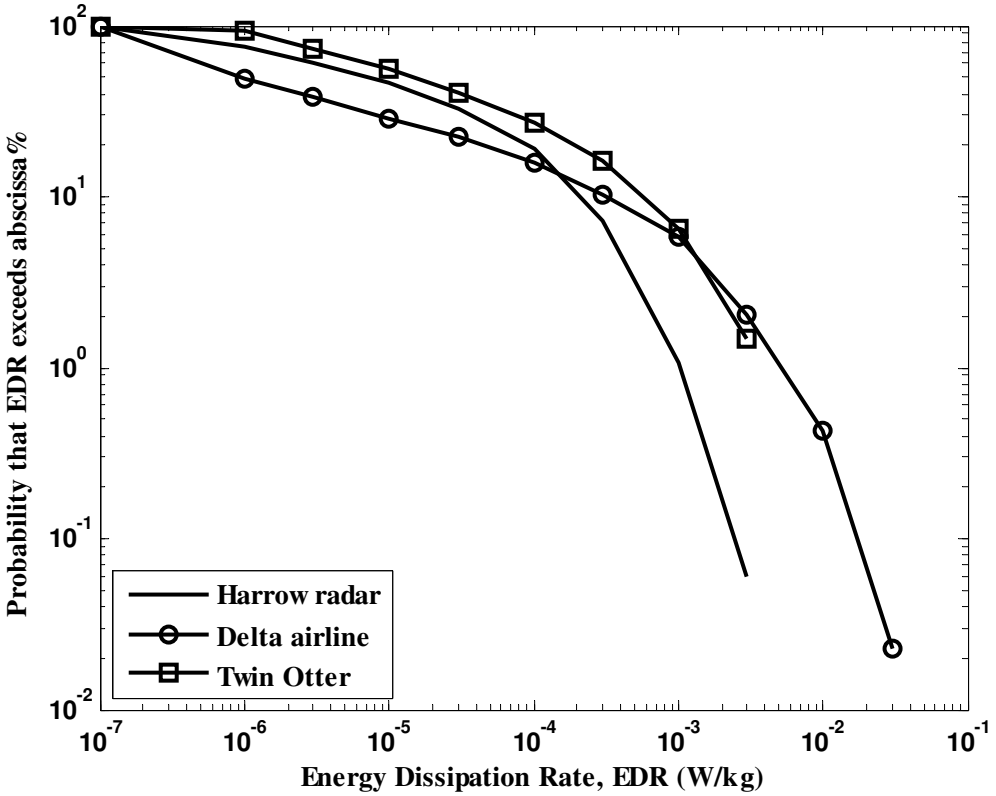

Figure 4.10: Inverse cumulative distributions of energy dissipation rates measured by different techniques. The solid line and lines with circle and square marks represent the Harrow, Delta and Twin Otter aircraft data including values smaller than 10^{-6} respectively), negatives and zeros. The Harrow and Delta data were measured during January-June 2009 and Twin Otter data were measured in June 2007. Note that the Delta airline data are mostly for 8-10 km, while the Twin Otter data are for 0.5-1.5 km

smaller than 10^{-6} W/kg have an order of magnitude of 10^{-7} W/kg. This is of course a crude approximation, but it enables us to display the effects of zeros and negatives. The results in the figure show that at smaller values of energy dissipation rate, the probability for Delta aircraft drops to a maximum of 25 % compared to the radar. Therefore, there is a smaller chance for commercial aircraft to measure ε values below approximately 10^{-4} W/kg. This is probably due to the fact that the radar beam and pulse cover a volume of typically few km across, and 0.5 km deep. Therefore, all patches of turbulence produce radar signal. On the other hand, the aircraft must fly through the turbulent patch to make a measurement. The percentage did not drop for Twin Otter data, possibly because measurements are limited to about 2 hours at lower altitudes (where turbulence is less intermittent) and only few small values of energy dissipation rate were measured. At values greater than about 10^{-4} W/kg, the probability that aircraft measure larger values of ε is greater than radar. Hence, including weak values did not affect the distributions at larger values. In general, the energy dissipation rates in Figures 4.9-4.10 are consistent with figure 14 of Hocking and Mu (1997) in which the distributions of radar and in-situ data have been presented.

Chapter 5

Discussion, Conclusions and Suggestions for Future Work

5.1 Discussion

This research was focused on studying the factors that affect turbulence measurements in the troposphere using radars. The data used were collected with the Walsingham, Harrow, and Negro Creek radars located in Southwestern Ontario. In order to estimate energy dissipation rate, the spectral-width method was applied to radar spectra. The spectral-width method utilizes the difference between the measured spectral-width and beam-broadening width (non-turbulent). The main body of this research can be divided into 4 parts: (1) the study of possible reasons for negative turbulence strengths as a result of using the spectral-width method; (2) developing a model for more reliable estimations of beam-broadening widths; (3) calculating of errors in determination of turbulence; (4) verifying the radar-estimated turbulence by comparing to high-resolution in-situ measurements.

It is clear from this study that negative values for ε are not only likely, but are expected and are mainly caused by errors in estimation of experimental and theoretical (beam-broadening) width. In regard to reducing errors related to experimental width measurements, several possibilities exist. Clearly, longer data sets are advisable, but if they become too long, the advantage is offset by the fact that the turbulent scatterers may physically evolve during the sampling time. A data-length of 30-40 s is about optimum. It is also possible to reduce the errors by using higher radar frequencies. In order to reduce the beam-broadening effect, it is necessary to reduce δu in Equation (2.12). This could be achieved if the radar could measure both components of the

wind at the location of the turbulence simultaneously. With a Doppler system, this is not feasible, since the beam used to measure one component is physically distinct from the orthogonal partner(s). In our analysis, we have represented the mean wind by hourly averaged profiles. There may be advantageous if the wind measured at the time of the turbulence measurement were used, but since at least one component of the wind field is measured some distance away, this does not help a lot. If the beams are tilted at 10.9° off-vertical, then at an altitude of 5 km, each is approximately 1 km from the point immediately above the radar, and the two scattering regions are separated by at least 1.5 km. Distances double at 10 km altitude. In this regard, the spaced antenna method may have advantages, since it does measure both components of the wind at the same point in space, but then the spaced antenna reflections are often dominated by specular reflectors, making the results often unrelated to turbulence.

However, even if shorter averaging times are used for the generation of the background wind profile, the experimental spectral width still seems to be the dominant source of error, and reducing the theoretical errors (associated with beam-broadening) without further reducing experimental errors (associated with experimental width) has little effect on the overall error. Both spectral widths depend on the beam width, so clearly use of narrower beams helps, as is well known (e.g. Hocking, 1986). Judging from the graphs presented to date, the Negro Creek radar, with a one-way half-power half-width of 3.3°, represents something of an upper limit on useful beam widths for turbulence applications. This is broadly similar to the limit suggested by Hocking (1985, 1986), who suggested that an individual measurement of turbulence strength is only statistically reliable with reasonable confidence if :

$$\sigma^2 > 0.3\Theta_{1/2}^2 u^2 \tag{5.1}$$

where $\Theta_{1/2}$ is the beam two-way half-power half-width and u is the mean wind. That author also suggested that 3° was a reasonable upper limit for the radar half-power half-width if the radar was to be used to measure the strength of turbulence in the real atmosphere. Nevertheless, given that turbulence often involves bursts of severe activity, separated in space and time by much weaker events, even radars with wider beams can have some useful application in identification and measurement of strong events.

One important point that arises is that when forming averages or medians, both positive and negative values of ε need to be included. The positive and negative parts of the distribution flow smoothly into each other, and there is no evidence

that the negative values refer to a different physical process. Indeed our theoretical calculations suggest that negative values are expected for statistical reasons.

Therefore another point which needs to be discussed is the accuracy involved in using positive-only estimates of turbulence. For example, some authors have chosen to ignore negative values, and Figure 2.2 in this work presents positive–only data (for visualization purposes only). The question arises – how much error occurs if we ignore the negative values? In Figure 5.1, the ratio of the mean value deduced using all data (including negatives), divided by the value deduced using positive data only, is presented as a function of the percentage of negative values. Data from all 3 graphs show a very similar curve. The dotted lines shows a theoretical calculation on this ratio, calculated assuming a Gaussian distribution. We have calculated the quantity:

$$Z = < x > / \left[(1/\sqrt{2\pi}) \int_0^\infty \exp(-(x - < x >)^2/2) dx \right] \tag{5.2}$$

which gives the ratio of the overall mean to the mean $< x >$ the quantity calculated using only positive values, and then calculated:

$$P = (1/\sqrt{2\pi}) \int_{-\infty}^0 \exp(-(x - < x >)^2/2) dx \tag{5.3}$$

which gives the area under the negative part of a Gaussian function with offset $< x >$, and then we have plotted the first against the second. The integrand is chosen so that the total area under the curve from -∞ to ∞ is unity.

A percentage of negatives of about 33 % corresponds to an error in the mean of a factor of 2, and a factor of 3 in error corresponds to a percentage of just over 40 %. It may seem that these are large values, but turbulence is a phenomenon with a large dynamic range, and a factor of 2 is not considered a large amount when making measurements with a radar. So even if the percentage of negatives is 30-40 %, using averages with positive values only, still gives information of moderate usefulness, so diagrams like Figure 2.3 are still of use in a qualitative sense. Studies which have used positive-only data may be useful too, but are unreliable when the percentages of negatives are in excess of about 35%, and certainly of little to no value when the percentage exceeds 43 %.

One additional point must be made. The radar naturally selects regions of strongest backscatter. Hence all our estimates of turbulence strengths are biased to regions of strong scatter. In the upper atmosphere, turbulence can be quite weak over much of the space, and spatially inhomogeneous. Strong burst of turbulence can occur which will be detected by the radar, while regions of relative calm will be

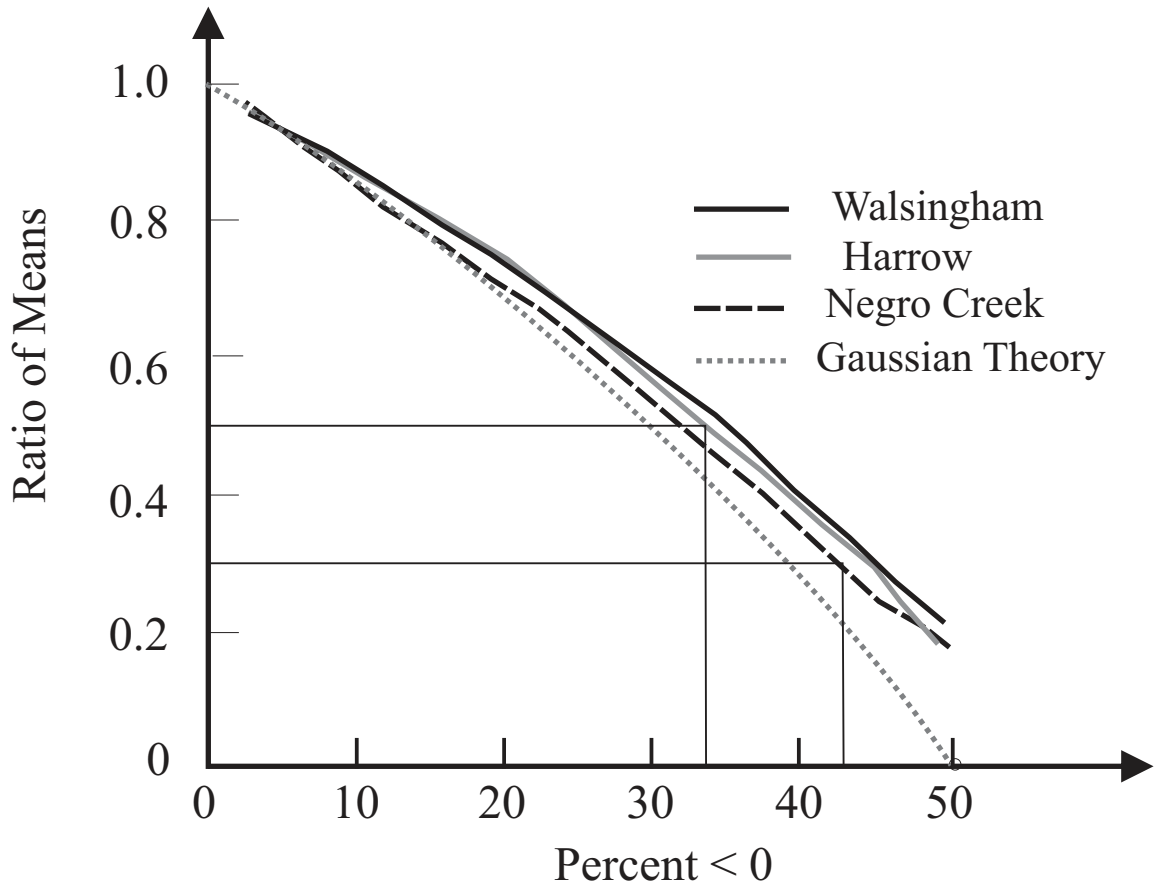

Figure 5.1: Plots of the ratio of the mean value of turbulence deduced using all data (positive and negative) relative to the value measured using positive values only, for the 3 radars at Walsingham, Harrow and Negro Creek. The Harrow and Walsingham data were for July, 2007, while the Negro Creek data were for July 2009 and September 2008. The theoretical graph expected for a Gaussian distribution is also shown for reference. It slightly underestimates the correct ratio at larger percentages due to the excess of large values of turbulence in the positive tail of the experimental distributions (which are the most important values from the perspective of atmosphere mixing and aircraft safety).

ignored. There is little that can be done to mitigate this, and this fact needs to be borne in mind during any interpretation.

We also studied the daily and monthly variations of the Brunt-Vaisala frequency mainly in the troposphere. The vertical profiles of the Brunt-Vaisala frequency, showed that the average value of the Brunt-Vaisala frequency squared, ω_B^2 is 1.65×10^{-2} Hz. In addition, the distributions of the Brunt-Vaisala frequency indicated that it is more likely that the values of $\omega_B = 1 \times 10^{-2}$ Hz within a factor of 2 in the troposphere.

Finally, short-time structure functions and spectral analyses were used to estimate energy dissipation rates from the Twin Otter and commercial aircraft. Analysis of aircraft data suggested that turbulence is intermittent in the altitude range of 0.5-10 km, specially above 1.5 km. The aircraft-estimated energy dissipation rates were compared to radar measurements using cumulative distributions. The comparisons showed that there is a good agreement between radar and aircraft measurements at lower values of energy dissipation rate ($10^{-6} - 10^{-4}$ W/kg) when the measured zeros by aircraft and measured negatives the radar were not included (Figure 2.11). Zero and negative energy dissipation rates are associated with regions of weak turbulence. When we include zeros and negatives in the cumulative distributions (Figure 4.10), the probability that commercial aircraft measure small values of energy dissipation rate drops 25 %. This can be explained by the fact that a radar beam cover a volume in the atmosphere and receive signals from any small turbulent patches inside the volume. Including the weak values of turbulence in the distributions did not affect the results for the Twin Otter significantly. At larger values, energy dissipation rates are averaged out by smaller values when measurements are made by radar. This explains why at larger values of turbulence, the probability of measurements is higher for aircraft.

5.2 Conclusions

We have studied measurements of turbulence strengths using 3 different radars, and compared characteristics. The following conclusions result.

1. While it is well known that narrower beam-widths are preferable for turbulence measurements, we have been able to make recommendations about the widest beams suitable for such studies. A one-way half-power half-width for the radar beam of less than 2.5° is highly desirable. Beam one-way half-power half widths which exceed 3.5° are not advised for Doppler-radar turbulence studies.

2. Negative values of the turbulent energy dissipation rate can occur, and indeed must occur. These arise due to statistical fluctuations of the mean wind on scales of minutes to hours, within the averaging interval. The main causes of negative values of ε are (i) errors in determination of the spectral width and (ii) choice of the mean wind profile used for calculation of the theoretical beam-broadened width. While these factors have been discussed in the literature previously, we have been able to develop expressions for quantifying their impact, and have been able to quantify the effect with our radars.

3. The impact of scatterer anisotropy seems to be a secondary concern in estimating ε.

4. Several formulas and methods were offered for determination of the theoretical spectral width, or equivalently, the variance σ^2. While all were generally similar, the most accurate was a model denoted as Cc. A general computer model (LS model) is still advised for dealing with cases of large and complicated shear. However, the model works well in the large percentage of calculations. A previously advocated model, denoted as model N, is shown to be a reasonable approximation to the true model, but may underestimate the true variance by typically 15 %. A new term has been added to the model N which improves its accuracy.

5. In calculating experimental widths, a fitting algorithm is highly advised, since calculation of weighted second order moments can lead to overestimates, and bias the experimental values to more positive values.

6. The daily and monthly analysis indicates that using the typical value of $\omega_B = 1 \times 10^{-2}$ Hz is reasonable.

7. There is a good agreement between radar and aircraft measurements at smaller values of energy dissipation rate when zero and negative values associated with very weak turbulence are not included.

8. The probability that aircraft measure larger values of turbulence, agrees reasonably well with radars when instantaneous values of turbulence measured by radars (using experimental spectral width only, allows us to measure near-instantaneous values of epsilon rather than hourly averages) are being used.

9. Regions of intense turbulence rarely occur in the atmosphere and appear as a sudden burst of turbulence followed by regions of weak turbulence.

5.3 Future Work

Future work may include studying the impact of using more reliable turbulence data in forecast and climate model results. This is specially important for aviation forecasts.

In regard to application of radars in meteorology, it is interesting to study the patterns and intensity of wind speed and turbulence during severe weather conditions, including tornadoes.

It is also interesting to investigate the effects of frontal systems on turbulence. This can be performed by looking at the locations of frontal systems on weather maps and estimating statistical characteristics of turbulence.

One point of considerable note is that a significant percentage of the spectra and structure functions measured by aircraft, show non-Kolmogorov behavior. The reasons for this need to be determined, and issues like the causes of the turbulence and the stage of development (generation, steady-state and decay) need to be further investigated.

It will also be useful to study the climatology of turbulence in places with different climatic conditions.

Appendix A

Turbulent Energy Dissipation Rate

The turbulent energy dissipation rate, ε can be determined through the following equation (Holmes et al., 1996):

$$\varepsilon = 2\nu < s_{ij}s_{ij} >= \left\{ < \frac{\partial u_i}{\partial x_j} + \frac{\partial u_j}{\partial x_i} >< \frac{\partial u_i}{\partial x_j} + \frac{\partial u_j}{\partial x_i} > \right\}, \tag{A.1}$$

where ν is the kinematic viscosity and s_{ij} the strain rate. Note that the repeated indices (i and j) are summed over 1, 2 and 3. One should note that we can not measure the turbulent energy dissipation rate in the atmosphere using Equation (A.1). Therefore, we use spectral analysis to estimate ε in the atmosphere.

It is assumed that the turbulent energy per unit wave number at scale k, $E(k)$ is independent of direction, and dependent only on the scale k and the rate of transfer ε(or the rate at which energy is dissipated to heat at the very smallest scales) within the inertial subrange of the energy spectrum. Therefore, the following relationship between $E(k)$, k and ε can be written (Hocking, 2006):

$$E(k) \propto \varepsilon^a k^b. \tag{A.2}$$

Dimensional analysis can be used to estimate values of a and b. $E(k)$, ε and k have units of kinetic energy per unit mass per wave number (L^3T^{-2}), kinetic energy per unit mass per unit time (L^2T^{-3}) and L^{-1} respectively. Hence, Equation (A.2) can be rewritten as (Hocking, 2006):

$$L^3T^{-2} \equiv L^{2a-b}T^{-3a}. \tag{A.3}$$

This gives a=2/3 and b= -5/3. Therefore, the energy dissipation rate (ε) can be estimated through the following equation (Hocking, 2006):

$$E(k) = C_E \varepsilon^{2/3} k^{-5/3}, \tag{A.4}$$

where C_E is a constant.

The energy dissipation rate can be also estimated using structure functions. According to Kolmogorov theory, the structure function of turbulent regime, D is dependent only on separation r and ε. D, ε and r have units of kinetic energy per unit mass (L^2T^{-2}), kinetic energy per unit mass per unit time (L^2T^{-3}) and L respectively. Hence, the structure function is given by (Hocking, 2006):

$$D(r) = C_D \varepsilon^s r^t, \tag{A.5}$$

where, C_D is a constant. Dimensional analysis showed that s=2/3 and t=2/3.

Appendix B

Spectra Forms for Velocity Measurements

There are different forms of spectra that can be used for turbulence studies. A more complex form of the spectrum is given by (Batchelor, 1953):

$$\Phi_{ij} = \frac{E(k)}{4\pi k^4}\left(k^2\delta_{ij} - k_i k_j\right), \tag{B.1}$$

which describes the three-dimensional cross-spectrum between the velocity components in the "i" direction and the "j" direction, where "i or $j = 1$" mean the x direction, "i or $j = 2$" mean the y direction and "i or $j = 3$" mean the z direction. In Equation (B.1), δ is the Kronecker delta, k the wave number ($k^2 = k_1^2 + k_2^2 + k_3^2$) and $E(k)$, the total energy. $E(k)$ is given by (Hocking, 1999):

$$E(K) = 1.53\varepsilon^{2/3}k^{-5/3}, \tag{B.2}$$

where ε is the turbulent energy dissipation rate.

For cases of isotropic turbulence, Φ_{ij} can be integrated over a shell of radius k to give (Hocking, 1999):

$$\Psi_{ij}(k) = 4\pi k^2 \Phi_{ij}(k). \tag{B.3}$$

$E(k)$ is related to Ψ_{ij} through the following equation (Hocking, 1999):

$$E(k) = \frac{1}{2}\left(\Psi_{11}(k) + \Psi_{22}(k) + \Psi_{33}(k)\right). \tag{B.4}$$

The individual $\Psi_{ij}(k)$ are difficult to measure experimentally, since a full three-dimensional description of the turbulent field in all three velocity components is needed. If a probe moves in a straight line through a patch of turbulence, recording the velocity components parallel to the direction of motion and then the results are Fourier transformed, the one-dimensional form of the spectrum is obtained through

(Hocking, 1999):

$$\phi_p(k_1) = \alpha_{11}\varepsilon^{2/3}|k_1|^{-5/3}. \tag{B.5}$$

One should note that $\phi_p(k)$ is not the same as Φ_{11}. While $\phi_p(k)$ is the spectral density at k_1 due to contributions of "waves" of all orientations which cross the x axis, $\Phi_{11}(k)$ is the spectral density due to "waves" with phase-fronts aligned perpendicular to the x axis. The spectrum for the velocity perpendicular to the direction of motion is similar to Equation (B.5), however, the constant α_{11} will have a different value.

Appendix C

This Appendix contains a Fortran code that calculates the beam-broadened width.

```
subroutine bbexpres(alpha,nu,delr,R0,u0,shr,sigm2n)
c Fortran subroutine to take beam tilt, 1-way beam half-power half-width,
c pulse length, range, wind parallel to the beam, and wind shear, and
c produce the squared beam-broadened and shear-altered spectral width
c sigma^2 for the component parallel to the beam
real nu
c some constants
a0 = 0.945
b0=1.500
c0=0.030
d0=0.825
a=3.0
b=500.0
c=250.0
d=1.5
e=0.013
f=800.
g=200.
ca = cos(alpha)
sa = sin(alpha)
t1an=nu*nu/(4.0*alog(2.0))*u0*u0*ca
t2an=-1.0*a0*nu/(4.0*alog(2.0))*sa*
$ (sa*2.0*nu*R0)*shr*u0
t3an=$b0/(8.0*4.0*alog(2.0))*(2.0*sa*sa)*(2.0*R0*nu*sa*shr)*
$ (2.0*R0*nu*sa*shr)
xttt =shr*delr/sqrt(12.0)
term4a = c0*(sa*sa*ca*ca)*(abs(u0)*abs(xttt))
```

```
term4b = d0*(sa*sa*ca*ca)*(xttt*xttt)
sigm2n = t1an+t2an+t3an+term4a+term4b
c Now apply final correction.
c limit correction term to prevent it blowing up.
ucrit=8.0
uref=u0
if(u0.ge.0.0.and.u0.lt.ucrit)uref=ucrit
if(u0.lt.0.0.and.u0.gt.(-1.0*ucrit))uref=-ucrit
yshr = shr*20.0/uref
ayshr = abs(yshr)
c ignore correction for small wind shears – more accurate to consider only
c the effect of the mean wind..
if(abs(yshr).lt.0.0015)sigm2n=t1an
if(abs(yshr).lt.0.0015)return
c FINAL CORRECTION TERM to produce model Cc.
sigm2n = sigm2n*(1.0+0.025*exp(-((sa-0.19)/0.05)**2))*
$ (1.0+a*sa**d * ( $ 0.75*(exp(-((delr-b)/c)**2)* tanh(ayshr/e) )
$-(0.25*(tanh((delr-f)/g)+1.0)*
$(1.0-tanh((yshr+0.002)/(0.004))))
$ + (11.5*(nu**1.5)*(tanh((delr-280.0)/70.0)-1.0)
$*(tanh((yshr-0.004)/0.004)+1.0))
$ + (2.0*exp(-((delr-600.0)/150.0)**2)*tanh(yshr/0.05))
$ + (0.05*exp(-((delr-500.0)/120.0)**2)
$ *(tanh((-0.004-yshr)/0.001)+1.0)) ) )
return
end
```

Appendix D

Brunt-Vaisala Frequency

Adiabatic oscillation of an air parcel in the atmosphere about its equilibrium level in a stable atmosphere is referred as buoyancy oscillation. The frequency of such oscillations (Brunt-Vaisala frequency) can be derived by considering an air parcel that is displaced vertically small distance δz. By Newton's second law (Holton, 1992):

$$\frac{D^2}{Dt^2}(\delta z) = -g - \frac{1}{\rho}\frac{\partial p_0}{\partial z}, \tag{D.1}$$

where the first term in the right side of the equation is the gravitational acceleration and the second term is the pressure gradient term. If it is assumed that the environment is in hydrostatic balance, $\rho_0 g = -dp_0/dz$, where ρ_0 and p_0 are the density and the pressure of the environment. Therefore, Equation (D.1) can be rewritten as (Holton, 1992):

$$\frac{D^2}{Dt^2}(\delta z) = -g(\rho - \rho_0)/\rho. \tag{D.2}$$

Using the ideal gas law ($p = \rho RT$, in which R is the gas constant), and Equation (1.7), the above equation can be expressed as (Holton, 1992):

$$\frac{D^2}{Dt^2}(\delta z) = g(1 - \frac{\theta_p}{\theta_0}), \tag{D.3}$$

where θ_p is the potential temperature of the air parcel and θ_0 the environmental value of potential temperature. The acceleration ($a(z) = \frac{D^2}{Dt^2}(\delta z)$) is zero at the equilibrium height z_0. Using a Taylor's expansion we can write (Holton, 1992):

$$a(z) = (\partial a/\partial z)_{z=z_0}(z - z_0). \tag{D.4}$$

The potential temperature of the air parcel is constant because the parcel adjusts adiabatically. Therefore, the change in $a(z)$ with height is due to the variation in

$\theta_0$with height. Thus $\partial a/\partial z = -(\theta_p/\theta_0^2)(d\theta_0/dz)$; however, at $z = z_0$, $\theta_p = \theta_0$, so this reduces to $\partial a/\partial z = -(1/\theta_0)(d\theta_0/dz)$. Thus the acceleration is given by (Holton, 1992):

$$d^2z/dt^2 = -g\,[d(\ln\theta_0)/dz]\,(z - z_0). \tag{D.5}$$

This is the equation for the harmonic motion about the equilibrium at z_0 and the frequency of oscillation is called the Brunt-Vaisala frequency and is given by (Holton, 1992):

$$\omega_B^2 = g\,[d(\ln\theta_0)/dz.] \tag{D.6}$$

Bibliography

Ahrens, C.D., 2000. Meteorology today: An introduction to weather, climate, and the environment, Brooks/Cole.

Atlas, D., 1964. Advances in radar meteorology, in: Landsberg, H., van Mieghem, J.(Eds.), Advances in Geophysics, 10, Academic Press, Inc., 317-478.

Atlas, D., Srivastava, R.C., Sloss, P.W., 1969. Wind shear and reflectivity gradient effects on Doppler radar spectra: II, J. Appl. Meteorol., 8, 384-388.

Batchelor, G.K., 1953. The theory of homogeneous turbulence, Cambridge Universoty Press.

Balsley, B.B., Gage, K.S., 1980. The MST radar technique: Potential for middle atmospheic studies, PAGEOPH, 118, 452-493.

Balsley, B.B., Frehlich, R.G., Jensen, M.L., Meillier, Y, 2006. High-resolution in-situ profiling through the stable boundary layer: Examination of the SBL top in terms of minimum shear, maximum stratification, and turbulence decrease, Am. Meteoro. Soc., 63, 1291-1307.

Barat, J., 1982. Some characteristics of clear-air turbulence in the middle stratosphere, Am. Meteoro. Soc., 39, 2553-2564.

Barat, J., Bertin, F., 1984. On the Contamination of stratospheric turbulence measurements by wind shear, Am. Meteoro. Soc., 41, 819-827.

Bevington, P.R., 1969. Data Reduction and Error Analysis for the Physical Sciences, McGraw-Hill.

Caughey, S.J., Crease, B.A., Asimakapoulos, D.N., Cole, R.S., 1978. Quantitative bistatic acoustic sounding of the atmospheric boundary layer, Q. J. R. Meteorol. Soc., 104, 147-161.

Cornman, L.B., Corrine, S.M., Cunning, G., 1995. Real-time estimation of atmospheric turbulence severity from in-situ aircraft measurements. J. Aircraft, 32, 171-177.

Dehghan, A., Hocking, W.K., 2011. Instrumental errors in spectral-width turbulence measurements by radars, J. Atmos. Solar-Terr.Phys., 73, 1052-1068.

Doviak, R.J., Zrnic, D.S., 1984, Doppler radar and weather observations, Academic Press, Inc.

Fairall, C.W., Markson, R., Schacher, G.E., Davidson, K.L., 1980. An aircraft study of turbulence dissipation rate and temperature structure function in the unstable marine atmospheric boundary layer, Boundary-Layer Meteorol., 19, 453-469.

Fairall, C.W., White, A.B., Thomson, D.W., 1991. A stochastic model of gravity-wave-induced clear-air turbulence, J. Atmos. Sci., 48, 1771-1790.

Fukao, S., Yamanaka, M. D., Ao, N., Hocking, W. H., Sato, T., Yamamoto, M., Nakamura, T., Tsuda, T., Kato, S., 1994. Seasonal variability of vertical eddy diffusivity in the middle atmosphere : 1. Three-years observations by the middle and upper atmosphere radar, J. Geophys. Res., 99, 18973-18987.

Frehlich, R., Sharman, R., 2010, Climatology of velocity and temperature turbulence statistics determined from radiosondes and ACARS/AMDAR data, Am. Meteoro. Soc., 49, 1149-1169.

Gage, K.S., Green, J.L., VanZandt, T.E., 1980. Use of Doppler radar for the measurement of atmospheric turbulence parameters from the intensity of clear-air echoes, Radio Sci., 15, 407-416.

Gage, K.S., 1990. Radar observation of the free atmosphere: structure and dynamics, Atlas, D.(Ed.), Radar in meteorology, 534-565.

Gavrilov, N.M., Luce, H., Crochet, M., Dalaudier, F., Fukao, S., 2005. Turbulence parameter estimations from high-resolution balloon temperature measurements of the MUTSI-2000 campaign, Ann. Geophysics, 23, 2401-2413.

Gossard, E.E., 1990. Radar research on the atmospheric boundary layer, Atlas, D.(Ed.), Radar in meteorology, 477-527.

Guo, L., Lehmacher, G. A., Kudeki, E., Akgiray, A., Sheth, R., Chau, J. L., 2007. Turbulence energy dissipation rates and eddy diffusivities in the tropical mesosphere using Jicamarca radar data, Adv. Space Res., 40, 744-750.

He, H., Tarasick, D.W., Hocking, W.K., Carey-Smith, T.K., Rochon, Y., Zhang, J., Makar, P.A., Osman, M., Brook, J., Moran, M.D., Jones, D.B.A., Mihele, C., Wei, J.C., Osterman, G., Argall, P.S., McConnell, J., Bourqui, M.S., 2011. Transport analysis of ozone enhancement in Southern Ontario during BAQS-Met, Atmos. Chem. Phys., 11, 2569–2583.

Hines, C.O., 1991. The saturation of gravity waves in the middle atmosphere. Part III: Formation of the turbopause and of turbulent layers beneath it, J. Atmos. Sci., 48, 1380-1385.

Hocking, W.K., 1983. On the extraction of atmosphere turbulence parameters

from radar backscatter Doppler spectra-I. Theory, J. Atmos. Terr.Phys., 45, 89-102.

Hocking, W.K., 1985. Measurement of turbulent energy dissipation rates in the middle atmosphere by radar techniques, Radio Sci., 20, 1403-1422.

Hocking, W.K., 1986. Observation and measurements of turbulence in the middle atmosphere with a VHF radar, J. Atmos. Terr.Phys., 48, 655-670.

Hocking, W.K., Ruster, R., Czechowsky, P., 1986. Absolute reflectivities and aspect sensitivities of VHF radio wave scatteres measured with the SOUSY radar, J. Atmos. Terr.Phys., 48, 131-144.

Hocking W.K., 1987. Radar studies of small scale structure in the upper middle atmosphere and lower ionosphere, Advances in Space Res., 7, 10, 327-338.

Hocking, W.K., 1988. Two years of continuous measurements of turbulence parameters in the upper mesosphere and lower thermosphere made with a 2-MHz radar, J. Geophys. Res., 93, 2475-2491, 1988.

Hocking, W.K., Target parameter estimation, 1989: Fukao, S. (Ed.), Middle Atmosphere Program, Hand book for map, 30, 228-268.

Hocking, W.K., 1991, The effects of middle atmosphere turbulence on coupling between atmospheric regions, J. Geomag. Geoelectr., 43, 621-636.

Hocking, W.K., 1997. System design, signal processing procedures and preliminary results for the Canadian (London, Ontario) VHF Atmospheric Radar, Radio Sci., 32, 687-706.

Hocking, W.K., Hazma, A.M., 1997. A quantitative measure of the degree of anisotropy of turbulence in terms of atmospheric parameters, with particular relevance to radar studies, J.Atmos.Terr. Phys., 59, 1011-1020.

Hocking, W.K., Mu, K.L., 1997. Upper and middle tropospheric kinetic energy dissipation rates from measurements of Cn2 - review of theories, in-situ investigations, and experimental studies using the Buckland Park atmospheric radar in Australia, J.Atmos.Terr. Phys., 59, 1779-1803.

Hocking, W.K., 1999. The dynamical parameters of turbulence theory as they apply to middle atmosphere studies, Earth planet space, 51, 525-541.

Hocking, W.K., Rottger, J., 2001. The structure of turbulence in the middle and lower atmosphere seen by and deduced from MF, HF and VHF radar, with special emphasis on small-scale features and anisotropy, Ann. Geophysics, 19, 933-944.

Hocking, W.K., 2003. Fast and accurate calculation of spectral beam-broadening for turbulence studies, Proceeding of the Tenth International Workshop on Technical and Scientific Aspect of MST Radar, Piura, Peru, May 13-20, 2003, 214-217.

Hocking, W.K., 2006. Course wave and turbulence, Lecture notes, pp115-118.

Hocking, W.K., Taylor, P.A., Zawadzki, I., Argall, S., Fabry, F., McBean, G., Sica, R., Hangan, H., Klaassen, G., Barron, J., Mercer, R., 2007. "A New 40-55 MHz Windprofiler Network in Ontario and Quebec, Canada – The O-Qnet", Proceeding of the Eleventh International Workshop on Technical and Scientific Aspects of MST Radar, Gadanki, India, Dec 11-15, 2006, 377-380.

Hocking, A., and W.K. Hocking, 2007. Turbulence anisotropy determined by Windprofiler Radar and its correlation with rain events in Montreal, Canada, J. Atmos. Oceanic Technology, 24, 40-51.

Holmes, P., Lumley, J.L., Berkooz, G., 1996. Turbulence, Coherent Structures, Dynamical Systems and Symmetry, Cambridge University Press.

Holton, J.R., 1992. An introduction to dynamic meteorology, Academic Press Inc.

Hooper, D., Thomas, L., 1995. Aspect sensitivity of VHF scatterers in the troposphere and stratosphere from comparison of powers in off-vertical beams, J. Atmos.Terr.Phys., 57,655-663.

Jacoby-Koaly, S., Campistron, B., Bernard, S., Bénech, B., Ardhuin-Girard, F., Dessens, J., Dupont E., Carissimo, B., 2002. Turbulent dissipation rate in the boundary layer via UHF wind profiler Doppler spectral width measurement. Bound.-Layer Meteor. 103,361–389.

Kaniewski, P., 2006. Aircraft positioning with INS/GNSS integrated system, Molecular and Quantum Acoustics, 27, 149-168.

Kantha, L., Hocking, W.K., 2010. Dissipation rates of turbulence kinetic energy in the free atmosphere: MST radar and radiosondes, J. Atmos. Solar-Terr.Phys., 73, 1043-1051.

Keeler. R.J., Passarelli. R.E, 1990. Signal processing for atmospheric radars, Atlas, D.(Ed.), Radar in meteorology, 199-229.

Kolmogorov, A.N., 1941. Dissipation of Energy in the Locally Isotropic Turbulence, Proceedings of the USSR Academy of Sciences 32: 16–18; translated in English "The local structure of turbulence in incompressible viscous fluid for very large Reynolds numbers", Proceedings of the Royal Society of London, Mathematical and Physical Sciences, 434 (1980), 15–17.

Lambert, W.C., Taylor, G.E., 1998. Data quality assessment methods for the eastern range 915 MHz wind profiler network, NASA contractor report# NASA/CR-1998-207906.

Lee, Y., Paradis, A.R., Klingle-Wilson, D., 1988. Preliminary results of the 1983 coordinated aircraft-Doppler weather radar turbulence experiment, Report # DOT/FAA/PM-86/11 (A197894)

Lindborg, E., 1999. Can the atmospheric kinetic energy spectrum be explained by two-dimensional turbulence? J. Fluid Mech., 388, 259-288.

Lovejoy, S., Schertzer, D., Tuck, A.F., 2004. Fractal aircraft trajectories and nonclassical turbulent exponents, PhysRevE.70.036306.

Luce, H., Fukao, S., Dalaudier, F., Crochet, M., 2002. Strong mixing events observed near the tropopause with the MU radar and high-resolution balloon techniques, Am. Meteoro. Soc., 59, 2885-2896.

Mahrt, L., 1989. Intermittent of atmospheric turbulence, J. Atmos. Sci., 46, 79-95.

May, P.T., Fukao, S., Tsuda, T., Sato, T., Kato, S., 1988. The effect of thin scattering layers on the determination of wind by Doppler radars, Radio Sci., 23, 83-94.

Meillier, Y.P., Frehlich, R,G., Jones, R.M., Balsley, B.B., 2008, Modulation of small-scale turbulence by ducted gravity waves in the nocturnal boundary layer, Am. Meteoro. Soc., 65, 1414-1427.

Meischner, P., Baumann, R., Holler, H., Jank, T., 2001. Eddy dissipation rates in thunderstorms estimated by Doppler radar in relation to aircraft in-situ measurements, Am. Meteoro. Soc., 18, 1609-1627.

Nappo, C.J., 2002. An introduction to atmospheric gravity waves, Academic Press.

Narayana Rao, D., Narayana Rao, T., Venkataratnam, M., Thulasiraman, S., Rao, S.V., Srinivasulu, P., Rao, P.B., 2001, Diurnal and seasonal variability of turbulence parameters observed with Indian mesosphere-stratosphere-troposphere radar, Radio Science, 36, 1439-1457.

Nastrom, G.D., 1997. Doppler radar spectral width broadening due to beamwidth and wind shear, Ann. Geophysics, 15, 786-796.

Nastrom, G.D., Eaton, F.D., 1997. Turbulence eddy dissipation rates from radar observations at 5-20 km at White Sands Missile Range, New Mexico, J. Geophys.Res., 102, 19495-19505.

Nastrom, G.D., Tsuda, T., 2001. Anisotropy of Doppler spectral parameters in the VHF radar observations at MU and White Sands, Ann. Geophysics, 19, 883-888.

Nastrom, G.D., Eaton, F.D., 2002. A case study of atmospheric conditions at 4-19 km over Vandenberg Air Force Base during passage of a cyclone, Am. Meteoro. Soc., 42, 467-475.

Panofsky, H.A., Dutton, J.A., 1984. Atmospheric turbulence, John Wiley & Sons.

Quintarelli, F., 1993. Acoustic sounder observations of atmospheric turbulence

parameters in a convective boundary layer, Am. Meteoro. Soc., 32, 1433-1440.

Rees, D., Roper, R.G., Lloyd, Low, C.H., 1972. Determination of the structure of the atmosphere between 90 and 250 km by means of contaminants releases at Woomera, May 1968, Philosophical Transactions of the Royal Society of London, 271, 631-663.

Rottger. J., 1989. The instrumental principles of MST radars and incoherent scatter radars and the configuration of radar system hardware, Fukao, S. (Ed.), Middle Atmosphere Program, Hand book for map, 30, 54-113.

Sato, T., 1989. Radar Principles, Target parameter estimation, Fukao, S. (Ed.), Middle Atmosphere Program, Hand book for map, 30, 19-53.

Shaw, W.J., LeMone, M.A., 2003, Turbulence dissipation rate measured by 915 MHz wind profiling radars compared with in-situ tower and aircraft data, Twelfth Symposium on Meteorological Observations and Instrumentation, Am. Meteoro. Soc., California.

Simon, D., 2001. Kalman filtering, Embedded Systems Programming, 14, 20-32.

Sloss, P.W., Atlas, D., 1968. Wind shear and reflectivity gradient effect on Doppler radar spectra, J. Atmos. Sci., 25, 1080-1089.

Stull, R.B., 1988. An introduction to boundary layer meteorology, Kluwer Academic Publishers.

Sutton, P.G., 1960 :Atmospheric turbulence, Worsnop, B.L. (Ed). Methuen & Co. Ltd., John Wiley & Sons, Inc.

Taylor, G.I., 1922. Diffusion by continuous movements, Proceeding of the London Mathematical Society, 20, 196-212.

Taylor, R.J., 1972. Aircraft measurements of dissipation of turbulent kinetic energy, Quart. J. R. Met. Soc., 98, 658-661.

VanZandt, T.E., Green, J.L., Gage, K.S., Clark, W.L., 1978. Vertical profiles of refractivity turbulence structure constant: Comparison of observations by the Sunset radar with a new theoretical model, 13, 819-829.

Vinnichenko, N.K., Pinus, N.Z., Shmeter, S.M., Shur, G.N., 1973. Turbulence in the free atmosphere, Dutton, J.A. (Ed). Consultants Bureau.

Weber, B. L., Wuertz, D.B., 1991. Quality control algorithm for profiler measurements of winds and temperatures. NOAA Tech. Memo., ERL WPL-212, 32pp.

Wroblewski, D.E., Cote, O.R., Hacker, J.M., Dobosy, R.J., 2010, Velocity and temperature structure functions in the upper troposphere and lower stratosphere from high-resolution aircraft measurements, Am. Meteoro. Soc., 67, 1157-1170.

Wyngaard, J.C., 2010. Turbulence in the atmosphere, Cambridge University

Press.

Yague, C., Viana, S., Maqueda, G., Redondo, J. M., 2006. Influence of stability on the flux-profile relationships for wind speed, ϕ_m, and temperature, ϕ_h, for the stable atmospheric boundary layer, Nonlin. Processes Geophys., 13, 185-203.

Copyright and Reprint Permissions

Dear Armin Dehghan

We hereby grant you permission to reprint the material detailed below at no charge in your thesis subject to the following conditions:

1. If any part of the material to be used (for example, figures) has appeared in our publication with credit or acknowledgement to another source, permission must also be sought from that source. If such permission is not obtained then that material may not be included in your publication/copies.

2. Suitable acknowledgment to the source must be made, either as a footnote or in a reference list at the end of your publication, as follows:

"This article was published in Publication title, Vol number, Author(s), Title of article, Page Nos, Copyright Elsevier (or appropriate Society name) (Year)."

3. Your thesis may be submitted to your institution in either print or electronic form.

4. Reproduction of this material is confined to the purpose for which permission is hereby given.

5. This permission is granted for non-exclusive world English rights only. For other languages please reapply separately for each one required. Permission excludes use in an electronic form other than submission. Should you have a specific electronic project in mind please reapply for permission

6. This includes permission for the Library and Archives of Canada to supply single copies, on demand, of the complete thesis. Should your thesis be published commercially, please reapply for permission.

Yours sincerely

Jennifer Jones Rights Associate

Elsevier Limited, a company registered in England and Wales with company number 1982084, whose registered office is The Boulevard, Langford Lane, Kidlington, Oxford, OX5 1GB, United Kingdom.

——Original Message—— From: adehghan@uwo.ca [mailto:adehghan@uwo.ca] Sent:

29 August 2011 20:18 To: Rights and Permissions (ELS) Subject: Obtain Permission
This Email was sent from the Elsevier Corporate Web Site
and is related to Obtain Permission form:

———————————————————————-

Product: Customer Support
Component: Obtain Permission
Web server: http://www.elsevier.com
Armin Dehghan
The University of Western Ontario
1151 Richmond street
N6A3K7, London, Canada
To use the following material:
ISSN/ISBN: 978-0-12-221420-2
Title: Doppler radar and weather observations
Author(s): Doviak and Zrnic
Volume: N/A
Issue: N/A
Year: 1984
Pages: 10
Article title: N/A
How much of the requested material is to be used:
I would like to use figure 2.3 (only one figure) of this book in my thesis.
Are you the author: No
Author at institute: No
How/where will the requested material be used: In a thesis or dissertation
Details:
I would like to use figure 2.3 (only one figure) of this book in my thesis.
Dear Armin,

Thank you for your interest in reproducing AGU published material. AGU does not require that permission be obtained from AGU or the author(s) for the use of tables, figures, or short extracts of papers published in AGU journals or books, provided that the original publication be appropriately cited.

The standard credit line for the citation is, "Author(s), title, publication, volume number, issue number, citation number (or page number(s) prior to 2002), date. Copyright [year] American Geophysical Union." The following must also be included, "Reproduced/modified by permission of American Geophysical Union."

If an article was placed in the public domain, in which case the words “Not subject to U.S. copyright” appear on the bottom of the first page or screen of the article, please substitute “published” for the word “copyright” in the credit line mentioned above.

Copyright information is provided on the inside cover of our journals. For permission for any other use, please contact the AGU Publications Office at AGU, 2000 Florida Ave., N.W., Washington, DC 20009. Should you need further assistance, please feel free to contact me at your convenience.

Regards,

Antonio Covington

AGU Member Service Representative

This is a License Agreement between Armin Dehghan ("You") and Elsevier ("Elsevier") provided by Copyright Clearance Center ("CCC"). The license consists of your order details, the terms and conditions provided by Elsevier, and the payment terms and conditions. All payments must be made in full to CCC. For payment instructions, please see information listed at the bottom of this form.

Supplier Elsevier Limited

The Boulevard,Langford Lane Kidlington,

Oxford,OX5 1GB,UK

Registered Company Number 1982084

Customer name Armin Dehghan Customer

address

The Department of Physics and Astronomy

London, ON N6A 3K7

License number 2738391095424

License date Aug 29, 2011

Licensed content publisher Elsevier Licensed content publication Journal of Atmospheric and Terrestrial Physics Licensed

content title On the extraction of atmospheric turbulence parameters from radar backscatter Doppler spectra—I. Theory Licensed content

author W.K. Hocking Licensed

content date February-March 1983

Licensed content volume number 45

Licensed content issue number 2–3

Number of pages 14 Start Page 89 End Page 102

Type of Use reuse in a thesis/dissertation Intended publisher of new work other Portion figures/tables/illustrations Number of figures/tables/illustrations 1

Format both print and electronic

Are you the author of this Elsevier article? No

Will you be translating? No

Order reference number

Title of your thesis/dissertation Validation and Application of Wind Profiler Measurements of Atmospheric Turbulence Expected completion date Aug 2011

Estimated size (number of pages) 120 Elsevier

VAT number GB 494 6272 12

Permissions price 0.00 USD VAT/Local Sales Tax 0.0 USD / 0.0 GBP Total 0.00 USD Terms and Conditions.

This is a License Agreement between Armin Dehghan ("You") and Elsevier ("Elsevier"). The license consists of your order details, the terms and conditions provided by Elsevier, and the payment terms and conditions.

License Number 2736540697433

License date Aug 26, 2011

Licensed content publisher Elsevier Licensed content publication Journal of Atmospheric and Solar-Terrestrial Physics

Licensed content title Instrumental errors in spectral-width turbulence measurements by radars

Licensed content author Armin Dehghan,Wayne K. Hocking

Licensed content date June 2011 Licensed content volume number 73 Licensed content issue number 9 Number of pages 17

Type of Use reuse in a thesis/dissertation Portion full article Format both print and electronic

Are you the author of this Elsevier article? Yes

Will you be translating? No

Order reference number

Title of your thesis/dissertation Validation and Application of Wind Profiler Measurements of Atmospheric Turbulence

Expected completion date Aug 2011 Estimated

size (number of pages) 120 Elsevier

VAT number GB 494 6272 12 Permissions price 0.00 USD VAT/Local Sales Tax 0.0 USD / 0.0 GBP Total 0.00 USD

Vita

NAME:	Armin Dehghan
POST-SECONDARY EDUCATION AND DEGREES:	The University of Western Ontario London, Ontario, Canada 2005-2007, M.Sc.
	Tehran University Tehran, Iran 1998-2000, M.Sc.
	Isfahan University Isfahan, Iran 1993-1998, B.Sc.
RELATED WORK EXPERIENCE:	Graduate Teaching Assistant The University of Western Ontario 2005-2011
	Graduate Research Assistant The University of Western Ontario 2005-2011

PUBLICATIONS:

Dehghan. A., and Hocking, W.K., 2011, Instrumental errors in spectral-width turbulence measurements by radars, J. Atmos.Solar-Terr.Phys., 73, 1052-1068.